



UNIVERSITÀ  
DEGLI STUDI  
DI TRIESTE

**UNIVERSITÀ DEGLI STUDI DI TRIESTE**  
**XXXIII CICLO DEL DOTTORATO DI RICERCA IN**  
**NANOTECNOLOGIE**

**Progetto co-finanziato dall'Istituto di Ricovero e Cura a Carattere Scientifico - IRCCS Burlo Garofolo**

**ATOMIC FORCE MICROSCOPY-BASED ESSAY FOR  
BIOMEDICAL APPLICATIONS**

Settore scientifico-disciplinare: **FIS/03**

DOTTORANDO / A  
**ALICE BATTISTELLA**

COORDINATORE  
**ALBERTO MORGANTE**

SUPERVISORE DI TESI  
**MARCO LAZZARINO**

CORRELATORE  
**LAURA ANDOLFI**

**ANNO ACCADEMICO 2019/2020**



## **Ringraziamenti**

Per cominciare, il ringraziamento più grande va a Marco. Per tutti i consigli, le conoscenze, le idee fornitemi durante questi anni. Per essere stato in grado di stimolare la mia curiosità scientifica, aver sempre tenuto in considerazione le mie opinioni e avere accolto positivamente il mio lavoro.

Un altro ringraziamento speciale va a Laura, per l'entusiasmo e la passione che mette in questo lavoro e la capacità di trasmetterla. Per aver condiviso i miei piccoli traguardi con gioia e al tempo stesso avermi motivato di fronte agli ostacoli incontrati.

Vorrei ringraziare i miei amici. In particolare, le amicizie più antiche e consolidate con le quali ho condiviso davvero tanto, momenti belli e momenti bui, che ci hanno unito moltissimo. Gianluca, Lucia, Marzia, Giovanni, Martina e Micol. Sono infinitamente grata di avervi incontrato.

A Valentina e Leonardo, due speciali persone a cui in questi ultimi anni mi sono molto affezionata. Un grazie speciale a Stefano, Giovanni, Francesco, Chiara, Micol, Carlo e Luca. Perché casa per me è anche un po' famiglia e in questi anni la vostra presenza mi è stata di grande conforto.

A Chiara, mia cugina, che per certi versi sarà sempre un po' una sorella per me.

A Tommaso, perché è entrato nella mia vita in punta di piedi e con grande forza e dolcezza ha saputo accettare le mie debolezze, accompagnandomi in questo percorso, da cui esco più forte e consapevole.

Grazie alla mamma, perché è per me l'esempio più grande della forza dell'amore. Grazie a papà, perché a tratti nelle sue fragilità ho riscoperto la forza del legame che ci unisce.



## **Acknowledgement**

I would like to thank financial support from Regione Friuli Venezia Giulia, within the framework of “Regional Law 17/2004: Contributions for clinical, translational, basic, epidemiological and organizational research” with the project “BioMec—Application of Biomechanical Technologies to Integrate Traditional Methodologies in the Hospital Context”.

Thanks for financial support the Doctoral School in Nanotechnology, University of Trieste (Italy) and “Istituto di Ricovero e Cura a Carattere Scientifico - IRCCS Burlo Garofolo” that funded my PhD.

In particular, thanks to Giuseppe Ricci and the team of embryologist, Stefania, Elena and Monica for their precious suggestions and their availability to answer my questions.

Thanks to Marco Stebel and Paola Zarattini and all the people of the animal unit, because their work has been essential for my research.

Thanks to all the colleagues and the collaborators, from which I learned a lot and with whom I had the opportunity to be involved in very nice projects.



## **Abstract**

The investigation of cellular mechanical properties for the evaluation of the cell physiological state has emerged as a hot topic in the last decade. In this framework, different aspects of the mechanobiology are considered in three biomedical fields. First, the alteration of the mechanical phenotype, the cell structure and morphology of melanoma cells according to the levels of production of a factor involved in the cytoskeleton organization, are considered. Secondly, mechanotransduction, and more precisely the capability of cells to adapt their mechanics to the environmental condition was investigated on the effect of a heart failure on cardiac pericytes. In the last part, the mechanical properties of oocytes have been identified as a scoring system to evaluate the quality of oocytes to be selected for the practice of the *in vitro* fertilization. In particular, I investigated the evolution of the oocyte stiffness and viscosity during post-ovulatory ageing, one of the processes responsible for the decreased yields of in vitro fertilization. Here, two mechanical parameters were found, able to predict ageing status of the oocytes before any visual feature due to degradation, allowing to introduce a novel classification for pre-apoptotic and non-fertile oocytes.



# Table of Contents

<b>Introduction .....</b>	<b>15</b>
<b>Chapter 1</b>	
<b>    1.1 The role of forces in biology.....</b>	<b>19</b>
<b>        1.1.1 Embryonic and mesenchymal stem cells .....</b>	<b>20</b>
<b>        1.1.2 Somatic cells and tissues homeostasis .....</b>	<b>21</b>
<b>        1.1.3 Cancer progression.....</b>	<b>22</b>
<b>    1.2 Mechanotransduction .....</b>	<b>24</b>
<b>        1.2.1 Focal adhesions complexes.....</b>	<b>24</b>
<b>        1.2.2 Cytoskeleton .....</b>	<b>26</b>
<b>        1.2.3 The message delivery to the nucleus .....</b>	<b>27</b>
<b>        1.2.4 Transcriptional activation.....</b>	<b>288</b>
<b>    1.3 Methods of the mechanobiology.....</b>	<b>29</b>
<b>    1.4 Active stimulation methods .....</b>	<b>31</b>
<b>        1.4.1 Micropipette aspiration.....</b>	<b>31</b>
<b>        1.4.2 Optical tweezers (OTs) .....</b>	<b>32</b>
<b>        1.4.3 Optical stretching.....</b>	<b>33</b>
<b>        1.4.5 Magnetic twisting cytometry (MTC) .....</b>	<b>34</b>

<b>1.4.6 Parallel-plate rheometry .....</b>	<b>34</b>
<b>1.4.7 Cell monolayer rheology (CMR) .....</b>	<b>34</b>
<b>1.5 Passive methods .....</b>	<b>36</b>
<b>1.5.1 Traction force microscopy (TFM).....</b>	<b>36</b>
<b>1.5.2 Micro-engineered platforms .....</b>	<b>36</b>

## Chapter 2

<b>2.1 Basic principles of AFM.....</b>	<b>39</b>
<b>2.2 Imaging.....</b>	<b>40</b>
<b>2.2.1 Contact mode imaging.....</b>	<b>41</b>
<b>2.2.2 Dynamic modes .....</b>	<b>42</b>
<b>2.3 Force spectroscopy .....</b>	<b>44</b>
<b>2.3.1 Single cell force spectroscopy and applications .....</b>	<b>44</b>
<b>2.3.2 Calibration of probe .....</b>	<b>45</b>
<b>2.3.3 Creep and stress-relaxation .....</b>	<b>46</b>
<b>2.3.4 Indentation .....</b>	<b>47</b>
<b>2.3.5 Single Cell adhesion.....</b>	<b>49</b>
<b>2.4 Indenters and experimental conditions .....</b>	<b>50</b>
<b>2.5 Mechanical models for living cells .....</b>	<b>51</b>
<b>2.5.1 Linear elastic solid models .....</b>	<b>52</b>

<b>2.5.2 Maxwell model .....</b>	<b>55</b>
<b>2.5.3 Linear viscoelastic solid model .....</b>	<b>56</b>
<b>2.5.4 Generalized Maxwell model.....</b>	<b>57</b>

## **Chapter 3**

<b>3.1 Introduction .....</b>	<b>59</b>
<b>3.2 Stemness state evaluation .....</b>	<b>61</b>
<b>3.2.1 Cell transformation potential .....</b>	<b>61</b>
<b>3.2.2 Tumorigenic potential .....</b>	<b>63</b>
<b>3.2.3 Stemness related markers expression .....</b>	<b>64</b>
<b>3.3 Cytoskeleton organization and biomechanical implications .....</b>	<b>65</b>
<b>3.3.1 Actin cytoskeleton and intermediate filaments organization .....</b>	<b>65</b>
<b>3.3.2 Cell mechanical properties.....</b>	<b>70</b>
<b>3.3.3 Cell height and morphology.....</b>	<b>71</b>
<b>3.4 Conclusions .....</b>	<b>73</b>

## **Chapter 4**

<b>4.1 Introduction .....</b>	<b>77</b>
<b>4.2 Cardiac pericytes, cell lines characterization .....</b>	<b>79</b>
<b>4.2.1 Cardiac pericytes rarefaction in chronic ischemia .....</b>	<b>79</b>

<b>4.2.2 Pericytes activity of angiogenesis induction is impaired in failing hearts .....</b>	<b>80</b>
<b>4.3 Pericytes different responses to external stimuli .....</b>	<b>81</b>
<b>    4.3.1 Hydrogel preparation with different stiffnesses .....</b>	<b>81</b>
<b>    4.3.2 Hydrogel coating with fibronectin .....</b>	<b>82</b>
<b>    4.3.3 Cell morphological change in response to external stimuli .....</b>	<b>82</b>
<b>    4.3.5 Mechanosensing alteration of pericytes isolated from failing hearts.....</b>	<b>85</b>
<b>    4.3.6 Mechanotransduction properties are altered in pathology-related pericytes.....</b>	<b>88</b>
<b>4.4 Possible regulation of YAP nuclear translocation by different drugs.....</b>	<b>89</b>
<b>4.5 Conclusions .....</b>	<b>91</b>

## Chapter 5

<b>5.1 Introduction .....</b>	<b>95</b>
<b>5.2 Methods .....</b>	<b>100</b>
<b>    5.2.1 Mouse oocytes retrieval and cumulus cells removal.....</b>	<b>100</b>
<b>    5.2.2 Oocyte freezing and thawing procedure.....</b>	<b>101</b>
<b>    5.2.3 AFM-indentation measurements.....</b>	<b>103</b>
<b>    5.2.4 Macro-probes fabrication .....</b>	<b>106</b>
<b>    5.2.5 AFM stress-relaxation measurements .....</b>	<b>108</b>
<b>    5.2.6 Cortical granule staining.....</b>	<b>109</b>

<b>5.2.7 ZP removal .....</b>	<b>110</b>
<b>5.2.8 Cumulus cells retrieval and culture .....</b>	<b>110</b>
<b>5.2.9 In vitro fertilization .....</b>	<b>111</b>
<b>5.3 Results.....</b>	<b>113</b>
<b>5.3.1 AFM investigation of the mechanical properties of mouse oocytes .....</b>	<b>113</b>
<b>5.3.2 Is post-ovulatory ageing affected by AFM indentation? .....</b>	<b>116</b>
<b>5.3.3 The mechanical properties of the oocyte depend on the postovulatory aging .....</b>	<b>119</b>
<b>5.3.4 The mechanical properties of the oocyte during the postovulatory aging do not depend on the measurement approach. .....</b>	<b>121</b>
<b>5.3.5 The mechanical properties of the oocytes depend on the release of the GC .....</b>	<b>125</b>
<b>5.3.6 ZP Stiffness variation in parthenogenetically activated oocytes .....</b>	<b>126</b>
<b>5.3.7 ZP stiffening in the aged oocytes correlates with a decrease in the IVF yields.....</b>	<b>127</b>
<b>5.4 Conclusions .....</b>	<b>130</b>
<b>General conclusions.....</b>	<b>133</b>
<b>References.....</b>	<b>137</b>



## Introduction

In 1981 the invention of Scanning Tunnelling Microscopy (STM) marked an important step in the field of microscopies. For the first time the goal of imaging individual atoms was reached, going beyond the diffraction limit and achieving higher sensitivity than electron microscopies. By applying a voltage bias between a conductive sample and a probe having a tip just one atom wide, it was possible to measure the tunnelling current between the tip and the sample that was proportional to the tip-to-sample distance. Few years later, in 1986, another technique, the Atomic Force Microscopy (AFM), able to work in liquid in physiological conditions on non-conductive samples and with a similar sensitivity was developed. By using this technique, the imaging of biological samples in physiological conditions, *in vitro*, on living cells, and living organoids was achieved, allowing to obtain the first high resolution images of proteins and biological molecules. In the following years many important achievements were made: with the introduction of the high speed AFM, the dynamics of the molecular processes could be observed. At the same time the development of force spectroscopy allowed to study the forces involved in the interaction between macromolecules. The forces involved in the folding/unfolding of proteins have been detected; the energy landscape of receptor-ligand interactions has been unveiled as well as the working mechanism of many cell membrane molecular complexes, like bacteriorhodopsin, protonic pumps or the photosynthetic machinery. The forces involved in cell-cell interaction and adhesion mechanisms have been precisely measured, as well as the tension developed during cell division.

The role of forces in cellular biology became more and more recognized, especially after the discovery of the mechanotransduction mechanisms that allow the cell to translate the mechanical stimuli perceived from the extracellular environment into the activation or repression of specific

genes. The alteration of these pathways has been associated to pathologies and diseases. An impairment of cellular mechanisms or structural alterations can also lead to a variation of the mechanical properties of the cells, which in turn paves the way to the development of innovative and non-invasive diagnostic tools based on the detection of the cellular mechanical properties.

In Chapter 1 of this thesis, the reader is introduced to the cell mechanobiology, how the cells sense and transduce the mechanical stimuli into the activation of specific molecular pathways that can be altered in the case of specific diseases. Moreover, an overview of the most commonly used methods to evaluate the forces and the cell biophysical properties is provided. In Chapter 2, I focus the attention on the AFM, as a powerful tool to investigate the cell morphology, cell adhesion and the cell mechanical properties, like elasticity, and viscosity. The possibility to probe the mechanics of different cell compartments by changing the experimental conditions like the indenter geometry and the indentation depth, together with the importance of selecting appropriate mechanical model to analyse the experimental data is discussed. In Chapter 3, I will talk about the impairment of the cytoskeleton components of melanoma cell lines according to the level of production of a protein involved in the actin polymerization and how this affects the cell mechanical properties and morphology. Moreover, the connection between this altered phenotype and cell invasiveness and stemness is evaluated. In Chapter 4, the altered mechanotransduction pathways that characterize cardiac pericytes recovered from ischemic hearts compared to the one from healthy patients is discussed. How this translates into a change in the ability to modulate the cell mechanical properties when seeded on hard substrates and the potential therapeutic use of these cells for the treatment of microcirculation diseases is also considered.

Finally, Chapter 5 describes the relation between the mechanical properties and the quality of the oocytes looking at the change of the cell elasticity and viscosity during post-ovulatory ageing, one of the main processes affecting the yields of the in vitro fertilization (IVF). Moreover, by simultaneous epifluorescence measurements, the origin of the observed phenomena is related to a known molecular process occurring in the aged oocyte and leading to the change in the mechanical properties of the

oocyte external glycoproteic layer. The use of a safe and sensitive essay able to predict the potential of an oocyte to be fertilized, is demonstrated with relevant clinical implications related to the exploitation of this procedure for the selection of the oocytes for IVF.



# Chapter 1

## 1.1 The role of forces in biology

From the fertilization to the embryogenesis to the adult tissue homeostasis and the progression of pathologies and diseases, cells are continuously subjected to mechanical stimuli and to nanoscale to macroscale forces of different kind and orientation: blood flow induces shear stress on the vessel wall, weight bearing induces compressive and tensile stresses on bones. Different tissues in the body have different mechanical phenotypes that depend upon the biophysical and biochemical properties of the surrounding extra-cellular environment (Figure 1).

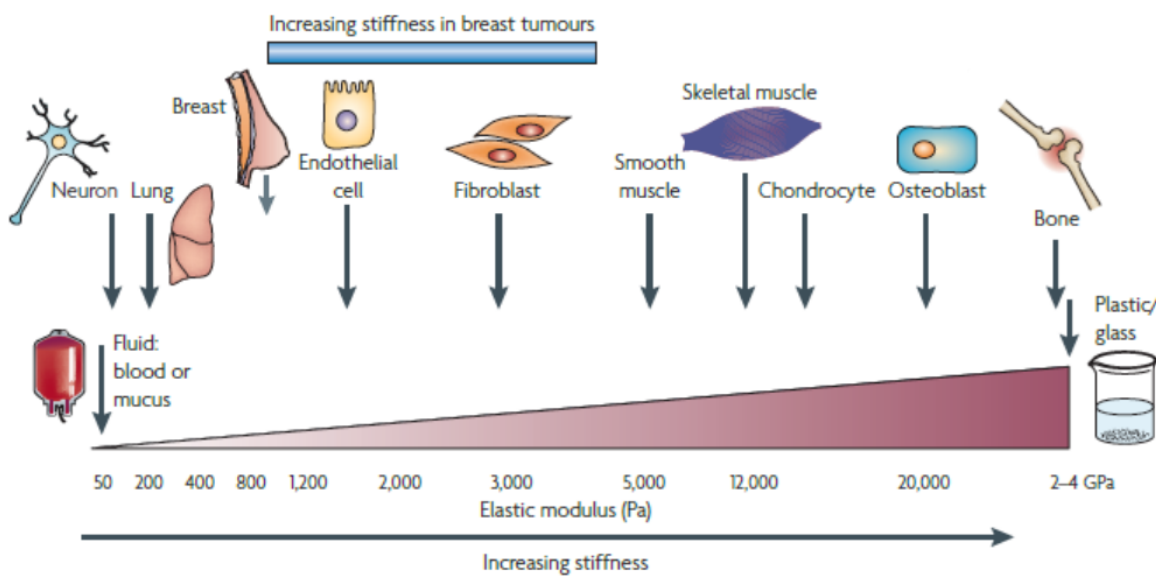


Figure 1: Different elasticity of the tissues in the body, from the soft brain to the stiffskeletal tissue. The mechanical properties are determined by cell-cell interaction and by cell sensing of the surrounding ECM and can change in the case of specific diseases (Butcher, 2009)

Even in the softest and “static” tissues such as brain and breast, cells are exposed to force or tension generated by cell-cell or cell-ECM (extracellular matrix) interactions (Butcher D. A., 2009).

These forces are sensed and integrated by the cell through mechanosensitive molecules and translated into cellular responses by complex biochemical pathways that are responsible for a change in gene expressions by the activation of specific transcription factors. In this way cells can modulate the

intracellular processes as well as influence the biochemical and biophysical properties of the microenvironment with which they constantly interact.

### 1.1.1 Embryonic and mesenchymal stem cells

Embryonic and mesenchymal stem cells (MSCs) differentiate according to tension fields generated by specific matrix elasticity: soft matrix directs stem cells into neurogenic lineages, whereas stiffer matrices direct stem cells into myogenic and osteogenic lineages.

Tissue-specific development and morphogenesis are often orchestrated by specific-forces, as, for instance, the branch patterning in the lung epithelium dictated by remodelling of the ECM.

Mesenchymal stem cells can be induced toward a different specific lineage by the modulation of ECM stiffness: MSCs on softer substrates can generate adipocytes, on the contrary on stiffer matrices osteoblasts can be formed (Engler, 2006). In regenerative medicine the potential of stem cells combined with biomaterials relies on their cross-talk. Stem cells release bioactive molecules and exert forces through the cytoskeletal components to recreate their niche (Vining, 2017). Conversely, as summarized in Figure 2, biomaterials shape, surface and stiffness act on stem cells by modulating their fate (Martino S. D., 2012).

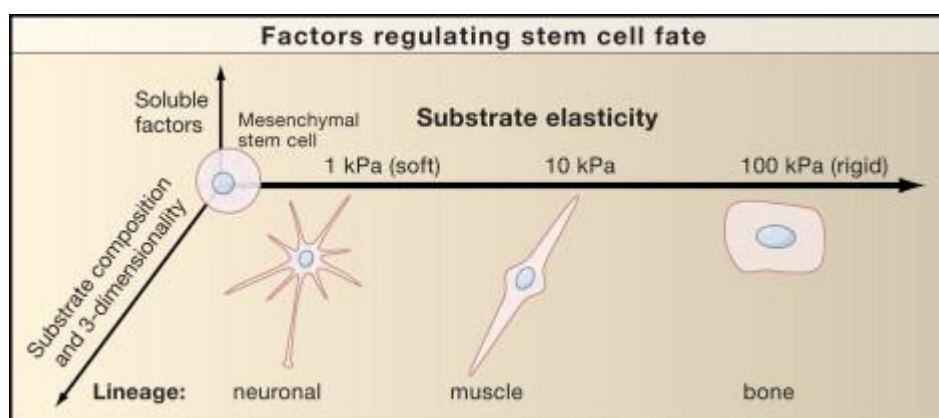


Figure 2: stem cell fate can be modulated by substrate elasticity, nanotopography and the presence of specific biochemical factors (Engler, 2006)

### **1.1.2 Somatic cells and tissues homeostasis**

A balance of forces is also required to maintain somatic cells homeostasis (Figure 3), examples are bone and vascular tissue where the external mechanical loading in the first case and the blood shear flow in the second one allows to prevent the occurrence of specific diseases and regulates the cell growth according to preferential directions, respectively.

Skeletal health depends on mechanical loading and reduced motility leads to a loss of proteoglycan content of articular cartilage that brings to arthritis-associated degeneration (Bird, 2000). The effect of biophysical cues is also important in osteoblast differentiation as well as in the development of bone related pathologies; during osteoporosis the mechanotransduction mechanisms appear to be compromised (Haugh, 2015).

A further example of the effect of forces exerted by ECM on cellular fate is the morphological change of branched capillaries formed by endothelial cells cultured on compliant gels to larger lumens vessels when cultured on stiffer substrates. Collagen crosslinking by glycosylation modifies the ECM tensile-strength and elasticity, likely caused by enzyme mediated action or physiologically increased glycan levels, as occurs in blood vessels of diabetic patients that compromises cardiac function (Susic, 2007). Many cardiovascular diseases are characterized by an impaired mechanical phenotype, in particular arterial stiffening is a key event in the progression of coronary heart disease, hypertension and atherosclerosis (Mitchell, 2010).

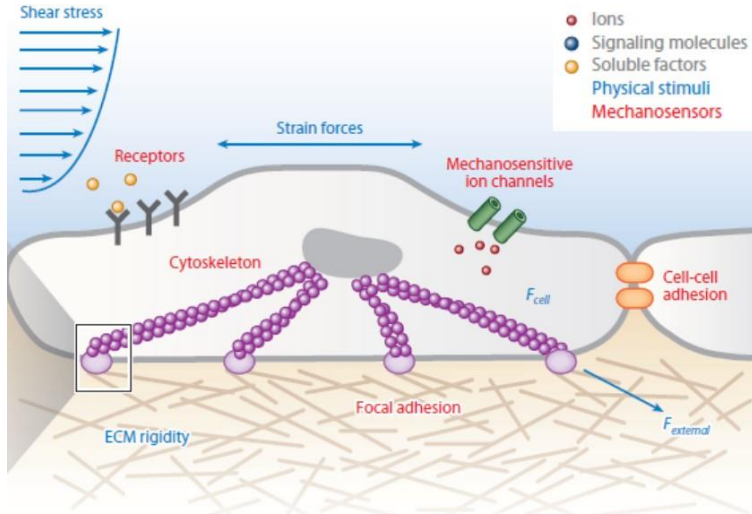


Figure 3: the main biophysical and biochemical signals coming from the external microenvironment involved in the modulation of the cell mechanical phenotype (Sun Y. C., 2012)

Other examples are neurological diseases (i.e. Alzheimer's disease, spinal cord injuries and traumatic brain injuries) that are accomplished by disruptions and alterations of cellular-mechanical properties, like the upregulation of focal adhesion proteins and the increased expression of intermediate filaments (Kálmán, 2001). At the same time, astrocytes hypertrophy and hyperplasia intensify the stress on the surrounding cells and ECM forming a collagenous scar, which represents one of the main obstacles to axonal regeneration (Meaney, 2015). Finally, ECM proteins secreted by the eye stroma in response to chronic inflammation might alter the mechanical integrity of ECM leading to metaplasia (Nowell, 2016).

In developmental biology, a mechanosensory mechanism has been speculated to be involved in sperm cell penetration of the thick glycoproteic membrane surrounding the oocyte whose stiffness can be modulated by a crosslinking mechanism ruled by the female gametocyte (Baibakov, 2007).

### 1.1.3 Cancer progression

Cancer, like many diseases, is characterized by a compromised tensional homeostasis: it has been reported that tumours are often characterized by an increased stiffness of the tissues and the desmoplastic stroma. At the same time circulating cancer cells are characterized by a softer

mechanical phenotype resulting from a defective mechanosensing ability that allows their penetration and survival on stiffer matrix (Lin, 2015) (Pickup, 2014). This opens up the way to the development of innovative diagnostic tools and raises the possibility to impede cancer progression by preventing matrix stiffening.

An example is the progression of breast cancer shown in Figure 4, in which the endothelial cells that characterize the lumen of the mammary gland interact with the interstitial stroma composed by some structural matrix proteins (collagen, elastin, proteoglycans and glycoproteins) that together with the basement membrane act as a scaffold by cooperating to define the form and the function of the breast. This matrix is softer when surrounding the terminal duct units, where the accumulation of milk causes a compressive stress on the luminal endothelial cells. With prolonged milk stasis, glands undergo involution (Watson, 2006), the secretory epithelial cells die and are replaced by adipocytes and the gland is remodelled to a pre-pregnant state. Failure in this process can result in inflammation and eventually remodelling of the extracellular stroma. The stiffening of this matrix causes the endothelial cells to proliferate and differentiate. In vitro studies revealed the crucial role of matrix compliance in the morphogenesis of epithelial cells: when grown on stiff substrates cell growth is enhanced with loss of cell-cell junction integrity, there is a change in cell shape and focal adhesion structures and the appearance of stress fibers, while the lumen formation is impeded (Paszek, 2005).

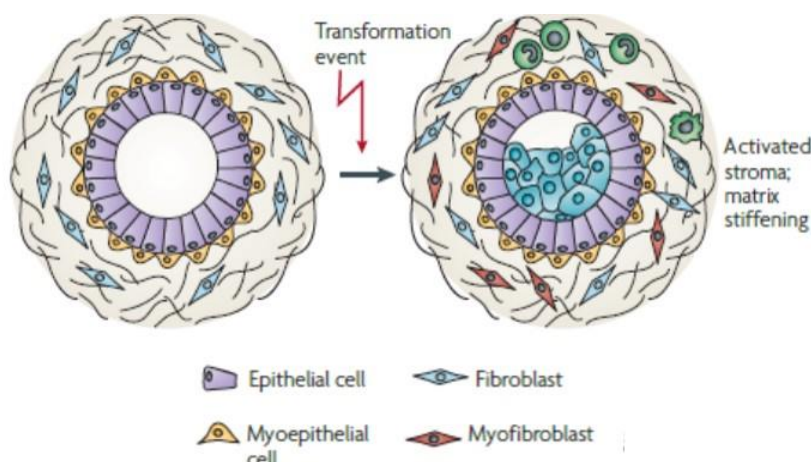


Figure 4: the lumen of the mammary gland is composed by a layer of endothelial cells surrounded by myoepithelial cells and the intestinal stroma. When a transformation event is triggered, the matrix stiffen and changes composition. This variation allows the endothelial cells to change the mechanical phenotype (in blue, inside the lumen) and to proliferate leading later to tumor extravasation (Butcher, 2009)

To summarize, normally cancers are characterized by increased cell-generated forces, increased matrix stiffness and interstitial pressure. There is a different profile of intermediate filaments with respect to normal cells and very often these changes are functional to the cancer diffusion through extravasation. Altered cellular forces could account for the increased invadopodia formation (degradation of the ECM by actin-rich protrusions of the plasma membrane) observed in invasive cells, the increased actomyosin contractility and an altered morphology of focal adhesion complexes (Suresh, 2007) (Dalby, 2004) (Croft, 2004). Tumour-associated compression stress can induce tumour angiogenesis and promote tumour progression.

## 1.2 Mechanotransduction

Mechanical stimuli are perceived through diverse mechanosensitive molecules at the cell membrane including integrins, mechanosensitive ion-channels, G-protein coupled receptors. Through the activation of different mechanotransduction pathways these signals are then transmitted from the cytoskeleton to the nucleus, which results in the transcriptional regulation of specific genes (Luis Alfonso, 2016).

### 1.2.1 Focal adhesions complexes

The main hub of cell-ECM interactions is represented by focal adhesions (FAs), that are composed by many proteins having different function (shown in Figure 5).

The focal adhesion molecules that physically interact with the main components of ECM (fibronectin, collagens and laminins) are integrins.

Integrins are heterodimers composed by  $\alpha$  and  $\beta$  subunits whose specificity is given in mammals by alternative splicing events and the combination of these subunits. While the extracellular domain contacts the ECM, the intracellular one interacts with cytoskeletal actin through the protein of the

inner FA core. The ability to modulate cell tensional homeostasis according to the external perturbations has been called “tensional buffering” (Webster, 2014). A key role in this mechanism is played by an equilibrium between different kind of integrins, that are not homogeneously distributed in different cell locations (Jansen K. A., 2015). The focal adhesion mediated mechanotransduction is associated with the activation (by autophosphorylation) of focal adhesion kinase (FAK). Many other kinases are involved in the mechanosensory machine, like for instance mitogen-activated protein kinase (MAPK). Kinase-mediated phosphorylation also provides the activation of Rho GTPase, another important class of proteins associated with actomyosin contractility (Birukov, 2009).

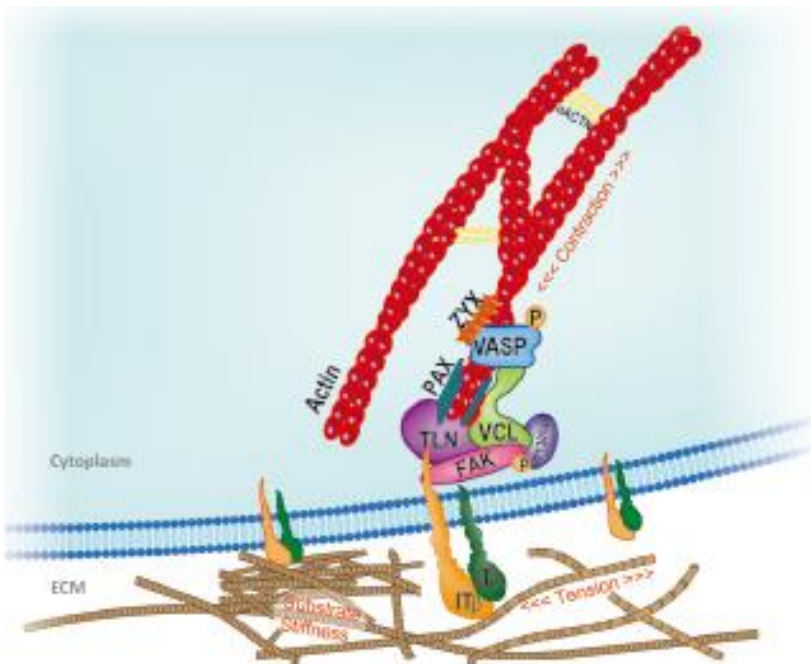


Figure 5: Main components of focal adhesion (FA) interacting with actomyosin cytoskeleton and ECM. IT ( $\alpha$ ) and IT ( $\beta$ ) integrins interact from one side to the cytoskeleton, from the other with talin (TLN), vinculin (VCL), paxillin (PAX) zyxin (ZYX) and p130Cas. Each interaction is ruled by the action of specific kinases whose the main is the focal adhesion kinase (FAK) (Jansen, 2015)

The first molecule that mediates the binding of integrins to F-actin is talin, whose rod domain folding/unfolding balance enables the binding of another key molecule, vinculin. In this configuration vinculin is activated and mechanical signals can be transmitted. The stabilization of FA-actomyosin interactions is also mediated by paxillin (activated through phosphorylation by FAK), zyxin, p130<sup>Cas</sup> (also activated by phosphorylation) and actinins (Martino F. P., 2018).

## 1.2.2 Cytoskeleton

The cytoskeleton is the structure that provides mechanical support to the cells and control their form, motility and contractility. The three main components of the cytoskeleton are shown in Figure 6 and include the actin fibers, the microtubules and the intermediate filaments.

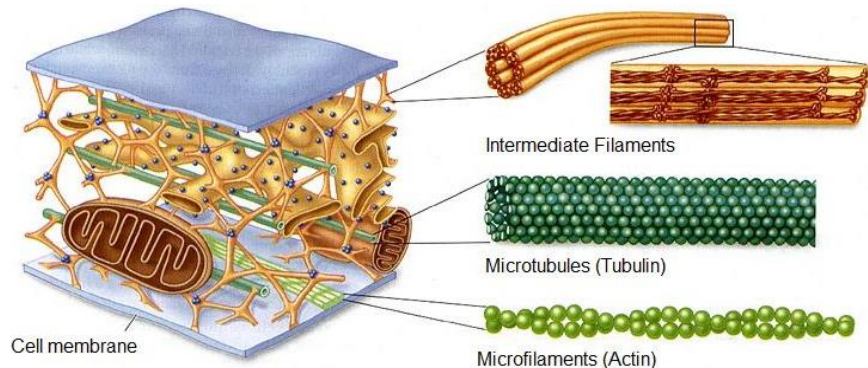


Figure 6: the three main components of the cell cytoskeleton [www.bmscience.net](http://www.bmscience.net)

The actin fibers are composed by two sliding filaments: F-actin and the motor protein myosin II. These two proteins are held together by crosslinking proteins forming the structure called stress-fibers (SFs) (Hotulainen, 2006).

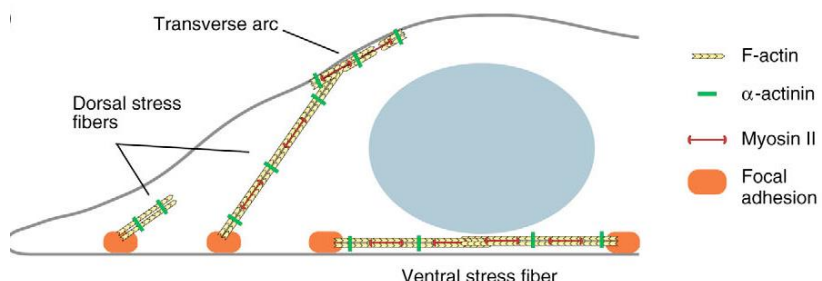


Figure 7: the three main kinds of actin stress fibers in the cell: ventral and dorsal stress fibers and transverse arcs and the connection to FAs (Pellegrin, 2007)

There are three kinds of SFs, shown in Figure 7: the dorsal SFs, the transverse arcs and the ventral fibers. Anchored to one end to FAs, the dorsal SFs act as stabilizers that cannot contract (do not contain myosin). The transverse arcs are only indirectly connected to FAs through the dorsal fibers. Ventral SFs are contractile actomyosin bundles anchored to FAs at both ends and positioned at the cell base. Another subtype of actin fiber is finally the perinuclear actin cap that connects the nuclear

envelop to FAs, in this way mechanical forces are propagate directly from the periphery of the cell to the nucleus (Kim, 2012).

Many actin-binding proteins regulate actin cytoskeleton dynamics, one of these is cofilin, that severs F-actin fibers and allows the depolymerization in G-actin (monomeric form). Cofilin phosphorylation upon mechanical stimulation inhibits this mechanism. The phosphorylation of myosin instead allows the activation of the motor protein generating contractile force. All these processes are activated by Rho associated protein kinase (ROCK) that is also involved in other pathways (Martino F. P., 2018). Microtubules (MTs) are the stiffest cytoskeletal components involved in intracellular trafficking, mitotic spindle formation and cell polarity, also connected to the SFs. The last components of the cytoskeleton are the highly flexible and more stable intermediate filaments (IFs) whose belong nestin and vimentin (Jansen K. A., 2015). Actin and IFs are generally considered to provide the main source of cell stiffness, whereas the more rigid MTs may provide resistance to compression forces.

### **1.2.3 The message delivery to the nucleus**

The mechanical information perceived by the FAs and propagated to the cytoskeleton is transmitted to the nucleus by specific “shuttling” proteins. Their different localized concentration between the nucleus and the cytoplasm is indicative of the mechanotrasduction pathways activation in the cell (Fu, 2018) Among the proteins identified are the tight junction protein ZO-1, the tyrosine kinase c-Abl and the β-catenin that is a component of the cadherin adhesion system at the plasma membrane, identified also as a co-trascritional activator. Zyxin is another protein previously mentioned that moves from the FAs sites to the nucleus following the perceiving of stretching stresses. The same mechanism is used by Paxillin (Martino F. P., 2018).

Another class of co-transcriptional activators, whose presence in the nucleus is unequivocally related to transcription activation of genes involved in cell-matrix interaction and cytoskeleton integrity, are the Yes associated proteins (YAP) and the WW-Domain containing transcription regulator protein 1 (TAZ). These factors are the downstream effectors of Hippo pathway (shown in Figure 8) that acting as a on/off switch in regulating organ shape and organogenesis in response to ECM composition and mechanical stimuli (Piccolo S. D., 2014).

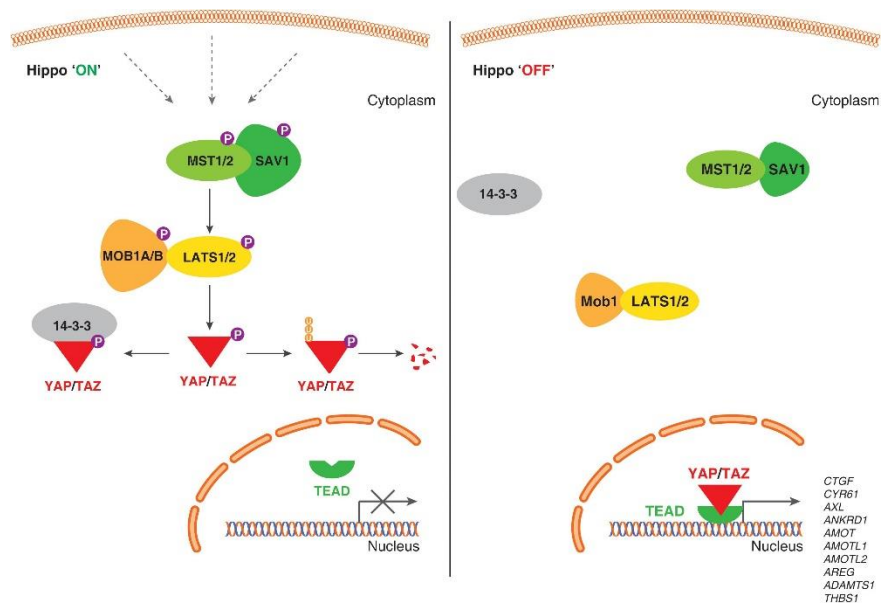


Figure 8: the main downstream effectors of Hippo pathway are the co-transcriptional activators YAP/TAZ that are traslocated to the nucleus to activate the trascritption of genes involved in the mechanotadsuction pathways. This factors, when phosphorylated, can be inactivated by cytoplasmatic sequestration by specific factors or tagged for the degradation (Piccolo, 2014)

YAP/TAZ phosphorylation regulates the persistence in the cytoplasm of this factors, that can be also sequestered to the adherens junctions by the cadherin-catenin system and by ZO-1.

#### 1.2.4 Transcriptional activation

The connection between the nucleoskeleton (the responsible for nuclear shape maintaining and mechanical loading support) and the cytoskeleton resides in the nuclear envelop and is named LINC complex (linker of nucleoskeleton and cytoskeleton). The main components of LINC system are SUN and nesprin proteins that establish strong connections between the inner nuclear membrane and the

outer one (as shown in Figure 9). Moreover, SUN proteins link to the nuclear lamina and in particular with the intermediate filament lamin A, that is connected to the nuclear chromatin directly or through regulatory proteins like emerin, thus affecting gene regulation. Many factors involved in transcription regulation are associated with emerin and lamin A, in this way the activation, or the repression, of transcription can occur in the nuclear pore complexes (NPCs).

Another mechanosensitive transcription factor that dissociates from the cytoskeletal G-actin and is relocated to the nucleus after mechanical stimulation is the mega-karyoblastic leukemia factor (MKL1 also known as MRTF-A) (Martino F. P., 2018).

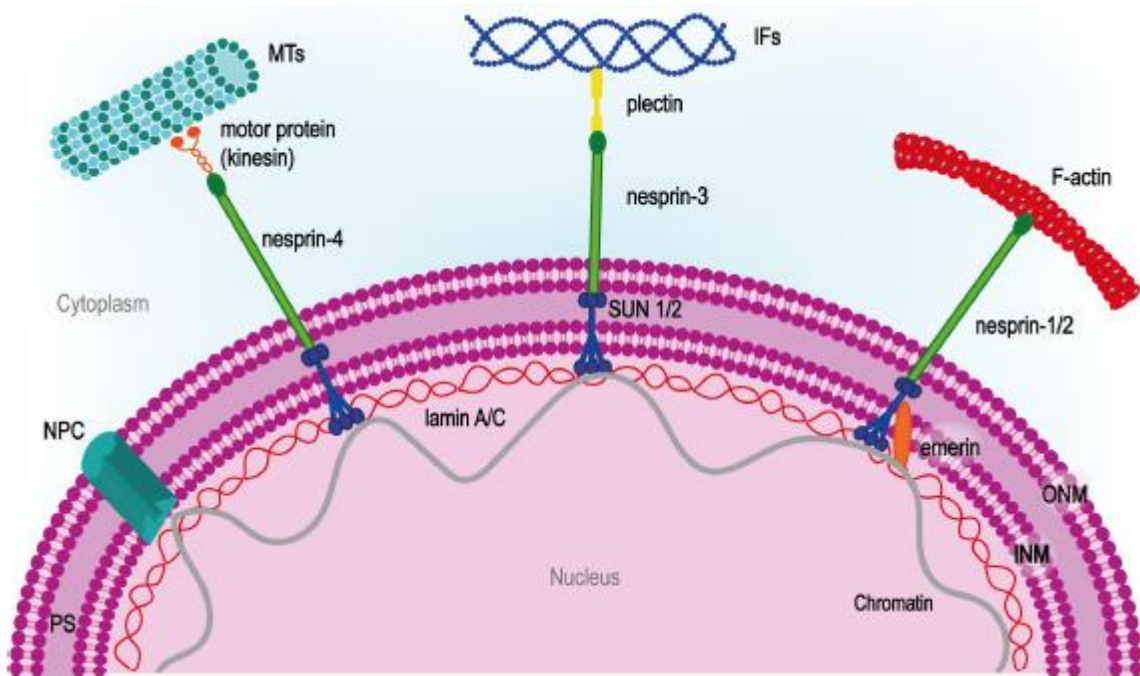


Figure 9: the main components of the LINC complex (linker of nucleoskeleton and cytoskeleton) are SUN and nesprin proteins that connect the inner and outer nuclear membranes to the outer cytoskeleton (Jansen, 2015)

### 1.3 Methods of the mechanobiology

The cell mechanical phenotype can be characterized by the use of different tools that have gained particular popularity in the last years. The mechanobiology tools are many and each of them has a specific application since the information that can be obtained changes according to the technique and the range of forces investigated.

In general, the different methods can be classified into active and passive methods. The first ones measure the cell response to mechanical force application; the modalities, as shown in Figure 10, can differ in the direction of the applied force and the variation in time of the mechanical loading: in measurements of cell stretching and compression the force is perpendicular to the sample, while the application of mechanical shear stress is normally parallel to the surface. Creep and stress-relaxation on the other hand apply a constant force or deformation to the sample for a given time, while in dynamic tests the applied forces oscillate resulting in an oscillatory deformation of the sample.

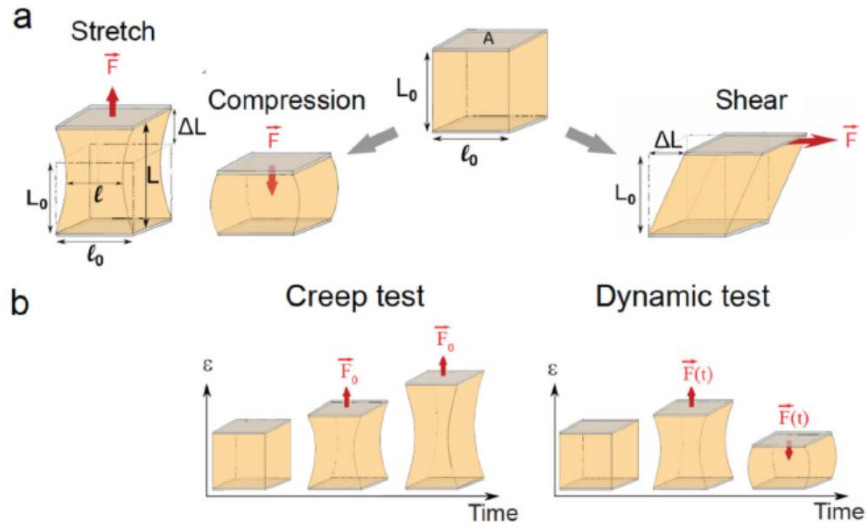


Figure 10: Different active methods for measuring the cell mechanical properties (a) in stretching and compression experiments the stress applied is perpendicular to the sample, while in shear-based methods the force is parallel to the sample, (b) in creep test, constant forces (stretching or compression) are applied for a given time, while in the dynamic test an oscillatory force is applied (Wu, 2018)

The passive methods instead only sense mechanical forces generated by cells without applying any external force.

Active stimulation methods also differ from each other for the range of deformation and stress applied to the cells: micropipette aspiration, parallel plate rheometry cell monolayer rheology (CMR) apply large deformations and the range of the measured force is from few nN to tens of  $\mu$ N, while atomic force microscopy (AFM), magnetic tweezing cytometry (MTC) and optical tweezers (OTs) usually apply small deformation, down to the molecular level. (Wu, 2018). In particular, forces investigated with OTs span from 0.1 to 100 pN while AFM allows the investigation of a wider

range of forces over 4 orders of magnitude, from 10pN to 100nN. These techniques allowed to unveil the unfolding force of proteins like Talin (14pN) and DNA denaturation (30-60 pN). Interaction between antigens and antibodies have been shown to involve forces of 200pN and the forces exerted by cells during mitosis go up to 80 nN.

Different probe geometry and size, different rates of stress application, different force intensities and time domain can give access to different kind of mechanical properties. Therefore, the results obtained with alternative techniques are not always easy to compare and often can be integrated to provide a more complete description of the cell mechanics. Here an overview of the most commonly used techniques is provided.

## 1.4 Active stimulation methods

### 1.4.1 Micropipette aspiration

This method has been widely exploited for the study of neutrophils and granulocytes as well as human or mouse oocytes and embryos.

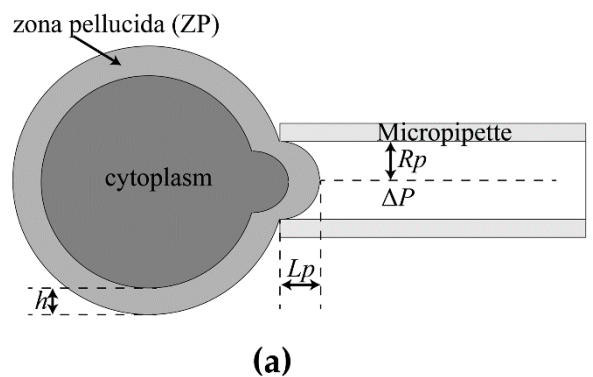


Figure 11: schematic representation of an oocyte suction by micropipette indentation.  $L_p$  is the length of the cell projection,  $R_p$  the radius of the pipette and  $\Delta P$  the pressure applied to the cell (Liu Y. C., 2019).

As shown in Figure 11, it consists of the creation through the aspiration with a micropipette of a cellular hemispherical protrusion. The aspiration of the cell with a pressure exceeding a critical value

will cause the cell to flow continuously inside the pipette. The relation between the pressure applied, the length of the cell projection  $L_p$  and the pipette radius  $R_p$  is the following:  $T_c = \frac{\Delta P}{2\left(\frac{1}{R_p} - \frac{1}{R_c}\right)}$  where  $\Delta P$  is the pressure applied to obtain  $L_p = R_p$ ,  $R_c$  is the cell radius,  $T_c$  is the cortical tension. The range of forces investigated by mean of this technique goes up to 1000nN. (Gonzàlez-Bermùdez, 2019).

### 1.4.2 Optical tweezers (OTs)

Laser trapping methods are particular useful when dealing with forces ranging from 0.1 to 100pN. The working principle mechanism of OTs is based on focusing with a high numerical aperture objective a laser beam onto a dielectric micro-particle. The radiation pressure of the light beam generates forces of which the dominant component is along the gradient of the electric field that is responsible for the particle entrapment at the focal point of the beam. The trap behaves like a linear Hooke's spring. Therefore, by changing the position of the focus it is possible to move the trap position. OTs can be used to perform nanoindentation measurements in which the force-indentation curves are obtained and fitted to the Hertz model to obtain the Young modulus, to globally stretch cells and study their elastic and viscoelastic properties (as shown in Figure 12). The two main configurations are single trap or dual trap systems, less frequently multiple-trapping or angular momentum systems are used.

Another use of this technique is related to active microrheology experiments by inducing the displacement of beads previously injected into the cells by an external force applied through OT. In this way the shear modulus ( $G$ ) can be obtained (Arbore, 2019).

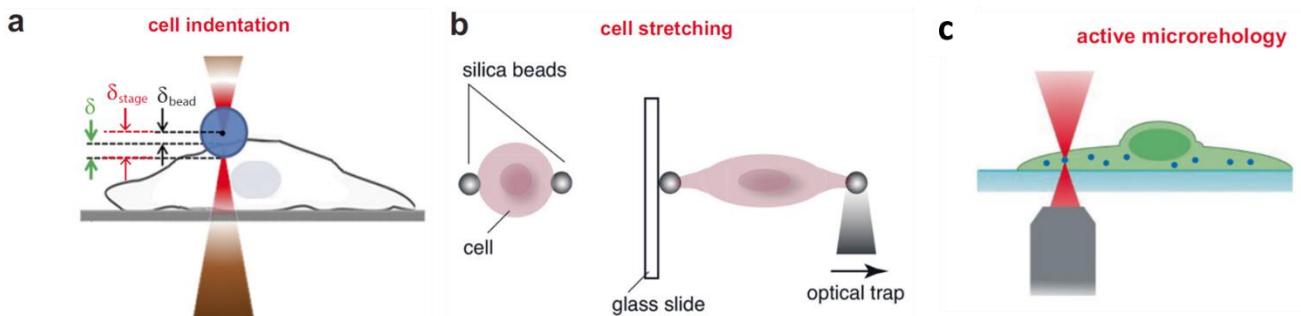


Figure 12: different operational modes of the OTs, (a) cell indentation by a spherical bead, (b) cell stretching through an anchored bead and a optical trapped movable bead, (c) beads moved by OTs can be incorporated inside the cell (Arboe, 2019)

### 1.4.3 Optical stretching

The same working principle as OTs can be used by the optical stretcher that allows to measure the creep compliance and elastic modulus of single cells through the use of a dual-beam optical trap to induce well-defined mechanical stresses on whole cells in suspension, with no need for the use of dielectric particles (Figure 13). The transfer of momentum from the light to the cell provides the generation of forces due to the change in the refractive index at the cell–medium interface. (Guck J. S., 2005). This technique is particularly interesting for the possibility to be integrated into a microfluidic system for convenient delivery of the cells into the trapping region.

The creep compliance profile of cells reveals their composite viscous and elastic properties. The range of the measured forces is the same as OTs (0.1-100pN).

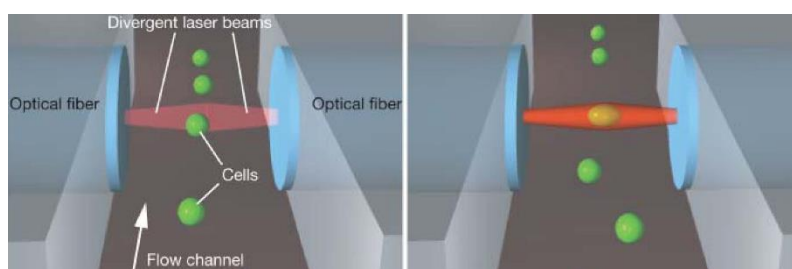


Figure 13: optical trapping of a cell and application of a stretching force to measure the cell deformability and creep compliance (Wu, 2018)

### 1.4.5 Magnetic twisting cytometry (MTC)

MTC, showed in Figure 14, uses a ferromagnetic bead bound to the apical surface of the cells. A controlled homogeneous magnetic field is applied to the cell via magnetic coils, which caused the bead to translocate and rotate. Shear viscous and elastic moduli and the Young's modulus can be calculated on the basis of the magnitude of the bead–cell area of contact, the magnetic field applied and the displacement of the magnetic bead. Different modalities allow also the application of stretching/pulling forces and to decouple torque from stretching forces (Wu, 2018).

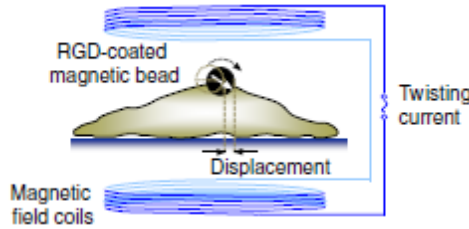


Figure 14: sketch of MTC setup, the cell is probed by the displacement of a magnetic bead ruled by the application of a magnetic field (Wu, 2018)

### 1.4.6 Parallel-plate rheometry

The parallel-plate rheometer allows to extract the Young's modulus and creep compliance. As opposed to the method that will be described below, in the parallel plate rheometry usually the cell deformation and the Young's modulus are measured by stretching the cells rather than by compressing them; for an homogeneous material the two approaches are equivalent, but in case of cells and tissues these two approaches investigate different aspects of the sample and can provide significantly different numbers. A single cell is placed between a rigid plate and a flexible plate of calibrated stiffness  $k$  that is used as a force probe, and the cell is stretched through constant or oscillatory displacements (Figure 15). For oscillatory displacements of plates with frequency  $\omega$ , the elastic ( $E^I$ ) and viscous moduli ( $E^{II}$ ) are weak power laws of the frequency ( $E^I(\omega) \sim E^{II}(\omega) \sim \omega^\alpha$ ). The balance between dissipative and elastic behaviours is expressed by the coefficient  $\alpha$ : a higher exponent signifies higher viscous dissipation, ( $\alpha = 0$  for a purely elastic solid, whereas  $\alpha = 1$  for a

viscous liquid) (Wu, 2018). The parallel-plate rheometer also measures the relaxation and creep functions of individual cells. Forces in the range of 1nN to 10 $\mu$ N can be measured.

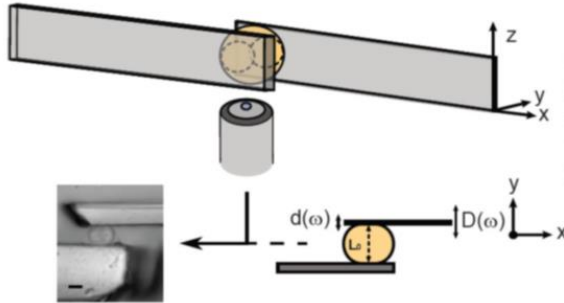


Figure 15: scheme showing the working principle of parallel-plate rheometry in which the cell is placed between two plates and stretched through an oscillatory displacement  $D(\omega)$  applied at the base of the microplate (Wu, 2018)

#### 1.4.7 Cell monolayer rheology (CMR)

Cells are placed between two plates of a rotational rheometer with plate-ring geometry, which operates in the regime of large shear deformations (as shown in Figure 16). Cells form a sparse monolayer, the adhesion on the plates is enhanced by fibronectin coating. The ring rotates around its symmetry axis, which leads to simultaneous shear deformation of the cells. At a certain deformation it is possible to calculate the cell elastic shear modulus (Fernández, 2007) (Wu, 2018).

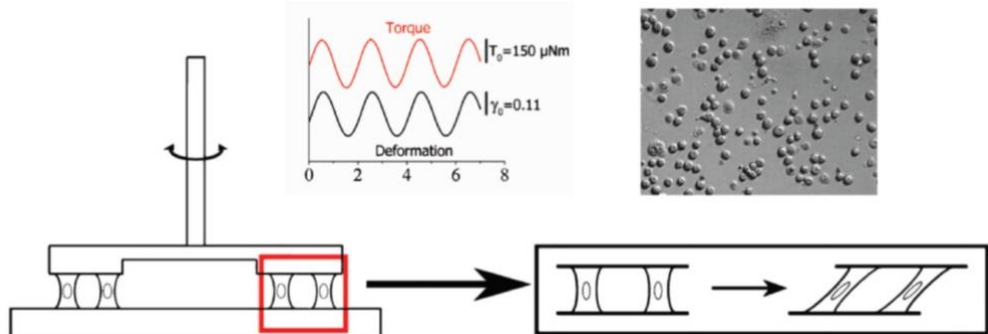


Figure 16: schematic diagram of the CMR, torsional strain is applied to the cells by a rotational rheometer, the shear modulus corresponding to an applied deformation can be calculated (Wu, 2018)

## 1.5 Passive methods

### 1.5.1 Traction force microscopy (TFM)

TFM, allows to study the traction forces generated in cell motility and adhesion to different substrate normally composed by thin hydrogel films with fluorescent beads incorporated (as shown in Figure 17).

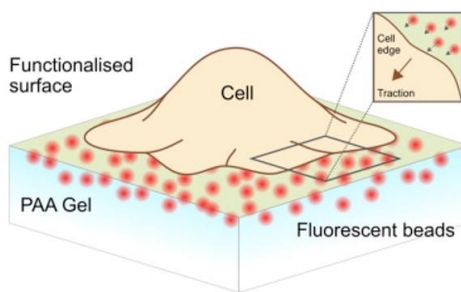


Figure 17: schematic diagram of the TFM working principle, the movement of fluorescent beads inside an hydrogel support are caused by traction forces performed by the adherent cell (Colin-York, 2018)

The bead positions can be imaged in a stressed state (when cells start to contract) and then in an unstressed state (when cells are detached from the substrate by trypsinization). Traction maps derived from the displacements of the beads can be obtained through a variety of computational methods. Polyacrylamide or silicon-based gels are typically used as substrates because both exhibit a linear elastic behaviour, but also ECM-mimicking materials can be employed for more realistic 3D models. However, the non-linear force-displacement response of these substrate prevents a precise quantification of traction forces. The range of forces measured with this technique spans from 2 to 120nN. With this technique the observation of spatio-temporal patterns of forces in more reliable physiological and pathological conditions is possible (Basoli, 2018).

### 1.5.2 Micro-engineered platforms

Microfabricated platforms can be distinguished into two main classes: hard-silicon based devices and soft polymer devices. The first category includes Micro-Electro-Mechanical systems (MEMS)

in which silicon elements deform in response to forces exerted by cells altering their electrical response (Polacheck, 2016). The second category includes soft polymers and gel microsystems obtained through soft-lithography techniques. Among these, microfabricated micropillar arrays (shown in Figure 18) have been applied to the measurement of forces exerted by single cell adhesion sites. The contractile forces deflect the underlying pillars that behaves as simple cantilever with known spring constant. In this way the traction forces can be calculated from optically measured deflections. Micropillar arrays can be coupled to microfluidic channels allowing the measurements of cell contractile forces under laminar shear flow. Moreover, heterogeneous mechanical environments can be obtained by altering the micropillar geometries that influence the substrate stiffness (Yang, 2011) (Gupta, 2015). The range of forces that can be measured here is very wide and goes from 1 pN to 1mN.

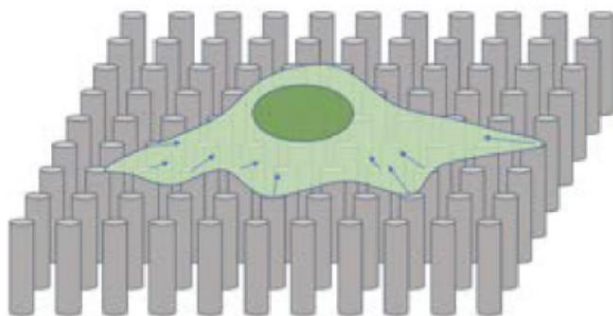


Figure18: micropillar array for measurement of cell contractile forces that can be determined by the deformation of the pillars (Basoli, 2018)



# **Chapter 2**

## **2.1 Basic principles of AFM**

Atomic Force Microscopy (AFM) is one of the most widely used tool for the investigation of the mechanical properties of cells and biological macromolecules. The advantage of this technique is related to the possibility to work in physiological conditions allowing to *in vivo* investigate the mechanisms underlying biologically relevant molecular processes by detecting the changes in the cell biophysical properties.

Depending on the characteristics of the probes, the experimental conditions and the selected range of forces, it can be applied to the study of tissues, cells, viruses, cell membranes and single molecules, like proteins and nucleic acids (Kasas, 2018). The working principle of AFM (Figure 19) is based on a probe, usually a triangular or rectangular cantilever with a tip at the upper end. In imaging mode, the spatial resolution is ultimately determined by the tip size and geometry. The cantilever is moved over the sample in three dimensions (x, y, z) by a computer-controlled piezo actuator. The deflection of the cantilever is proportional to the tip-sample interaction forces and is usually detected by a laser beam focused on the cantilever which is reflected backward to the centre of a photodiode. The displacement of the laser is measured as a voltage response on the photodetector. A feedback loop transmits the electrical signal to the piezoelectric scanner to maintain constant the tip-to-sample distance through the measurement of a suitable reference signal, usually the cantilever deflection or the cantilever oscillation amplitude.

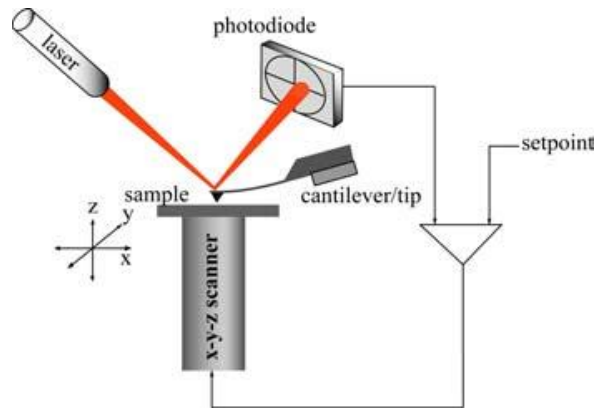


Figure19: AFM main components: a piezoelectric scanner, a cantilever with the tip, an optical lever detection system based on an IR laser beam, a four-quadrant photodiode connected by a feedback loop to the piezo actuator. (**Chtcheglova, 2004**)

## 2.2 Imaging

According to the distance between the tip and the sample, different forces can dominate the interactions, as depicted in Figure 20. Accordingly, it is possible to distinguish different AFM imaging modes: when the tip is far from the surface of the sample, the “Non-contact mode” is based on long range attractive forces (Van der Waal interactions); as the tip get closer to the sample, a change in the derivative of the force-vs-distance curve occurs and the main tip-sample forces become repulsive short-range Coulomb interactions, that area exploited in “Contact mode” imaging. Another mode then allows to cover the gap between the range of applications of these two techniques the “Intermittent mode”. The choice of the imaging mode depends on the sample, the environmental conditions and the biophysical properties that are intended to be investigated.

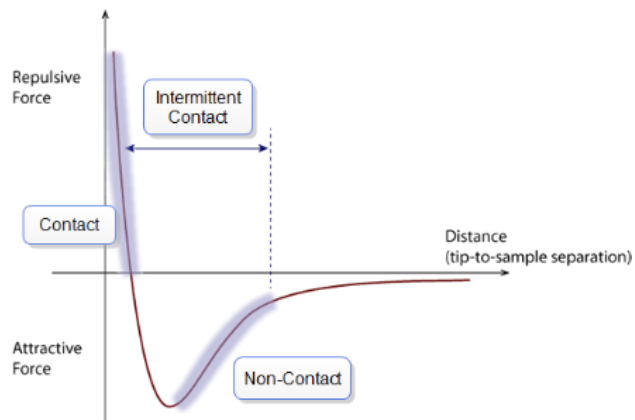


Figure 20: Forces involved in the tip-sample interactions against the tip-sample distance and the different AFM operating modes (Contact, Non-contact and Intermittent contact modes).  
[www.bruker.com](http://www.bruker.com)

### 2.2.1 Contact mode imaging

The main components and working principles are shown in Figure 21.

In this mode the tip is pressed against the sample until a target value of cantilever deflection is reached. Then the sample is raster-scanned through the x-y plane. The change in the sample morphology induces a deflection of the cantilever that is revealed by the variation of the voltage signal on the photodiode. This signal is sent to a controller and compared to the predetermined deflection setpoint value. The resulting error signal is therefore sent to the piezo that adjusts the position in “z” to maintain the tip-sample distance constant. The response time of the feedback system is controlled by the integral and proportional gain that cause the piezo to move faster in “z”. From this operation mode, also called “constant-force mode”, it is possible to have two outputs: the height and so the sample topography and the error signal. In this mode the tip is always in constant contact with the sample and this can damage it because of the lateral shear forces produced especially if dealing with soft biological samples, for this reason it is normally unsuitable for imaging of non-fixed biological samples in liquid.

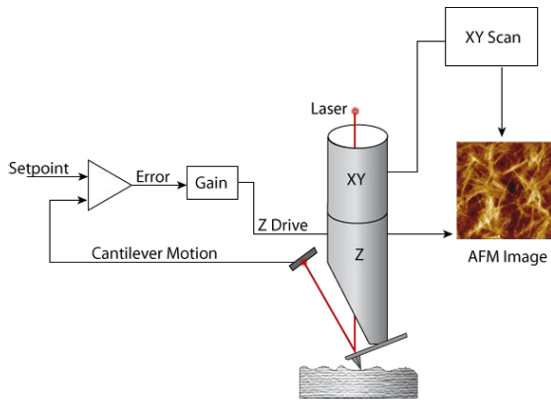


Figure 21: The main components of the costant-force imaging mode. The “gain” regulates the rate of the piezo displacement in response to the feedback signal. This mode allows to obtain mainly the information about the topography of the sample. [www.bruker.com](http://www.bruker.com)

### 2.2.2 Dynamic modes

Dynamic modes differ from the static ones in that the cantilever is oscillated by a driving force at or near its resonance frequency. Depending on the mode, the tip can be only in intermittent contact with the sample (so called “tapping mode”) or not physically interact with the sample in the non-contact regime (Dufrêne, 2017). The intermittent-contact mode is the most used, especially dealing with biological samples in which the frequency modulation is unsuitable because of the intrinsic instability in the feedback control generated by the transition from non-contact to contact that is further complicated by adhesion and attractive interactions between the tip and the sample (Jaafar, 2012).

In tapping mode, the cantilever is oscillated at a given frequency and the amplitude of this oscillation defines the setpoint (Figure 22). Every time the tip touches the sample, there is a decrease in the detected signal amplitude and a shift in the detected signal phase, defined as the delay between the driving signal and the actual oscillation signal of the cantilever, and by comparing this variation to the established setpoint a lock-in amplifier generates an error signal. By a feedback loop this signal is converted to a piezo displacement that by changing the position of the sample in “z” restores the oscillation amplitude and phase.

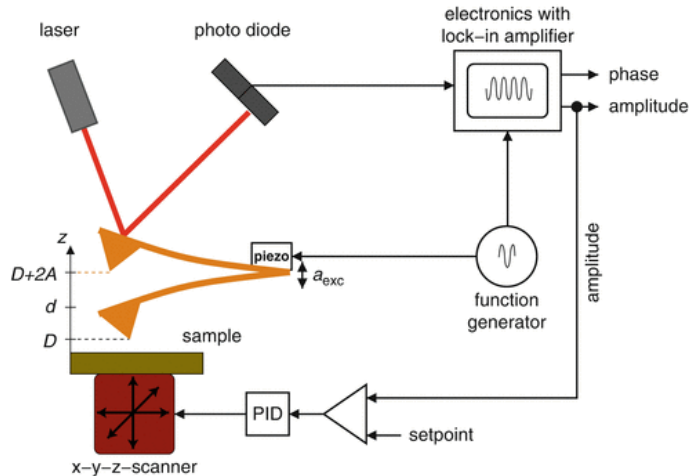


Figure 22: schematic diagram in which the AFM-amplitude modulation working principle is depicted. The main outcome of this technique are topographical informations (from the amplitude variation of the detection signal) and viscoelasticity of the sample (from the phase channel). (**Holscher, 2008**)

From this kind of imaging mode also called “amplitude modulation”, it is possible to obtain two main information: the topography (from the height channel outcome) and the viscoelastic properties of the sample (from the phase channel output). (Figure 23). This last information can be used to produce high contrast images of soft material but the interpretation of the obtained numerical values is generally very difficult because of the interplay of viscous and elastic contribution.

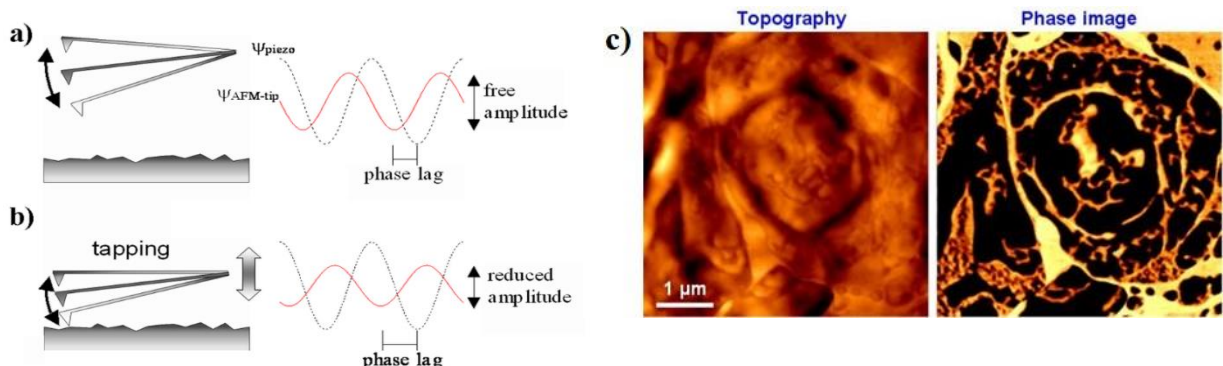


Figure 23: (a,b) variation of phase and amplitude of the detected signal when the probe is in contact with the sample, (c) imaging of two different channels, related to amplitude variation (topography) and phase (sample viscoelasticity) (**Nie, 2011**)

In addition to the mentioned modes, a lot of other approaches have been developed that are meant to provide more precise information about the sample chemical and mechanical properties and to increase the scan rate. Among these, it is worth to mention the multifrequency imaging that is based

on the simultaneous excitation and detection of different frequencies of the cantilever motion and the observation of different related biophysical properties (Garcia, 2012).

## 2.3 Force spectroscopy

### 2.3.1 Single cell force spectroscopy and applications

Other than imaging, one of the most exploited tools for the investigation of mechanical properties of biological membranes, cells and tissues is the AFM-based force spectroscopy. (Krieg M. F., 2019) (Kasas, 2018). The working principle of this mode is based on the approximation of the cantilever to a Hookean spring that is characterized by a defined spring constant ( $k$ ) related to the force ( $F$ ) exerted during the deflection ( $d$ ) by the Hooke's law:  $F = kd$ .

When the cantilever is put in static contact with a cell, the forces exerted by the cell during contraction due to application of an external stimulus or a physiological state, can be measured by the corresponding change in the deflection of the probe. In this way it was possible to unveil the forces associated to cell mitotic and meiotic divisions (Stewart, 2011). At the same time the mechanisms and forces related to cell migrations and protrusions at the leading edge and the tight relationship between the role of actomyosin cytoskeleton and the osmotic pressure in the mitotic rounding (O'Callaghan, 2011) have been elucidated.

On the other hand, a constant force loading can be applied to the cell for a given time and the effects on the dynamics of cell processes can be evaluated. For instance, the acceleration of the mitotic progression was observed by the application of small forces (5nN) but when forces exceed 100pN the mitotic arrest was accomplished (Cattin, 2015). On the contrary, if a constant deformation is applied to the cell, it is possible to evaluate the cell viscoelastic properties by observing the variation of the force exerted by the cell during the relaxation (Moreno-Flores, 2010). The cell mechanical properties like viscosity and elasticity could be also evaluated by AFM-indentation in which the cantilever is pressed against the cell to reach a given depth within the cell, while recording the forces

applied. In this way, force-indentation curves can be recorded that express the relation between the indentation depth and the applied force. When the probe is detached from the cell, another important information can be obtained: the cell-cantilever adhesion, that can be exploited to evaluate interactions with specific molecules according to the cantilever functionalization. If cell is held for a while, it can be attached to the probe and this system can be employed to evaluate cell-substrate or cell-cell interactions.

In the last years a lot of studies have allowed to deepen our knowledge about cellular and molecular processes involved in cell adhesion (Sullan, 2014). In particular adhesion studies allows to discriminate between different kinds of cell links to different surfaces and to calculate the forces involved in the rupture of specific receptor-ligands bindings, as well as to determine the kinetics of these interactions (Krieg M. H., 2008).

The combination of force spectroscopy with other techniques like patch clamp technology and FRET, enabled to monitor the electrical properties of mechanical stimulated conductive cells (like neurons and beating cardiac cells) or by epifluorescence microscopy to detect the calcium influx related to the opening of mechanosensitive ion channels, like Piezo channels and the effect of the concurrent presence of ECM proteins on this mechanism (Gaub, 2017) .

### **2.3.2 Calibration of the probe**

One important step is the calibration of the probe that allows to determine the force that corresponds to the cantilever deflection by calculating the sensitivity ( $s$ ) and the spring constant ( $k$ ) of the cantilever. When the cantilever is pressed against an hard substrate, in the contact region the cantilever deflection is equal to the displacement of the piezo. If the variation of the voltage signal ( $V$ ) on the photodiode is plotted against the piezo displacement (nm), as shown in Figure 24, from the slope of the curve it will be possible to calculate the sensitivity (nm/V).

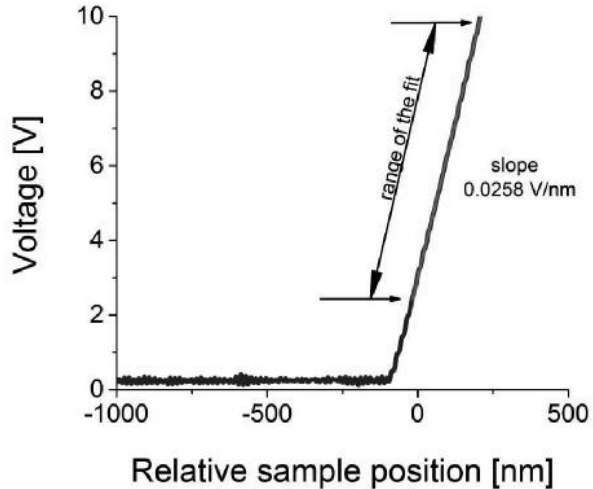


Figure 24: From the slope of the calibration curve we can calculate the sensitivity (nm/V). (Lekka, 2017)

Then, the effective spring constant (nN/nm) of the cantilever is normally calculated by the thermal noise method: the free oscillations of the cantilever provide the thermal energy associated to this motion  $\langle x^2 \rangle$  where  $x$  is the vibration amplitude that is connected to  $k$  of the cantilever by the following equation:

$$\langle x \rangle = \sqrt{\frac{k_b T}{k_{\text{cantilever}}}}$$

in which  $k_b$  is the Boltzmann constant,  $T$  the temperature.

By the calculation of these two parameters, the change in the voltage signal on the photodiode (V) related to the cantilever deflection will be converted into a force signal by the Hooke's law:

$$F (\text{nN}) = k \left( \frac{\text{nN}}{\text{nm}} \right) s \left( \frac{\text{nm}}{\text{V}} \right) V(\text{V})$$

### 2.3.3 Creep and stress-relaxation

These approaches consist in the application of a given mechanical loading or a certain deformation to the cell that are maintained constant in time (Moreno-Flores, 2010). In the first case, creep experiments, the deformation of the sample under constant force loading can be calculated by the

variation in the vertical position of the cantilever. The cell's deformation will increase in time in an exponential way (as shown in Figure 25). From the fitting through the proper mechanical model, the ratio of the Young modulus ( $E$ ) and the viscosity ( $\eta$ ) of the cell can be obtained. The second approach consist in the “constant height mode”, in this case the vertical position of the cantilever will be set constant while force exerted by the cell on the cantilever will be obtained measuring the time evolution of the cantilever deflection. The force will decay exponentially in time and by the fitting procedure (the more used model is the Zener model) it will be possible to calculate the relaxation time ( $\tau$ ) that is related to the sample Young's modulus and viscosity by the following relation:  $\tau = \eta/E$ . The main assumptions on which these methods rely are that contact area is maintained constant during the measurement and the cell is subjected to a sudden and constant deformation.

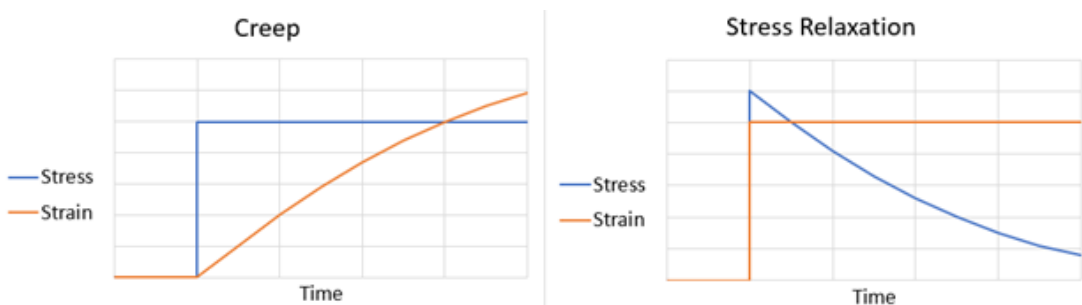


Figure 25: Creep experiments measure the exponential increase of the cell deformation during the application of a constant force loading. Stress-relaxation measure the exponential decay of the force exerted by the cell on the cantilever during the application of a constant strain. (Liu C. P., 2015)

### 2.3.4 Indentation

The main principle of AFM-indentation is based on the acquisition of the force-distance (F-d) curves that are the resultant plot of the cantilever deflection versus the displacement of the z-piezo. After the calibration, the cantilever deflection is expressed in force (nN) and the subtraction of the cantilever bending from the piezo displacement in the contact region allows to calculate the indentation ( $\delta$ ). Therefore, F-d curves are converted into force-indentation (F-  $\delta$ ) curves.

A representation of a force-indentation curve is depicted in Figure 26. The cantilever is approached to the sample (approach curve, in red in the figure), at the contact point the tip-to-sample interaction forces cause the bending of the cantilever toward the sample caused by attractive van der Waals forces; continuing the approach, in the contact region, repulsive forces become dominant and the cantilever is deflected in the opposite direction. Then the tip is moved away from the surface (retraction curve, in blue in the figure) and enter again in the range of attractive forces exerted by the sample, until it detaches from the sample.

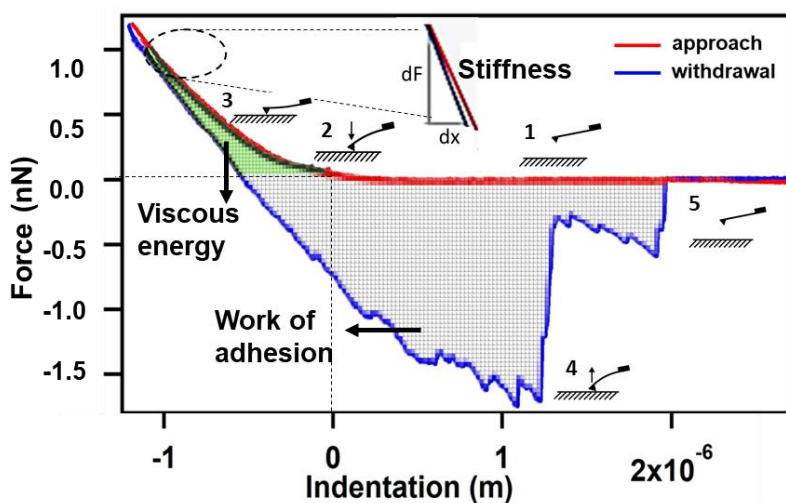


Figure 26: The cantilever in non-contact region (1) is approached to the sample, at the contact point (2) the attractive forces exerted by the sample cause the bending of the cantilever toward the sample, while as the cantilever enter in the contact region (3) the repulsive forces cause the cantilever deflection in the opposite direction. As the cantilever is moved away from the surface, the attractive forces cause again the bending toward the sample (4) until the cantilever detaches from the sample (5). the analysis of force-distance curve provides different kind of informations: the stiffness of the cell, the work done to detach a cell (adhesion energy) and the viscosity expressed by the dissipated viscous energy

Several information can be obtained from a F- $\delta$  curve: from the slope of the approach curve in the contact region, the sample elasticity expressed by the Young's modulus ( $E$ ) can be calculated by fitting the curve through a specific mechanical model. On the other hand, the contribution of non-specific adhesion or the interaction of the tip (functionalized with interacting molecules) with specific ligands can be detected in the retraction curve up to the tip "jump-off-contact" (Friedrichs J. L., 2013).

Moreover, from the hysteresis between the extension and the retraction curves it is possible to infer the occurrence of a plastic or an elastic deformation of the sample (Butt, 2005). In particular, the

dissipated viscous energy related to the sample viscosity can be calculated by integrating the area between the trace and the retrace curve in the positive range of forces (Wang, 2021), while the area between the approach and the retraction curve in the negative range of forces identify the adhesion energy.

### 2.3.5 Single Cell adhesion

Cell adhesion studies allow the investigation of the cell surface specific or non-specific receptors (Friedrichs J. L., 2013) (Puecha, 2006). Briefly, the cantilever is coated with specific molecules to increase the cell-cantilever interactions: lectins (that specifically recognize sugar groups on the cell membrane), antibodies, poly-lysine (by electrostatic interaction with negative charged cell membrane) or ECM proteins (like collagen, laminin, fibronectin). Then the cells, suspended in the measurement medium, are put on a weakly adhesive surface and left equilibrate for a while. At this point the cell capture occurs: the cantilever is gently brought into contact with a single cell and a given force (in general around 500pN) is applied for few seconds. Thereafter the cantilever is retracted and cells are allowed to firmly attach for 5-15 min. The investigation of cell-substrate or cell-cell interaction can be performed and the probe-cell is approached with the surface of interest. A given force is then applied for a while and then the cantilever is retracted with a constant speed. The retraction curve will give information about the interactions of the two surfaces (Figure 27): the presence of membrane tethers ( $t$ ) and the number of “step events” ( $s$ ) can be detected. Tethers are membrane protrusions that form when a receptor detach from the underlying cytoskeleton, while step events define adhesive units that are connected to the cell cortex. Membrane tether force provide information about the membrane properties (tension and viscosity) and if the number of bonds tethering the membrane is known, the force clamp applied by the cell membrane tether can also be used to determine the lifetime of the bond under constant force. Other important information that can be derived is the work of detachment that comprise the area between the approach and the retraction

curves in the negative force region and describes the energy dissipated during the adhesion, the maximum detachment force and the adhesion rate, the fraction of curves with at least one detected force step with a peak force greater than a given threshold.

The use of specific molecules that act as inhibitor of specific adhesion sites are generally used to distinguish the contribution of specific and non-specific adhesion. Important parameters are the contact time and the contact force: the probability of multiple bonds contributing to adhesion increases for longer contact time and higher contact force.

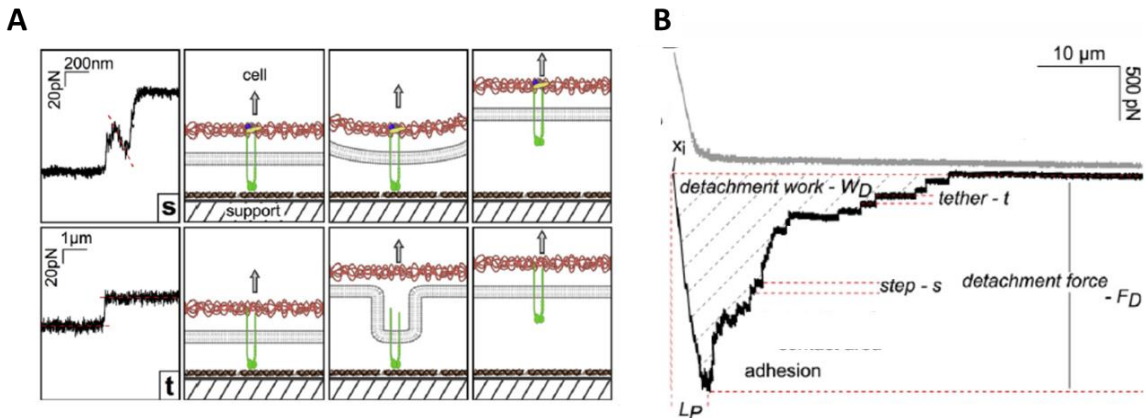


Figure 27: (A) the difference between step events (s) in which the pulled receptor is anchored to the cytoskeleton and tether events (t) in which the pulled receptor is not anchored to the cytoskeleton, (B) the different informations that can be extrapolated from the retraction curve. (Friedrichs, 2013)

## 2.4 Indenters and experimental conditions

AFM measurements can be performed with different indenters. The main common used are depicted in Figure 28.

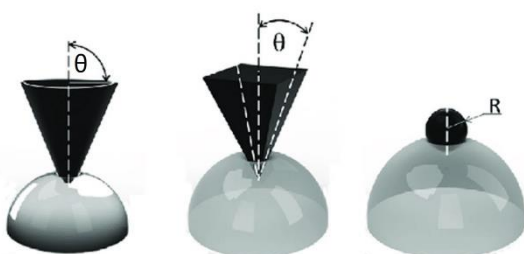


Figure 28: three different indenter geometries used to probe the cell conical, pyramidal and spherical tips. (Cárdenas-Pérez, 2018)

Conical and pyramidal indenters are preferred for imaging purposes or when dealing with proteins and molecules because the small size of the tip is related to the increased resolution of forces detected and topographical details (Krieg M. F., 2019). Conical and pyramidal tips because of the local sensitivity are also more suitable for the investigation of the mechanical properties of the cellular membrane or actin cortex. On the contrary, spherical indenters are preferred for nanoindentation measurements of cells because of the larger probe radius that results in higher contact area and better allows to detect the mechanical properties of the whole cell. Moreover, a small deviation from the ideal tip geometry affects the accuracy of the results during nanoindentation experiments. The higher variability of the Young's modulus values obtained with conical or pyramidal indenters is mainly related to the impossibility to determine with a high accuracy the curvature radius of these probes compared to the spherical indenters. Also the regions of the cells probed by different tips are different and can result in different numbers: for instance the elastic moduli measured by pyramidal tips resulted four times higher compared with those measured by spherical tips probably because of the higher tip penetration that could sense regions near stiff actin filaments (Hoh, 1994). Finally, tipless cantilevers are used for adhesion measurements, creep or stress-relaxation. In that case the presence of the tip could negatively affect the result of the measurement.

Other conditions that need to be considered are the cell morphology and the cell type: the nuclear distance from the cell surface is higher in rounded cells than in spread adherent cells (Chen J. , 2014).These factors have to be considered when choosing the indentation depth and the indenter shape.

## 2.5 Mechanical models for living cells

When dealing with cell mechanics, the main issue is about the choice of the right model to fit the data. Cells are anything but homogeneous materials, composed by different structures with different

mechanical properties of which the main ones are the cell membrane, whose mechanical characterization is difficult because of its small thickness (about 5-8 nm), the actomyosin cortex (100-1000 nm thick) from which derives the main elastic contribution, the cytoplasm that is thought the main responsible of the cell plastic deformation and finally the nucleus (Krieg M. F., 2019). According to the kind of experiment performed (nanoindentation or stress-relaxation) and the chosen probe (spherical, pyramidal, cylindrical, conical), different mechanical models can be used to describe our system. Moreover, other parameters have to be carefully considered like for instance the indentation depth and the rate of the measurement (Medalsy, 2013) (Snijder, 2012). In particular the viscous forces of biological systems increase with the indentation speed and can be reduced by slowing down the rate of scanning (Rigato A. M., 2017). Nevertheless, too slow indentation rates can cause the biological systems to remodel and respond to mechanical cues. Indentation depth of at least 400 nm would be needed to avoid the dependence of the results on the inaccuracy related to the identification of the instant and the position at which the tip-sample contact is established on the vertical scale, however with respect to the cell heights this depth is most of the time too close to the limit of indentation assumed by most of the models (Rigato A. M., 2017).

Two kinds of approaches are followed in the description of the mechanical models: the micro/nanostructural approach that considers the cytoskeleton as the main structural component and focuses on cytoskeletal mechanics and the continuum approach. Here we decided to address our attention only on some continuum models that consider the cells as comprising materials with certain continuum material properties.

### 2.5.1 Linear elastic solid models

In these models the whole cell is usually assumed as homogeneous without considering the distinct cortical layer. The equation describing the relation between the applied stress ( $\sigma$ ) and the strain ( $\varepsilon$ ) for a linear elastic solid material is  $\sigma = G\varepsilon$  where  $G$  is the shear modulus and is related to the Young

modulus  $E$  by  $E = 2(1 + \nu)G$  where  $\nu$  is the Poisson's ratio. These models are particularly used when applied to AFM indentation measurements on adherent cells and different models exist according to the geometry of the indenter.

In the case of a cylindrical indenter the force-displacement relation will be given by:

$$F = \frac{2ER}{(1 - \nu^2)} \delta$$

Where  $R$  is radius of the indenter and  $\delta$  the indentation depth.

If the geometry of the indenter is conical, the Sneddon model is applied. In this case the force-displacement relation is given by:

$$F = \frac{2Etan\alpha}{\pi(1 - \nu^2)} \delta^2$$

Where  $\alpha$  is the semi-included angle of the conical indenter.

For a pyramidal indenter the constitutive equation is the following:

$$\frac{3}{4} \frac{E}{(1 - \nu^2)} tan\theta \delta^2$$

Where  $\theta$  is the angle of the pyramidal indenter.

When the indenter is a spherical tip, the force-displacement relation will be the following:

$$F = \frac{4}{3} \frac{E}{(1 - \nu^2)} \sqrt{R} \delta^{\frac{3}{2}}$$

This is the Hertz model and is one of the most used models in AFM nanoindentation measurements.

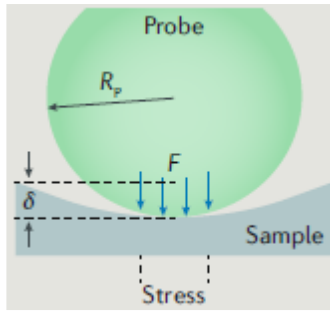


Figure 29: a spherical probe with radius  $R_p$  indenting a sample with a certain indentation depth ( $\delta$ ). (Krieg, 2019)

This model (depicted in Figure 29) relies on some major assumptions: the probe is considered a perfect shaped sphere perpendicularly indenting a non-corragated surface, but both the indenter and the sample surface are not smooth at the nanoscale. Then strain and stress depend linearly on the elastic Young's modulus and the deformation is fully elastic. However, cells exhibit viscoelastic behaviour as results from the presence of hysteresis between the approach and the retraction curves. A more reliable stress-strain relationship must include the viscosity coefficient  $\eta$  ( $\tau = \eta d\gamma/dt$ ). Another important factor is the indentation depth: in order to avoid the substrate contribution to the measurement, no more than the 10% of the cell thickness must be indented. Finally, this model does not include the presence of other interactions like adhesion or friction between the contacting surfaces. Also, in this case, when dealing with biological samples is not possible to exclude the presence of these two phenomena. Alternatively, other models have been developed that take into account adhesive effects: Derjaguin–Müller–Toporov (DMT) and Johnson–Kendall–Roberts (JKR) models. However, in literature there is a solid consensus for the adoption of the simpler model provided by Hertz, and a more detailed data analysis would lead to the impossibility of comparing our data with others'. Therefore, we will adopt the Hertz model throughout the whole experimental section and thus the other models are not treated in this thesis.

## 2.5.2 Maxwell model

The Maxwell liquid drop model (depicted in Figure 30) consists of a prestressed cortical shell containing a Maxwell fluid with a characteristic elasticity expressed by the Young's modulus ( $E$ ) and viscosity ( $\eta$ ) represented as a dashpot and a spring in series. The force will decay in time in an exponential way according to the following equation:

$$F(t) = F_0 \exp\left(\frac{-(t - t_0)}{\tau}\right)$$

where  $\tau$  is the relaxation time can be defined as  $\tau = \eta/E$ .

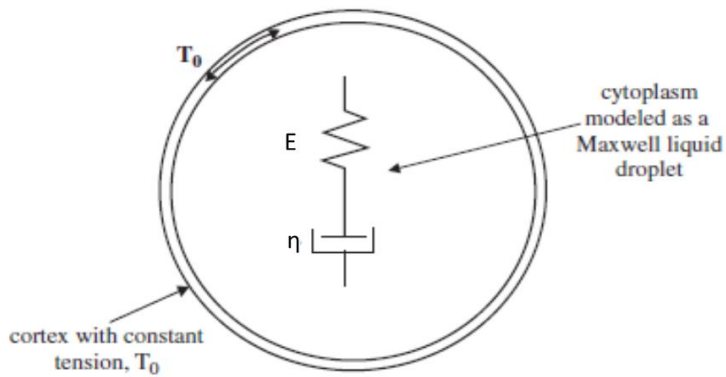


Figure 30: the main components of the Maxwell model are a cytoplasm modelled as a Maxwell liquid droplet (modelled by a spring and dashpot in series) surrounded by a constant tension cortical layer. (Lim C. T., 2006)

Unlucky, it could not fit the experimental data in the case of larger deformations unless the values of cell elasticity and viscosity increase continuously. However, the importance of this model relies in the insertion of an elastic and a viscous components and the more reliable consideration of the cytoplasm as a viscoelastic compound.

### 2.5.3 Linear viscoelastic solid model

This model (exemplified in Figure 31), also known as the Zener model, has been developed to take into account the cells viscoelastic behaviour under a given set of loading conditions.

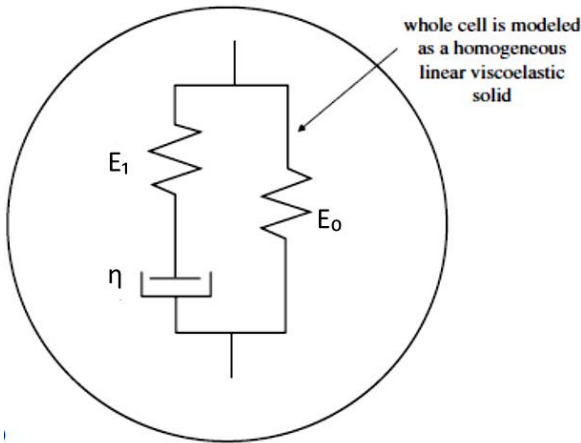


Figure 31: The linear viscoelastic solid model consists of a spring in parallel with a spring and a dashpot in series. (Lim, 2006)

Under a constant stress (creep experiment), the material will deform to some strain, the main contribution is initially given by the elastic portion of the strain. After that it will continue to deform asymptotically approaching a steady-state strain. This is the retarded portion of the strain and will include the contribution of a viscous and elastic element as described by the Maxwell model. In a similar way, the two elastic and viscous elements will contribute to the stress-relaxation measurements in which a given strain is applied to the cell and the exponential decay of the force exerted by the cell in time is monitored. The linear viscoelastic solid model can be represented with an elastic element with a defined  $E_0$  value connected in parallel with another elastic element ( $E_1$ ) and a viscous element ( $\eta$ ) in series.

The constitutive relation of this model takes the form:

$$F(t) = F_0 + F_1 \exp\left(\frac{-(t - t_0)}{\tau}\right)$$

In this way both the creep and stress relaxation behaviours of a viscoelastic material could be described in a more accurate way respectively to the Maxwell model.

## 2.5.4 Generalized Maxwell model

To better describe the creep and stress relaxation behaviours of cells the general form of the linear viscoelastic model is applied, also called Maxwell-Wiechert model (shown in Figure 32). It observes that the relaxation does not occur at a single time, but with a superposition of different decay times, representative of the different viscoelastic contributions present in a cell. Therefore it is represented by having as many spring-dashpot Maxwell elements as necessary to represent the distribution. To describe the behaviour of most of the cells two Maxwell elements are sufficient that can be assigned to cell membrane and cytoplasm (Karcher, 2003).

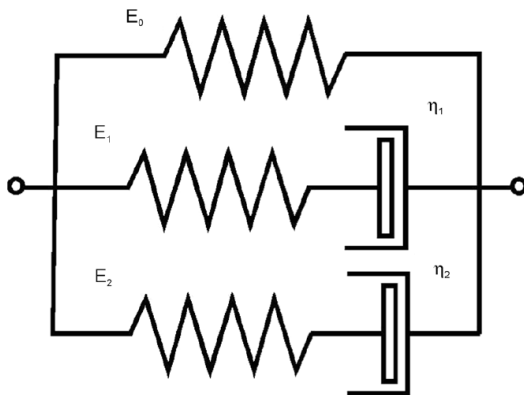


Figure 32: the generalized Maxwell model relies on the assumption of different cellular components having a characteristic viscoelastic behaviour represented here spring-dashpot elements connected in parallel.

For stress-relaxation, the force  $F(t)$  decays biexponentially:

$$F(t) = F_0 + F_1 \exp\left(\frac{-(t-t_0)}{\tau}\right) + F_2 \exp\left(\frac{-(t-t_0)}{\tau}\right)$$

To conclude, according to the experiment that is performed and the kind of indenter, we can choose different mechanical models, only the most important for our purpose are described here, but many others exists and can be more appropriated for describing the mechanics of other systems like the indentation of viruses for which the indentation of a thin and hard protein shell enclosing a compact nucleic acid core is poorly described by Hertzian models. Other models can be used for describing the complex mechanics of the cytoskeleton, like the poroelastic model (also called biphasic model) that treats separately the two fluid and solid phases of this cellular component.



# Chapter 3

## 3.1 Introduction

Thyomosin  $\beta$ 4 (T $\beta$ 4) is a highly conserved polypeptide identified as a significant sequestering agent of monomeric actin (G actin) in mammalian cells, involved in the actin cytoskeleton's reorganization during cell movement (Sanders, 1992). It plays an essential role in wound healing: migration of keratinocytes and endothelial cells (Malinda, 1997), stimulation of angiogenesis (Smart, 2007), recruiting and supporting the differentiation of progenitor cells at the injury site (Sosne, 2002), reducing inflammation and immunomodulatory activity. In recent studies, its role in cancer development and progression was demonstrated: in human melanoma cells T $\beta$ 4 is a component of focal adhesion (FA) and plays a role in forming these structures. Cells with low TMSB4X (T $\beta$ 4 encoding gene) expression levels form a higher number of FAs than cells with high TMSB4X expression levels. However, these FAs were of a smaller size than those observed in the cells with a high T $\beta$ 4 synthesis level (Makowiecka A. M., 2019) (Figure 33).

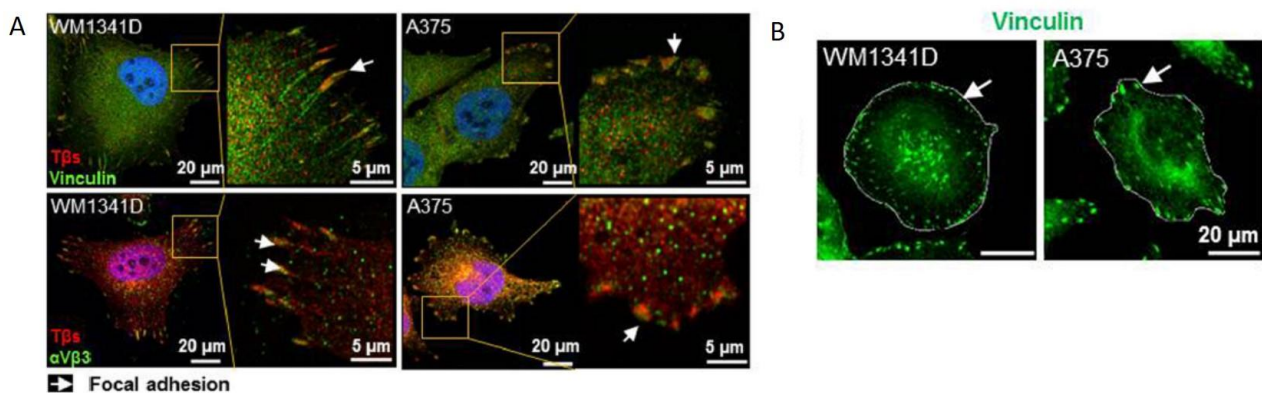


Figure 33: FAs localization in two melanoma cell lines WM1341D and A375 expressing respectively low and high levels of T $\beta$ 4. (A) co-localization of two FA markers (Vinculin and the integrin  $\alpha$ V $\beta$ 3) with a marker for T $\beta$ s (comprising three different kinds of Thyomosin  $\beta$ ), allowing to deduce the presence of these polypeptides in the FA sites. (B) difference in the size and number of FA sites in the two cell lines

Moreover, the silencing of TMSB4X expression in melanoma cells affected their adhesion, migration, and invasion abilities (Makowiecka A. M., 2019) (Figure 34).

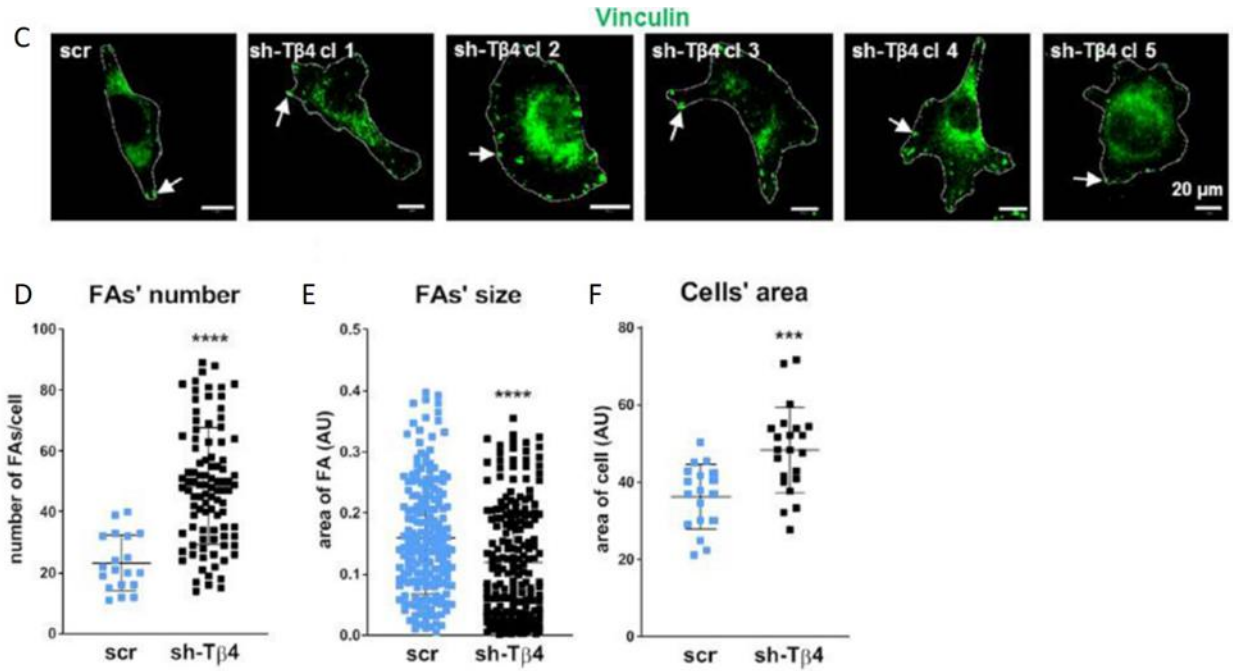


Figure 34: (C) Location of FAs in control A375 cell line (scr) and four different clones in which TMSB4X was silenced. As can be noticed, and is highlighted in the plots below (D-F), there is a change in the number (higher in the clones) and the size of focal adhesions (that are smaller in the clones) and also in the area of the cell spreading. The adhesion assay showed an increased adhesion to Matrigel of the clones with respect to the control line.

In tumors and established cancer cell lines, there is a subpopulation of cells manifesting stem cell features: cancer stem cells (CSCs), also called tumor-initiating cells (Scatena, 2012). CSCs are characterized by some standard features, i.e., self-renewal, differentiation to other types of tumor cells, resistance to chemotherapy, and radiotherapy (Kondo, 2012). The presence of CSC cell populations was reported also in melanoma cell lines (Fang D. N., 2005). In recent years, the involvement of Tβ4 in cell stemness and differentiation has been unveiled in different cell types (Molinari, 2009) (Ricci-Vitiani, 2010) (Ji, 2013). In particular, the cellular levels of some typical stemness markers has been investigated.

Expression of Myc proto-oncogene protein (c-Myc) has been connected with tumorigenesis in mouse models and observed in up to 70% of human cancers (Dang, 2012). It has been shown that the expression of Nanog is involved in the regulation of the epithelial-mesenchymal transition (EMT)

and chemoresistance in ovarian cancer (Qin, 2017). Sox2, on the other hand, is expressed in multipotential neural stem cells and is essential to maintain their proliferative potential (Ellis, 2004). Stem cell differentiation is very often related to a change in the actin cytoskeleton and cell mechanical properties (Fan, 2019). It has been shown that induced pluripotent stem cells (iPSCs) have a less developed cytoskeleton than fibroblasts: while in paternal fibroblasts multiple thin actin stress fibers were aligned across the cell body, human iPSCs cells were characterized by thick ventral stress fibers forming “an actin fence.” Instead, AFM indentation measurements of mouse embryonic stem cells (mESC) revealed significant differences in the mechanical phenotype of early differentiated mESCs cells and undifferentiated ones: the first were 3 times stiffer than the second due to the increasing filamentous actin density and alterations in nuclear cytoskeleton composition (Närvä, 2017)

It has been demonstrated for various tumour types that the cells with higher metastatic potential exhibited decreased stiffness (Xu, 2012) (Andolfi L. B., 2014). For this reason, in this study the contribution of T $\beta$ 4 in melanoma cell cytoskeleton organization and mechanical properties in correlation to their stemness features was evaluated. For this purpose, A375 cells with a lowered level of T $\beta$ 4 (sh-T $\beta$ 4 clones) were examined. Additionally, two melanoma cell lines: A375 and WM1341D, in which endogenous levels of T $\beta$ 4 are, respectively, high and low were also examined. The objective of this study is trying to uncover the interplay between mechanics and stemness in melanoma cells with respect to T $\beta$ 4 levels.

## 3.2 Stemness state evaluation

### 3.2.1 Cell transformation potential

Cellular anchorage-independent growth ability was evaluated by performing a soft agar colony formation assay. Cells are included into agar matrix into the presence of specific growth factors, the detail of the procedure are reported elsewhere (Makowiecka A. M., 2021) (Borowicz, 2014). Under

the test conditions, only cells exhibiting stem cell features can initiate a colony. A higher number of created colonies characterized A375 cells, on average 25, compared to WM1341D cells, which formed an average of 18 colonies (Figure 35 A,B). Moreover, colonies formed by A375 cells were ~15-times larger than those of WM1341D cells (Figure 35 C). In the cells with a lowered level of T $\beta$ 4, a diminished abilities to form colonies was observed in comparison to control cells (scr) (Figure 35 D–F). The average number of colonies was 36 for sh-T $\beta$ 4 cells and 45 for scr cells, and the area of colonies formed by sh-T $\beta$ 4 cells was smaller by about 15% comparing to scr cells (Figure 35 F). The cells with a higher level of T $\beta$ 4 were characterized by an increased ability to initiate colony formation, which were more prominent in size. Though these data show that T $\beta$ 4 level lowering affects the number and area of colonies, analysis of these parameters for separate clones give different results to diminished TMSB4X expression. These results imply that A375 cells can form colonies in soft agar and the silencing of TMSB4X expression leads to alterations in these cells' ability to form colonies in soft agar. However, not all the clones exhibited this specific behaviour.

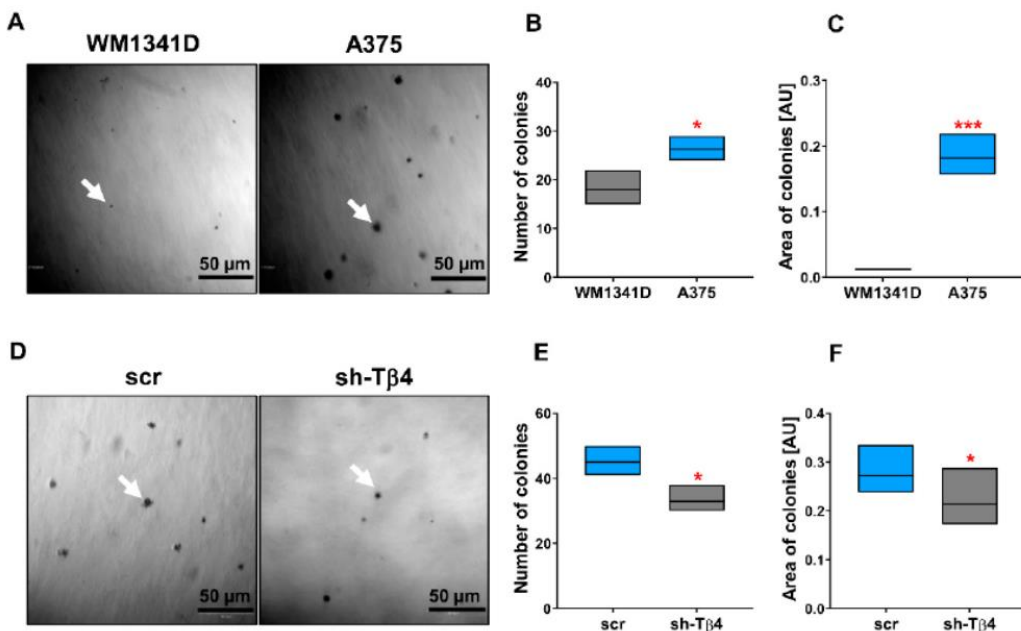


Figure 35: Different size and number of colonies formed in the soft agar colony formation assay for two melanoma cell lines expressing lower endogenous levels of T $\beta$ 4 and higher levels of this polypeptide. In the first case (WM1341D), the potential of these cells to initiate a colony is very low and also the size of the formed colonies is smaller compared to A375 cell line (A-C). An analogous response was observed for a subset of sh-T $\beta$ 4 clones in the same conditions (D-F).

### 3.2.2 Tumorigenic potential

To further validate the tumorigenic potential of melanoma cells with silenced TMSB4X expression, the *in vivo* tumour formation was checked using the chorioallantoic membrane (CAM) assay (Crespo, 2016). This essay consists of the formation of a window on the shell of fertilized chicken eggs at the seventh day of incubation.

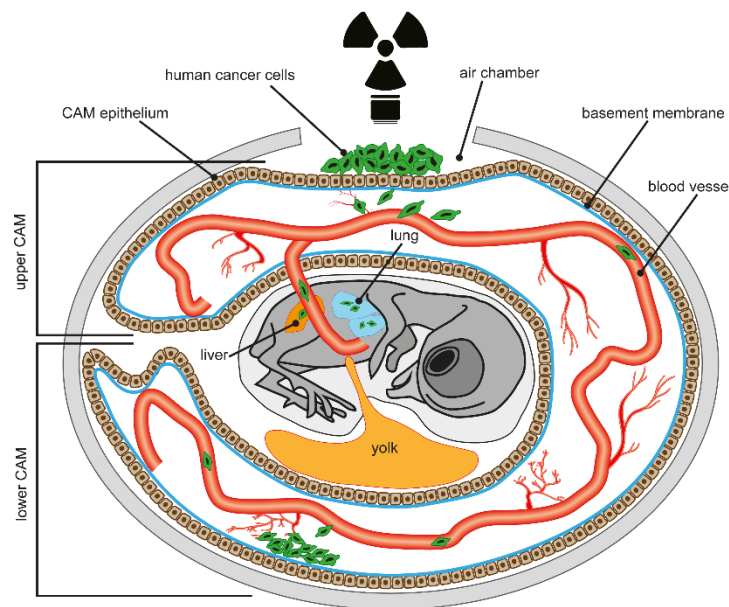


Figure 36: cells grafting on the Chorioallantoic membrane and the observation of tumour metastatic potential

This window allows to detach the CAM from the shell, exposing the allantoic vein. CAM is the highly vascularized membrane that surrounds the chicken embryo allowing the gaseous exchange with the external environment (see Figure 36).

Cancer (scr and sh-T $\beta$ 4 cells) are then grafted on this membrane and the window is sealed with tape. After 7 days the size and area of the developed tumours was checked.

The tumours formed by the cells with lowered T $\beta$ 4 levels were about 35% smaller than those observed in embryos after engraftment of scr cells (Figure 37 A, B). However, when the clones were analyzed separately, no statistically significant difference was noticed for any clone than control cells.

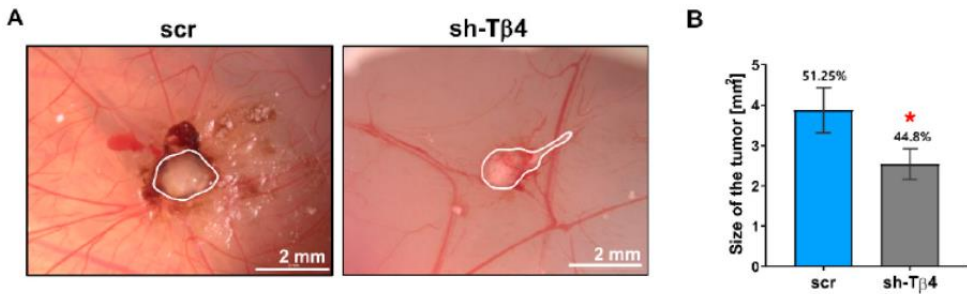


Figure 37: (A,B) CAM assay showing the difference in the size of the developed tumour in melanoma cell lines with lowered T $\beta$ 4 levels (sh- T $\beta$ 4) and control (scr) cells

### 3.2.3 Stemness related markers expression

Next, the transcriptional cell activity related to genes involved in stemness features (genes coding for Nanog, Nestin, c-Myc, and Sox2 proteins) was evaluated by qPCR (Hadjimichael, 2015). The results indicated statistically significant differences in mRNA level of transcripts only for Nestin (NES) (Figure 38 A–D). Here, increased NES expression was noted in the case of every sh-T $\beta$ 4 clone. Next, by Western blot analysis, the amount of the corresponding proteins (Nanog, Nestin, c-Myc, and Sox2) was evaluated. Total protein analysis was carried out to control the amount of loaded protein on the lanes. Similar c-Myc (that have two isoforms) and Sox2 levels for both sh-T $\beta$ 4 and scr cells (Figure 38 E, F) were observed. Surprisingly, compared to control cells, an increase in Nestin and Nanog levels was detected in the cells with silenced TMSB4X expression. For sh-T $\beta$ 4 clones, there was a 2.5-fold and 2-fold increase in the Nestin and Nanog level, respectively, relative to the control cells (Figure 38 F). Yet, only for a subset of the clones were statistically significant increases in the Nanog and Nestin level. The level of these proteins in A375 and WM1341D cells was also analyzed. In A375 cells characterized by better colony formation abilities, we observed a higher level of stemness marker proteins: Sox2, Nestin, and Nanog than in WM1341D cells. Lowering the T $\beta$ 4 level in melanoma cells diminished the tumour formation abilities in vivo only for a subset of clones. Similarly, changes in the expression level of transcription factors involved in

stemness were not observed for all clones. Despite this, Nestin was upregulated in almost all clones with the silenced expression of TMSB4X.

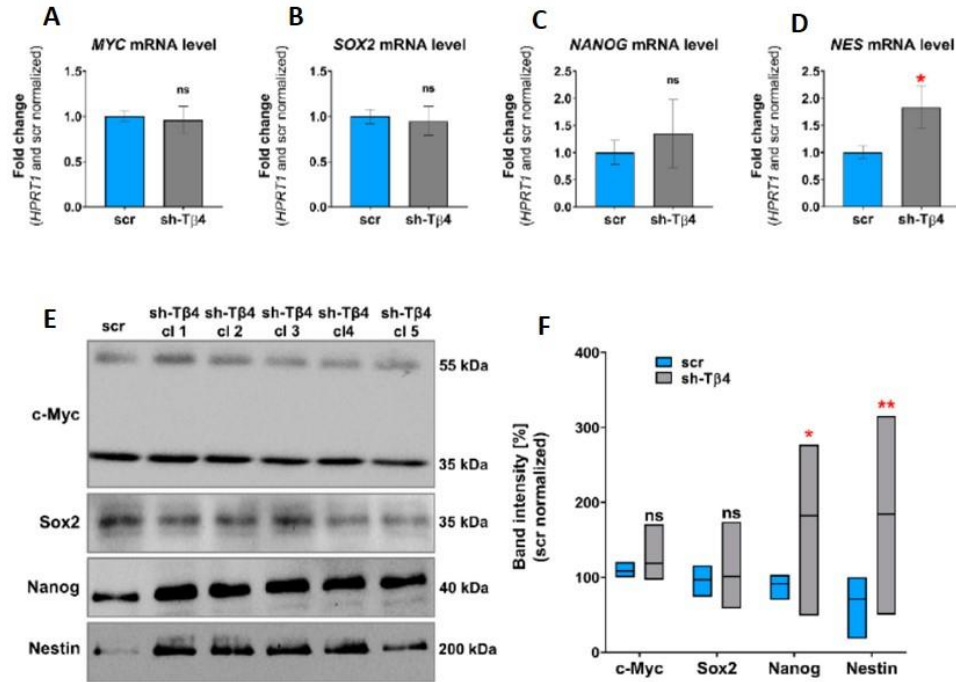


Figure 38: (A-D) mRNA transcripts levels of 4 genes coding for transcription factors involved in stemness features (c-Myc, Sox2, Nanog and Nestin) detected by qPCR. A significative increase in sh-T $\beta$ 4 clones is observed only in the case of Nestin transcript. (E-F) Western Blot (WB) results allow to find the differences in the amount of translated proteins involved in stemness features (c-Myc, Sox2, Nanog and Nestin) in the sh-T $\beta$ 4 clones compared to the control. Only for Nestin and Nanog a significative difference was noticed in the cells with lowered T $\beta$ 4 levels.

### 3.3 Cytoskeleton organization and biomechanical implications

#### 3.3.1 Actin cytoskeleton and intermediate filaments organization

The cellular localization of some components of the cytoskeleton was also examined. Filamentous (F-) and monomeric (G-) actin were selected because of the role of T $\beta$ 4 in the actin cytoskeleton organization and in particular in sequestering of monomeric actin (Goldstein, 2005). Nestin's subcellular localization was also investigated as it is the intermediate filament protein of neuronal stem cells and because of its observed increase in sh-T $\beta$ 4 cells. Additionally, vimentin, another IF protein identified as a nestin polymerization partner, was evaluated (Park, 2010).

F-actin and G-actin were detected by using fluorescently labeled phalloidin and deoxyribonuclease I (DNase), respectively. The intermediate filament proteins were detected with the help of appropriate antibodies. The confocal microphotographs for each cell were taken in three focal planes: cell contact area to the substratum (basal, green), a cross-section at the level of the cell nucleus (mid-height, red), and nucleus apical outer surface (apical, blue) (Figure 39). Finally, the photos taken at different focal planes were merged into a single image. Thanks to this approach, the 3D subcellular localization of the studied proteins was highlighted. More pronounced F-actin structures at the basal focal plane (green) in WM1341D cells, including stress fibers (pointed by arrows) than for A375 cells were observed. At the mid-height plane (red), more polymerized actin around the cell's nucleus, forming a ring for WM1341D cells than for A375 cells was observed. Finally, in the apical part of the WM1341D cells (blue), the actin network was more compact than in A375 cells (Figure 39 A). In both WM1341D and A375 cells, the G-actin was localized in the cytoplasm and the cell nucleus. However, in WM1341D cells, a higher signal for G-actin was observed in nucleoli (Figure 39 B, red arrows).

Nestin's visualization in WM1341D cells showed an interesting pattern. This intermediate filament protein was localized predominately in the nuclear area, forming a structure entwining the cell nucleus (Figure 39 C). At the mid-height plane (red), Nestin filaments were assembled in the ring-shaped form (Figure 39 C, yellow arrows). Nestin filaments were observed below and above the nucleus in the other two focal planes. On the contrary, in A375 cells, Nestin was primarily localized in the basal area's cell body. The observed Vimentin staining pattern was similar to that described previously for Nestin for both cell lines (Figure 39 D).

Next, the subcellular location of F-actin, G-actin, Nestin, and Vimentin in scr and sh- T $\beta$ 4 cells was also investigated. In the case of sh- T $\beta$ 4 cells, more pronounced F-actin structures at the basal focal plane (green) were noticed when compared to scr cells (Figure 40 A). Similarly to WM1341D, more polymerized actin around the cell's nucleus for sh- T $\beta$ 4 than for control cells at the mid-height plane

was highlighted. At the apical plane, less compact F-actin was observed for scr cells than for sh- T $\beta$ 4 cells.

In the cells with downregulated TMSB4X expression, G-actin's signal was weaker than in control cells and localized mainly in the cell nucleus (Figure 40 B).

In sh- T $\beta$ 4 cells, more Nestin filaments were localized around the cell nucleus at the mid-height and apical planes than in control cells (Figure 40 C). We observed a similar Nestin staining pattern for Vimentin in tested cells (Figure 40 D). In summary, the actin cytoskeleton, Nestin, and Vimentin filaments were organized significantly differently in melanoma cells with low T $\beta$ 4 levels than the cells with high TMSB4X expression. Less prominent F-actin structures were observed for latter cells, accompanied by Nestin and Vimentin being more dispersed at the basal focal plane.

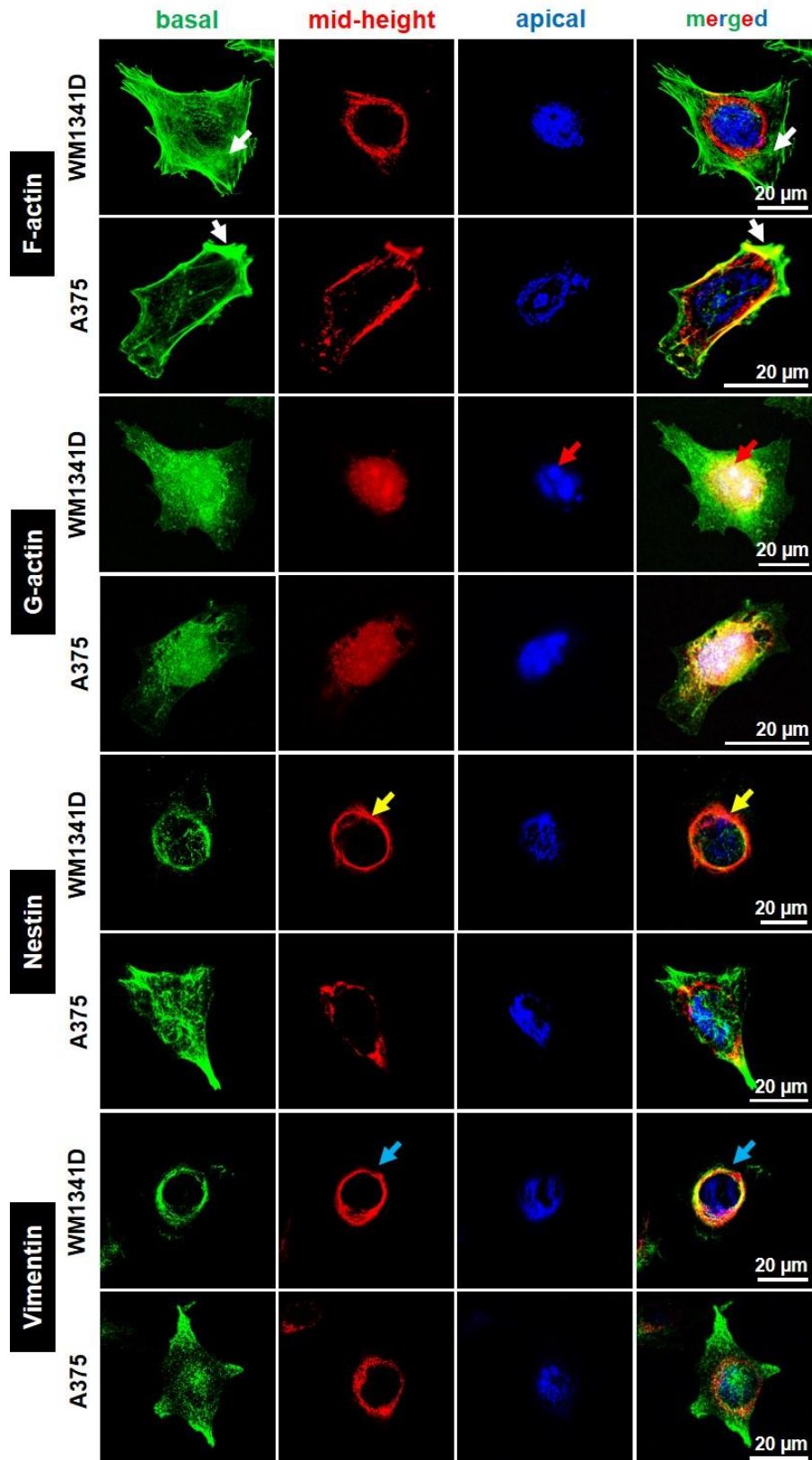


Figure 39: (A-D) immunostaining of F-actin, G-actin, Nestin and Vimentin in cells with endogenous higher levels (A375) and lower levels (WM1341D) of T $\beta$ 4, three focal planes are depicted: the basal focal plane (in green), the mid-height (in red) and the apical (in blu) and finally the merging of these images is shown. (A) White arrows indicate stress fibers, (B) red arrow points at the nucleoli, (C, D) yellow and blu arrows indicate a ring-shaped structure nestin and vimentin around the nucleus

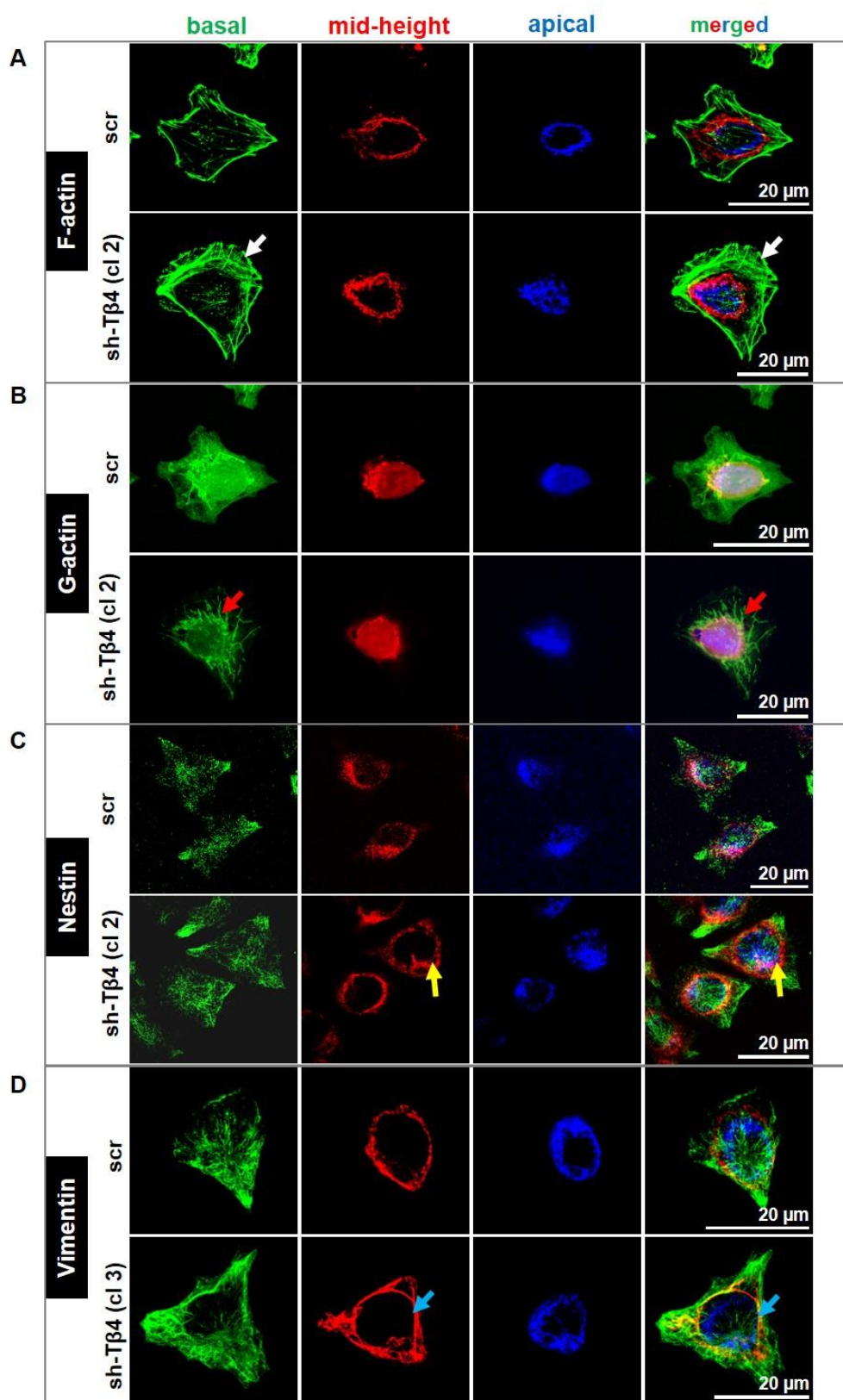


Figure 40: (A-D): immunostaining of F-actin, G-actin, Nestin and Vimentin in cells with silenced expression of TMSB4X, three focal planes are depicted: the basal focal plane (in green), the mid-height (in red) and the apical (in blue) and finally the merging of these images is shown. (A) White arrows indicate stress fibers, (B) red arrow points at the nucleus, (C, D) yellow and blu arrows indicate a ring-shaped structure of nestin and vimentin around the nucleus

### 3.3.2 Cell mechanical properties

Finally, by AFM-indentation, the mechanical properties of the tested melanoma cells were evaluated. A NanoWizard II AFM (JPK instruments) mounted on top of an Axiovert 200 inverted microscope was used. Measurements were performed at the centre of the cells, over the nuclear region in order to avoid the contribution of the underlying substrate, with pyramidal cantilevers (OMCLTR 400PSA HW, Olympus) with nominal spring constant 0.02N/m. The cantilevers were calibrated by the thermal noise method before each experiment and force-distance curves were collected with a force loading of 0.4 Nn and a rate of 2.5 $\mu$ m/s. All experiments were performed at 37 °C using a temperature controlled BioCell chamber. Five curves were acquired for every cell, and in every experiment, a minimum of 30 cells was analyzed. Obtained force-distance curves were next fitted through the Sneddon model (described in detail in Ch. 2, section 2.5.1) to calculate for each cell Young's modulus (E) defining cell stiffness. Force-distance curves were analyzed with JPK data processing software.

WM1341D cells were characterized by statistically significative higher values of Young's modulus, which means that these cells were stiffer than A375 cells (Figure 41 A). The average value of Young's modulus for WM1341D cells was 5.6 kPa, almost 2 times higher than for A375 cells, for which the average value was 2.8 kPa. The stiffness analysis also showed that the stiffness was increased for the cells with decreased TMSB4X expression (Figure 41 B). The average value of

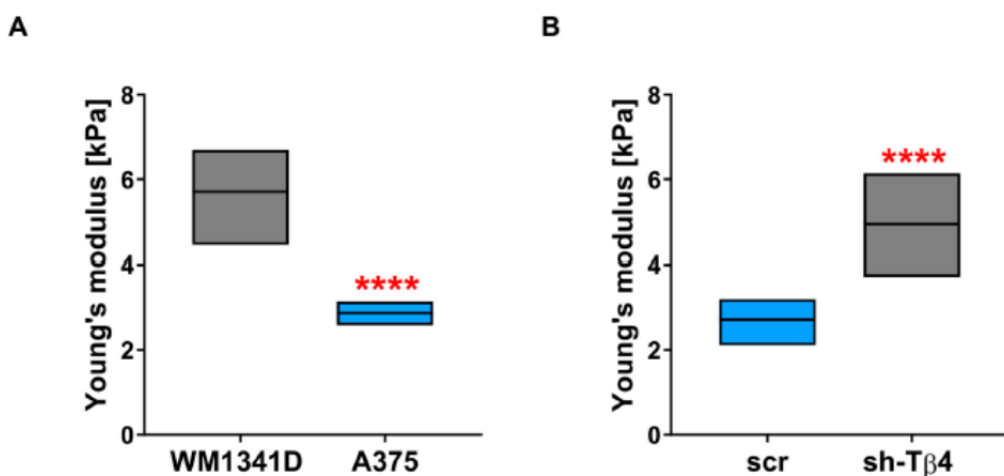


Figure 41: Change in the cell stiffness between the tested cell groups. Cells with lowered levels of T $\beta$ 4 (WM1341D and sh-T $\beta$ 4 clones) are characterized by an increase of the stiffness compared to scr and A375

Young's modulus for sh-T $\beta$ 4 cells was around 5 kPa and was almost twice that of the control cells, for which the average value was ~2.7 kPa. Our results suggest that the silencing of TMSB4X expression in melanoma cells caused changes in their biomechanical properties. This effect was observed for every sh-T $\beta$ 4 clone.

### 3.3.3 Cell height and morphology

The height and morphology of the different cell lines was evaluated by AFM imaging. Cells were fixed with 4% paraformaldehyde and dehydrated with gradients of ethanol. AFM imaging was performed with a MFP 3D-BIO AFM (Asylum Research) and using the same pyramidal tipped cantilevers used for SCFS. Imaging was done in contact mode in the air, with a scan rate of 1Hz, a scanning area of 90  $\mu$ m. with 1024 scan points, a set point of 1 V. The integral and proportional gains were set to 10 and 0, respectively. Gwyddion software was used to analyze the obtained images.

In Figure 42, the error signal and the height channels are shown. From the first, 2D imaging with highly contrasted lateral resolution could be detected, from the second one the 3D topographical information could be obtained. Looking at the error signal (Figure 42 A), WM1341D and sh-T $\beta$ 4 cells were similar: these cells were more spread on the substrate than A375 and scr cells. Moreover, WM1341D and sh-T $\beta$ 4 cells were characterized by broader membrane extensions in which we observed more prominent filamentous structures (Figure 42 A, pointed with arrows) compared to A375 and scr cells, respectively.

In WM1341D and sh-T $\beta$ 4 cells, the nucleus was distinctly separated from the rest of the cell body with clearly visible nucleoli in contrast to A375 and scr cells. The maximum heights of A375 and scr cells were 1.5  $\mu$ m and 1.6  $\mu$ m, respectively. While in the case of WM1341D and sh-T $\beta$ 4 clone, they were 1.02  $\mu$ m and 1.11  $\mu$ m high, respectively (Figure 42 B, C). This height difference was statistically significative for both the two sample groups: A375 and scr cells were much higher than WM1341D and sh-T $\beta$ 4 cells (Figure 42 D). In summary, melanoma cells with low T $\beta$ 4 levels were

characterized by a more spread morphology and lesser height of the cell body than the cells with a high level of this polypeptide. This phenomenon was observed for all sh-T $\beta$ 4 clones.

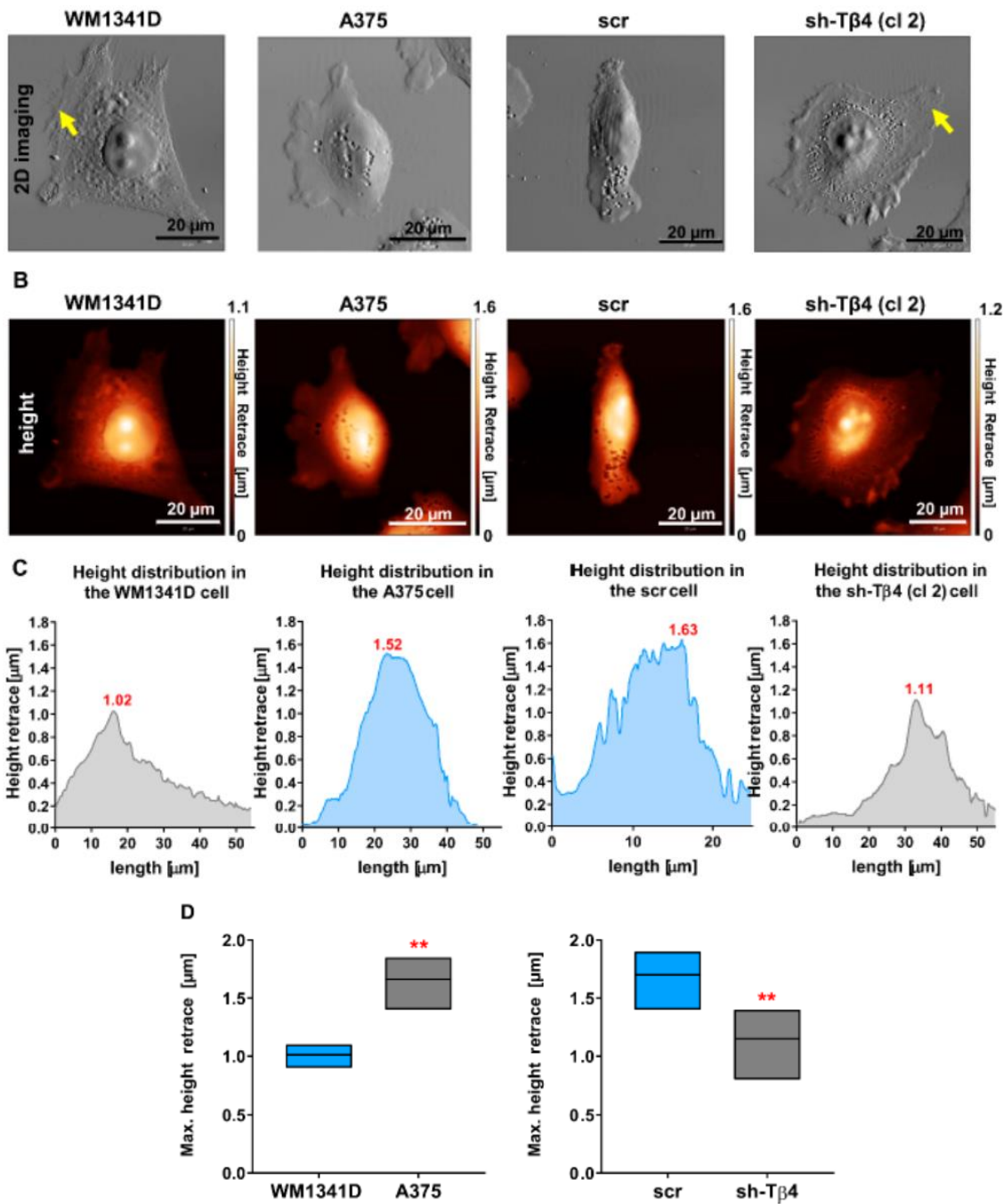


Figure 42: (A) error signal channels showing high 2D lateral resolution for the analyzed cell lines, (B) topographical information from the height channel of the same cells, (C, D) height distributions of the cell lines showing a statistically significative difference in the higher cell height of A375 and scr cells compared to the one with lowered levels of T $\beta$ 4

### **3.4 Conclusions**

Cancer stem cells are a subpopulation in the tumor often associated to tumor recurrence and progression. Standard anti-cancer treatments are ineffective at eradicating these cells whose percentage is normally very low (Scatena, 2012).

As it was previously shown, T $\beta$ 4 is essential for the maintenance of glioblastoma stemness, so the evaluation of the role of T $\beta$ 4 in melanoma tumorigenicity and clonogenicity (factors that are manifestations of stemness features) was carried out. The results presented here indicate that the cells with a lowered T $\beta$ 4 level initiated a lower number of CAM model tumors than control cells. Moreover, they were smaller. The clonogenic potential was as well diminished in those cells.

In order to assess the stemness level of the studied cell lines, the analysis of the levels of three transcription factors, known marker involved in the maintaining of cell stemness, was performed. Nevertheless, it was not possible to establish a unequivocal correlation between tumorigenic potential and chosen stemness-related transcription factors' expression level in the tested melanoma cells as results change according to different clones.

Constant crosstalk between the cytoskeleton's three main components (actin microfilaments, microtubules, and intermediate filaments, IFs) is essential for proper cell functioning. For this reason the distribution of two IFs was evaluated: Nestin and Vimentin.

When stress fibers were disassembled in the cells, Vimentin's perinuclear localization disappeared, and instead, Vimentin was spread across the cell body. A similar effect was shown also for Nestin and is not surprising in view of the constant interaction of these two proteins.

Contrasting results regarding the relation between Nestin levels of metastatic breast cancer cells and the cell mechanical properties were previously found (Yamagishi, 2019). Here the increased level of Nestin in the A375 clones with lower levels of T $\beta$ 4 together with an increase in the cell stiffness of the same cells, could be explained by the location of this IF protein in the perinuclear cap. On the contrary, A375 cells with increased T $\beta$ 4 levels were characterized by a softer mechanical phenotype,

and a Nestin localization rather spread in the cytoplasm in a less organized disposition. So it is here proposed that Nestin levels in the cells affects the mechanical properties according to the different location in the cell body. Apparently, T $\beta$ 4, by affecting actin cytoskeleton, also induced changes in Nestin and Vimentin locations, in that way influencing cell morphology and biomechanical properties (Figure 44).

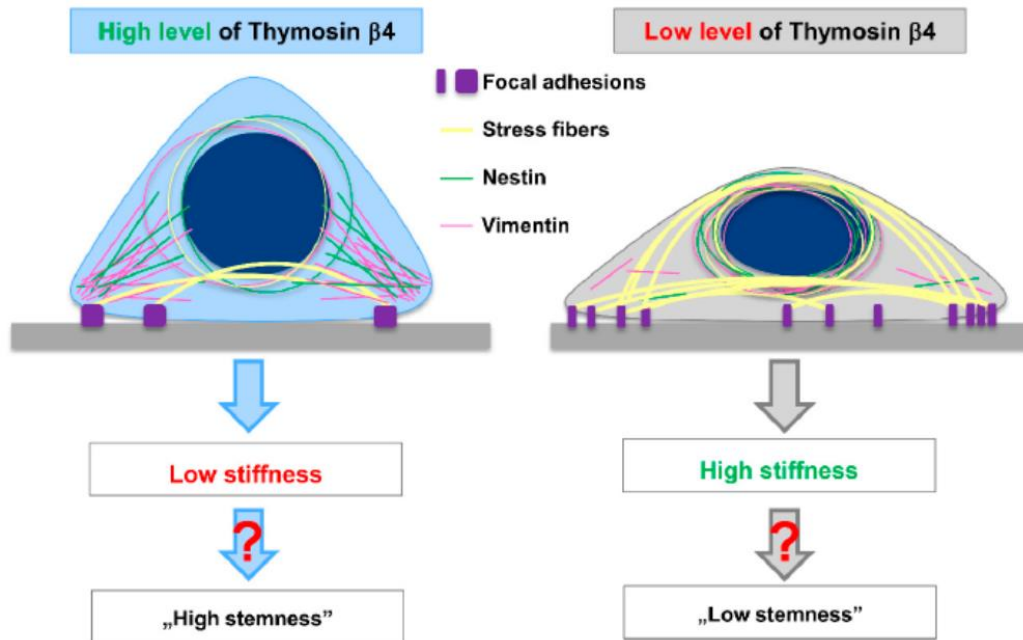


Figure 44: Postulated disposition of cytoskeleton main components according to the different expression of TMSB4X. Cells with higher T $\beta$ 4 levels are characterized by a softer mechanical phenotype, the absence of actin stress fibers and less localized IFs around the perinuclear capping. On the contrary, cells with low levels of T $\beta$ 4 are characterized by an increased presence of stress fibers and IFs proteins localized in the perinuclear area

The increased stiffness in the cells in which TMSB4X was silenced, is also explained by an increase in actin stress fibers formation.

The role that T $\beta$ 4 plays in the organization of focal adhesions, has been recently shown: when the levels of this polypeptide are decreased, the morphology and number of FAs change providing a stronger interaction with the substrate. The change in adhesion abilities of sh-T $\beta$ 4 cells well matches with the modifications observed in this study of cell morphology that result in diminished body height and increased spreading on the substrate.

It has been shown that the mechanical properties of materials on which cells grow strongly influence their fate and functions (Fusco, 2015). It is then plausible that changes in focal adhesion organization and, thus, adhesion upon TMSB4X expression silencing could reprogram cell's fate. However, a correlation between biomechanical properties and stemness was observed solely for selected clones with silenced expression of TMSB4X. Moreover, not all clones expressed statistically significant changes compared to the control cells while analyzing the results from clonogenicity and tumorigenicity.

However, for the distribution of the cytoskeletal proteins studied here and the cells' biomechanical properties, we obtained consistent results for all tested clones with lowered TMSB4X expression. This intriguing observation suggests that even though A375 cells stemness is probably linked with alterations in the biomechanical properties, this is not a direct link and apparently there is an additional factor linking them, which is not uniformly present in the whole population of A375 cells.



# Chapter 4

## 4.1 Introduction

Microvessels regulate the coronary blood flow by promoting the exchange of oxygen and metabolites between blood and tissues. In case of coronary microcirculation diseases (CMD) the impairment in this metabolic traffic leads to ischemia. On the contrary, peri-infarct angiogenesis by supplying oxygen and nutrients prevents cardiomyocytes hibernation.

The coronary microcirculation diseases (CMD) are interconnected with macrocirculation ones and often coexist with coronary artery atherosclerosis (Taqueti, 2018).

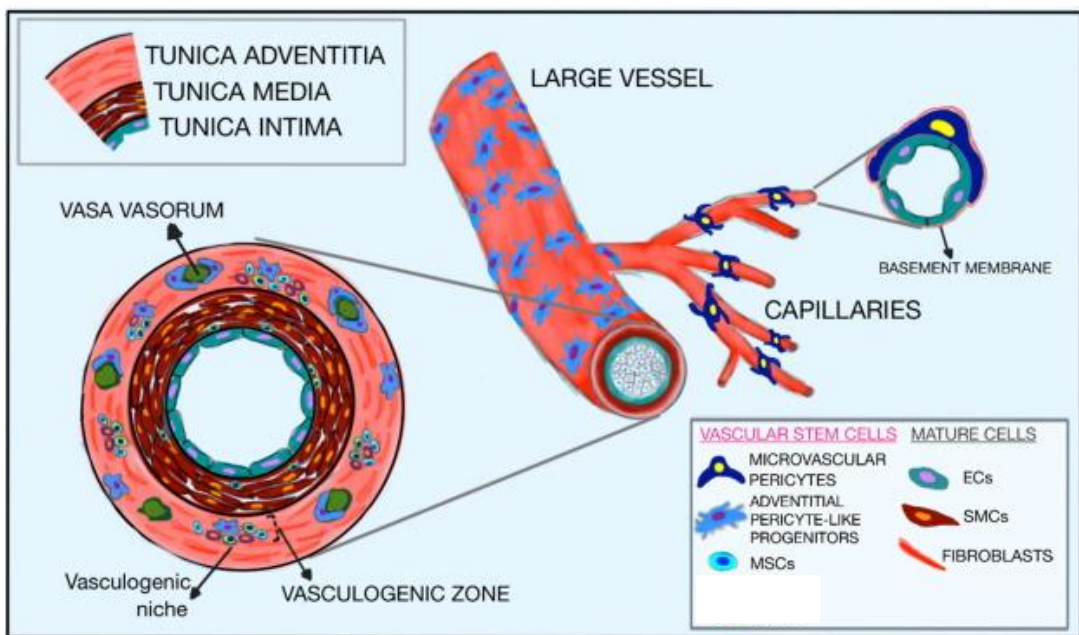


Figure 45: cross-section of a larger vessel and smaller capillaries highlighting the layered structure composed by a luminal layer of endothelial cells (ECs) surrounded by the basement membrane and, in the case of large vessel, one layer of smooth muscle cells (SMCs) and one of connective tissue. Cardiac pericytes lie in close contact with ECs

Pericytes (Pc) are a heterogeneous population of cells embedded within the basal lamina of microvessels in close contact with endothelial cells (as depicted in Figure 45), they exert a regulatory function during microcirculation: regulate immune cell trafficking, modulate fibrosis, angiogenesis

and the stabilization of newly formed vessels, during infarct healing (O'Farrell, 2014). The possible role exerted by this cell population in heart failure leads to microvascular dysfunctions in case of pericytes damage. On the other side, transplantation of pericytes promotes cardiac protection against ischemia (Chintalgattu, 2013) (Chen C. W., 2013) (Avolio, 2015).

Few antigens specifically allow to distinguish pericytes from other cell types: PDGFR $\beta$ , CD146 and Tbx18 are shared between many pericytes, then other specific antigens are typical of only arterial or capillary Pc. Other novel Pc markers recently identified are CD93 and Caveolin-1 (CAV-1) (Hsu, 2019) (Guimaraes-Camboa, 2017).

Recently, the involvement of ROCK (Rho associated kinase) signaling in modulating Pc contractility has been demonstrated, suggesting the primary role of mechanotransduction in the modulation of the Pc function (Durham, 2014).

Yes-associated proteins (YAP) and transcriptional activators with PDZ binding motif (TAZ) are two co-transcriptional factors that are involved in the activation of genes related to cell proliferation and differentiation in response to mechanical cues (like substrate stiffness, stress/strain stimuli and cell contact inhibition of proliferation). The most important gene family are Transcriptional Enhanced Associate Domain (TEAD). YAP/TAZ are in turn controlled by Hippo pathway (which involves MST and LATS kinases) and by ROCK signaling (Pesce, 2017) (Piccolo S. D., 2014). Recent data have shown that also CAV-1 and MRTF (Myocardin related Trascription Factors) play a role in mechanosensing, the first by regulating the activity Rho GTPase and promoting actin polymerization, the second by co-regulating the expression of several cytoskeletal genes (Moreno-Vincente, 2019) (Foster, 2017).

The mechanotransduction properties of pericytes residing in ischemic failing hearts compared to the one of healthy heart donors are investigated. The results allow to shed light on the mechanisms involved in the observed change in biomechanical properties, open important perspectives in the field of heart tissue regeneration.

## 4.2 Cardiac pericytes, cell lines characterization

### 4.2.1 Cardiac pericytes rarefaction in chronic ischemia

The distribution of Pc was evaluated in left ventricular biopsies of patients affected by end stage heart failure secondary to chronic ischemia and control hearts.

PDGFR expressing cells were observed both in the smooth muscle cell layer of arterioles and associated with smaller vessels (Figure 46 A, B). Capillary pericytes were distinguished from the arteriolar ones according to lower amount of smooth muscle actin. CAV-1 and CD93 were also used as Pc markers. But the presence of CAV-1 was highlighted also in endothelial cells (Figure 46 E, F, M).

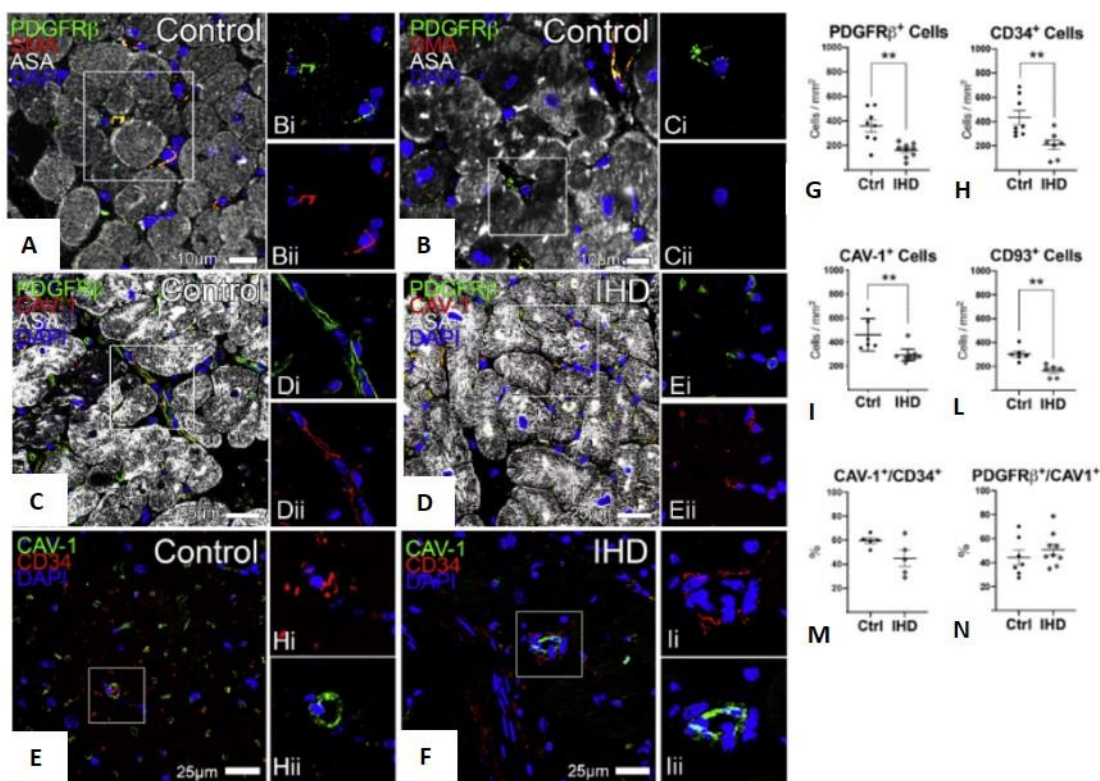


Figure 46: Pc located in arterioles (A) are distinguished from that of smaller capillaries (B) by the presence of smooth muscle actin (SMA), a characteristic feature of arterioles, overlapped to PDGFR $\beta$  Pc marker. CAV-1 is expressed in both control (C, E) and ischemic human heart (D, F) both in endothelial cells (E, F) characterized by the presence of CD34 and pericytes (C, D) the higher level of these markers in control compared to ischemic hearts (G-L) shows the occurrence the microvascular rarefaction. CAV-1 is expressed in both endothelial cells and pericytes (M, N)

Pc density was significantly reduced in failing hearts. The microvascular rarefaction involved also the endothelial cells (in that case, the recognition marker used was CD34).

Pericytes were expanded in vitro and Pc lines where then characterized by immunolabeling for the Pc markers PDGFR $\beta$ , Tbx18 and NG2 (Figure 47). The vast majority of cultured cells (>80%) were characterized by the presence of these markers. The low contamination levels with fibroblast was also determined by the low presence of TCF21 (a fibroblast marker).

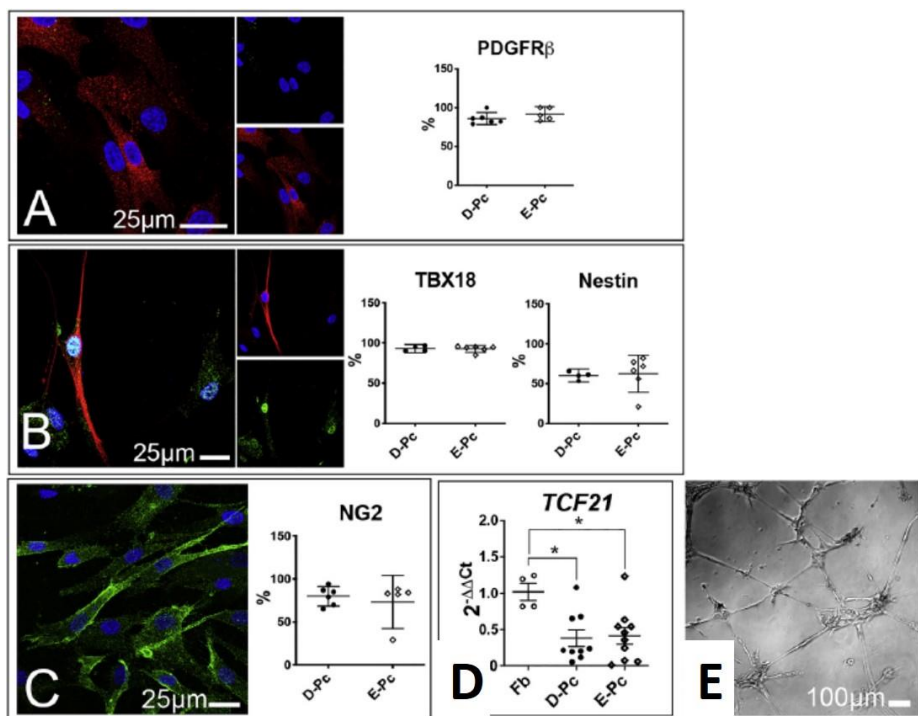


Figure 47: high levels of PDGFR $\beta$ , TBX18, Nestin, NG2 characterize the Pc cell lines (A, B, C), the low levels of TCF21 compared to fibroblasts highlight the low contamination levels by these cells (D), finally Pc formation of vascular networks (E) D-Pc derives from healthy hearts and E-Pc from failing ischemic hearts

#### 4.2.2 Pericytes activity of angiogenesis induction is impaired in failing hearts

The ability of endothelial cells to form vascular networks in vitro was evaluated when culture media were conditioned by D and E-Pc. Cells were culture on Matrigel, that mimics the ECM (extracellular matrix). An increase efficiency of D-Pc compared to E-Pc in promoting this effect was detected: vascular tubes formed by endothelial cells cultured in the presence of healthy pericytes were

significantly longer compared to the control (any vascular effect was observed) and the cells treated with pericytes from failing ischemic hearts (Figure 48).

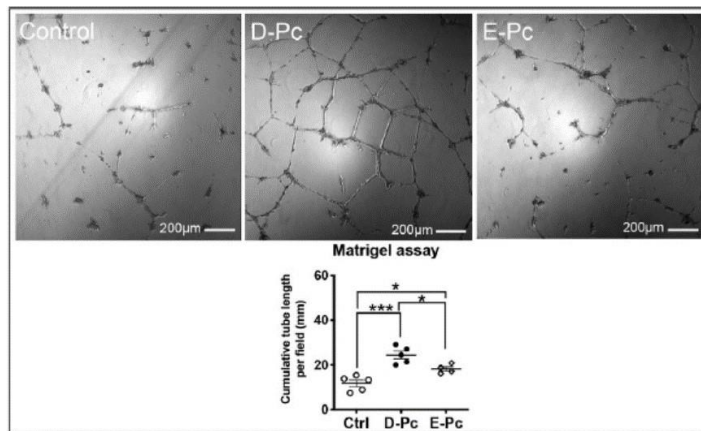


Figure 48: Different vascular network promoting ability of D and E-Pc on endothelial cells cultured in vitro

## 4.3 Pericytes different responses to external stimuli

### 4.3.1 Hydrogel preparation with different stiffnesses

Coverslips (24mm) are first washed with ethanol and left drying on a glass sheet. To make the polyacrylamide adhere to the coverslip, a solution of metacrylate and ethanol 1:1 is prepared and a drop of 15-20 ul is put on the coverslips that are then washed with ethanol and milliQ water. The coverslips are then dried and the polyacrylamide solutions are prepared, according to the ratio between the acrylamide and the bis-acrylamide (the cross-linker reagent), gels with different stiffness can be obtained, as described in the table 1.

ELASTIC MODULE	Acrylamide (40% solution)	Bis-Acrylamide (4% w/v)	dh2o
1 kpa	0,75 ml	0,25 ml	9 ml
16 kpa	2,5 ml	0,37 ml	7,13 ml
231 kpa	5 ml	3,75 ml	1,25 ml

Table 1: the different amount of Acrylamide and Bis-Acrylamide needed for the preparation of gels with different stiffness

Then the glass sheet is cleaned with ethanol followed by milliQ water and dried; A paper cloth is wet with methylsilane and the glass sheet is cleaned. This step allows then the coverslips to detach from the glass.

A source of free radicals and a stabilizer, such as APS (ammonium persulfate) and TEMED (Tetramethylethylenediamine) are added to the solution to induce the cross-linking and, working quickly from this point, 50ul drops of the acrylamide solution for each coverslip are placed on the glass slide and the coverslips are put over with the functionalized side to the drop. When the hydrogel is polymerized, the coverslips are detached with the help of a blade and moved into the petri dish filled with milliQ and stored at 4°C overnight before use.

#### **4.3.2 Hydrogel coating with fibronectin**

Sulfo-sanpah, sulfosuccinimidyl 6-(4'-azido-2'-nitrophenylamino)hexanoate, is used as a protein cross-linker agent. After the washing with sterile PBS, the coverslips are moved into a sterile culture plate. A sulfo-sanpah solution with PBS is prepared, the coverslips are covered and left under UV lamp for 20 minutes. After that, the sulfo-sanpah is removed and three PBS washing are performed. The fibronectin solution (1mg/ml or 25mg/ml) is prepared, put over the coverslip and left for overnight incubation at 4°C. After removal of fibronectin and PBS washing, the cells are seeded.

#### **4.3.3 Cell morphological change in response to external stimuli**

Gene expression levels were analysed by RNA sequencing and two main clusters were identified, distinguishing D from E-Pc (pericytes deriving from healthy hearts and failing ischemic hearts, respectively). Differentially expressed genes were 627, by functional enrichment analysis it was possible to identify perturbations in genes involved in vascular development, chemotaxis, regulation of actin-filament based processes and cell response to extracellular stimuli.

For this reason, the different responsiveness to external mechanical stimuli of D and E-pericytes was evaluated by changing two parameters: the substrate fibronectin coating and the substrate stiffness. Pc obtained from normal hearts spread and flattened more than those obtained from pathologic hearts. Moreover, while D-Pc responded to the increased fibronectin concentration by decreasing their circularity and solidity, E-Pc did not (Figure 49).

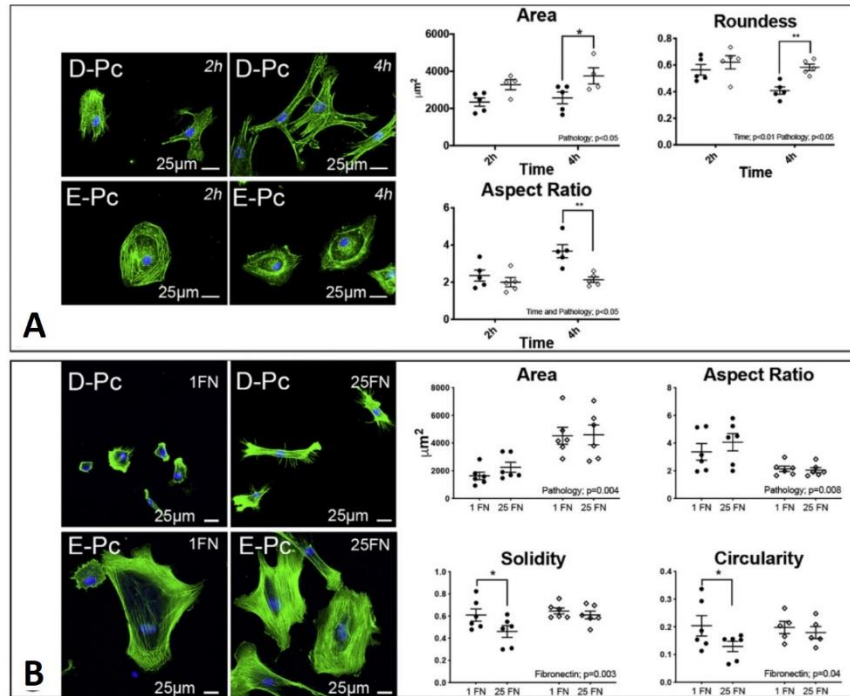


Figure 49: (A) D and E-Pc adhesion after 4h from seeding, the difference in cell spreading and polarization is highlighted by the statistically significative change in Roundness and Aspect Ratio indexes, (B) significative decrease in solidity and circularity indexes only for cells healthy Pc according to the increased fibronectin concentrations

Next, the morphological changes in response to different substrate stiffness were evaluated by seeding the cells on three different supports: two polyacrylamide gels having a Young modulus of 16kPa and 231 kPa and a glass coverslip with stiffness in the order of GPa. As showed in Figure 50, as substrate stiffness increased, D-Pc morphology was significantly affected. The response was an increase of their polarization (aspect ratio) and a decrease in their circular shape (solidity). Conversely, the main response of E-Pc was cell hypertrophy (increase in size).

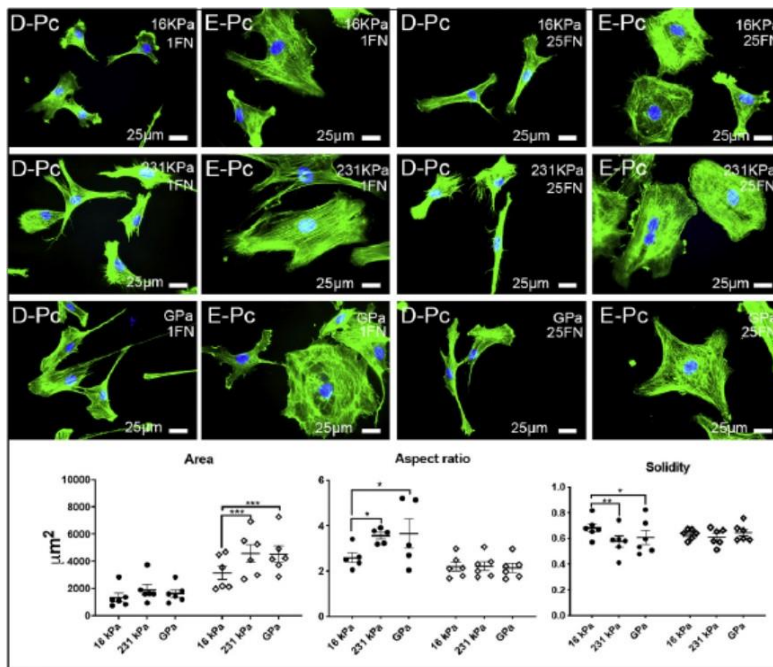


Figure 50: Different responses of D and E-Pc to substrate stiffness. As highlighted by the increase in the cell area of E-Pc in stiffer substrates, the main response of this cell line was hypertrophy, while E-Pc responded by increasing the spreading and polarization and decreasing the solidity

#### 4.3.4 Cell mechanical properties change in response to substrate stiffness

The mechanical properties of D and E-Pc seeded on the same substrate mentioned before (16kPa, 231 kPa and glass) were tested by AFM-force spectroscopy. Triangular cantilevers with a glass bead ( $d=4.5\mu\text{m}$ ) glued on the tip of nominal spring constant 0.3 N/m were previously calibrated and used for the purpose. Cantilever were prepared by mounting silica microspheres of 4.5 mm nominal diameter to silicon AFM triangular tipless cantilevers (Nanoworld with Cr/Au back-side coating) of nominal spring constant  $k = 0.32$  N/m by using UV sensitive glue. Silica beads were picked under microscopy control, cured for 15 minutes with a UV lamp and left stabilizing overnight.

Measurements were performed at the centre of the cells with a force setpoint of 0.5 nN and  $5\mu\text{m}/\text{s}$  speed. For each sample conditions at least 30 cells were measured. The force-distance curves (15 curves/cell) were fitted through the Hertz model (described in detail in Chapter 2, section 2.5.1) and the Young's modulus (E) was calculated, by an Igor procedure. The distribution of the values for the different conditions is shown in Figure 51. As depicted, D-Pc increased in a statistically significative

way their stiffness when seeded on glass support, while E-Pc did not respond to the increased substrate Young's modulus.

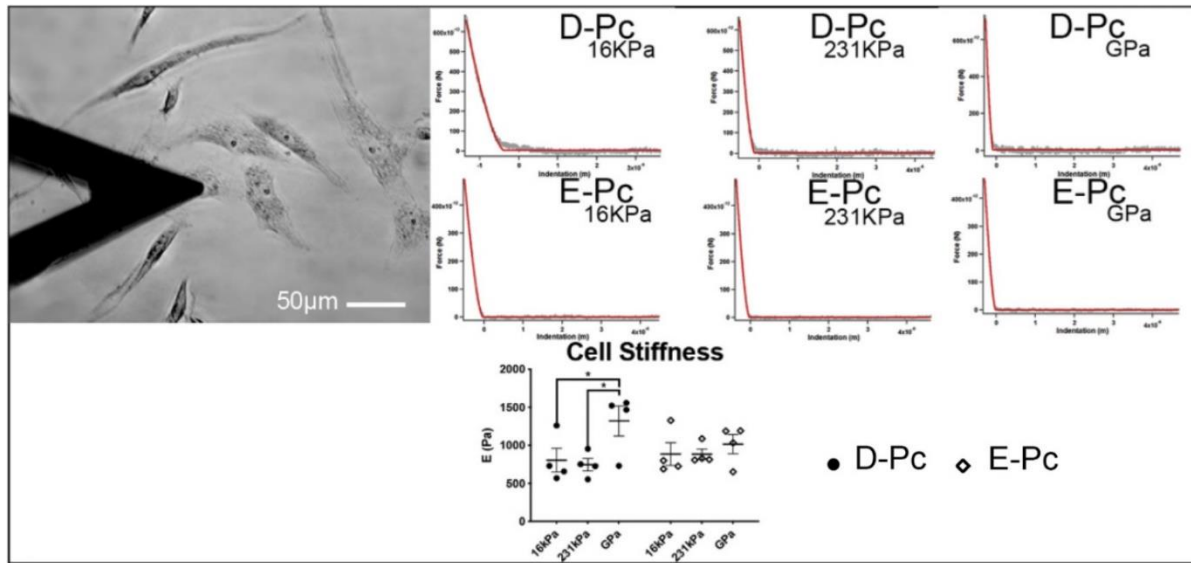


Figure 51: AFM-nanoindentation measurements on D and E-Pc grown on different stiffness substrates, 6 force-distance curves are shown. The distribution of values (shown by dotplots) for at least 30 cells for different conditions is shown. There is a consistent increase in E (Young modulus) of D-Pc on a stiffer substrate, while E-Pc did not respond the mechanical stimulus

#### 4.3.5 Mechanosensing alteration of pericytes isolated from failing hearts

The alteration in the mechanosensing machinery that could be responsible for the observed functional differences were investigated.

First, the density of focal adhesions (FAs) in D and E-Pc grown on glass substrates was evaluated by immunofluorescence, looking at presence of Paxillin, a component of FAs. The cellular area fraction covered by this factor was significantly lower in E-Pc (Figure 52, A). Consistently, the levels of FAK phosphorylated were significantly lower in these cells and even if the total levels of p130 CAS were higher in E-Pc, the fraction phosphorylated of this molecule was lower (Figure 52, B i-ii).

Since CAV-1 has been shown to regulate the response to substrate stiffness, its expression was also evaluated and resulting in a downregulation in E-Pc (Figure 52, C). Given the interaction of this factor with Rho-GTP, the levels of this factor were also evaluated, but although a trend toward a reduction in E-Pc was observed, it did not reach significance (Figure 52, D).

Finally, the spatial distribution and relative abundance of both F-actin and NMII (non-muscle myosin) was analyzed. Consistently with mechanical data, both the number of stress fibers per unit of cell area and average stress fiber thickness were negatively influenced by cardiac pathology (Figure 52, E, F).

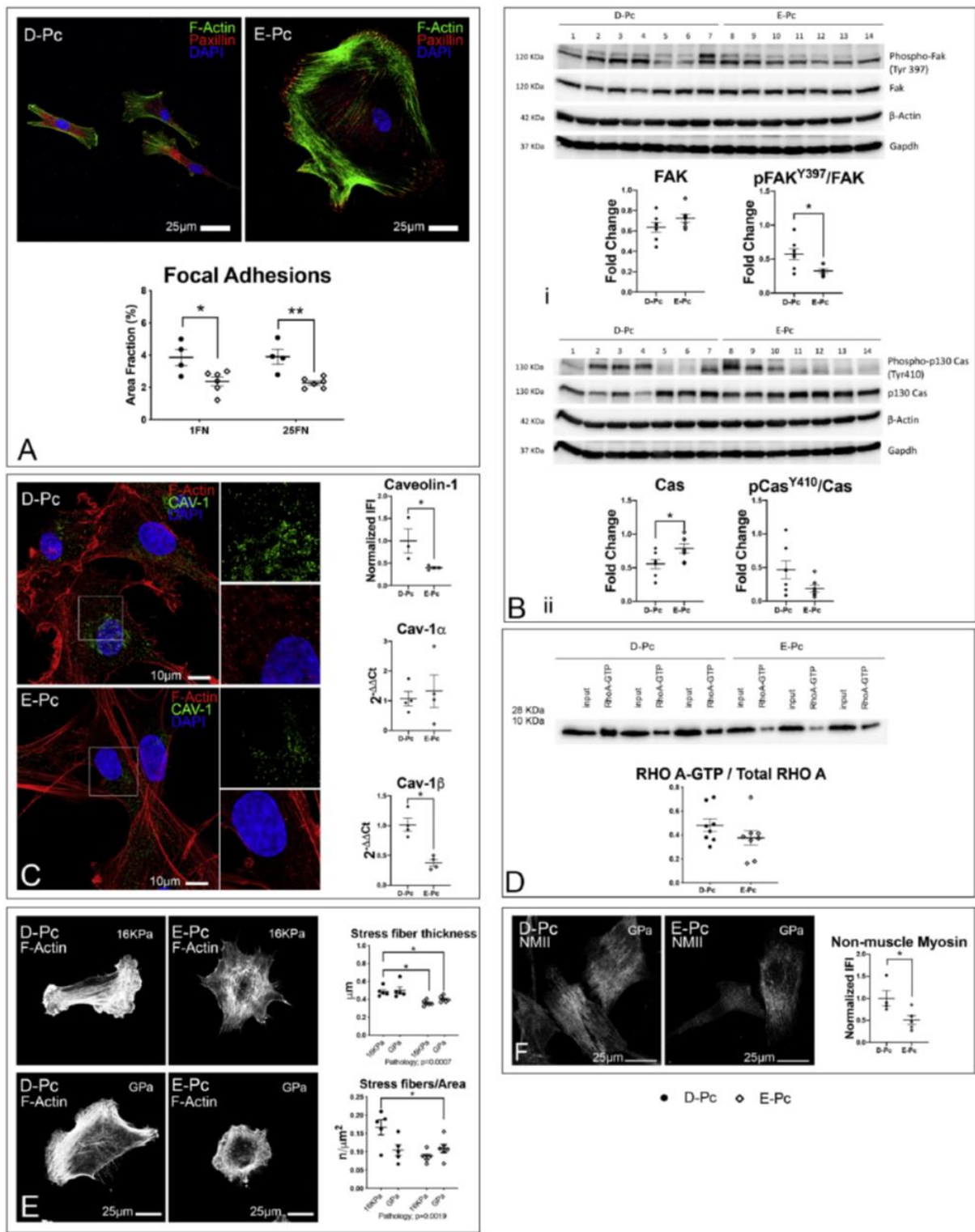


Figure 52: Alterations in cytoskeleton components and mechanosensing pathways are depicted (A) lowering in the number of focal adhesions (FAs) in E-Pc compared to D-Pc expressed by the decreasing of Paxillin per cell area, (B) concentration of FAK phosphorylated ( $pFAK^{Y397}$ ) is significantly lower in E-Pc, also a decrease even though not significative, in  $pCas^{Y410}$  could be detected in E-Pc, (C) lower levels of CAV-1 are detected in E-Pc, in particular the  $\beta$  isoform, (D) there is a decrease in Rho-GTP concentration of E-Pc, (E) there is an higher number of stress fibers/area and an higher stress fiber thickness in D-Pc grown on both 16kPa and glass supports compared to E-Pc, (F) also the amount of NMII (non-muscle myosin) is higher in D-Pc than E-Pc when grown on glass

#### **4.3.6 Mechanotransduction properties are altered in pathology-related pericytes**

To further investigate the molecular pathways associated to the change observed in the mechanosensitive cell components and the related modification of the mechanical phenotype on hard substrates, the cell localization of co-transcriptional activators, like YAP/TAZ, was investigated. The nucleus/cytoplasmic (N/cyt) shuttling of YAP in response to substrate stiffness was analyzed. By immunofluorescence it was possible to locate this factor and to assess the N/cyt ratio. The same was done for another co-transcriptional activator: MRTF-A. The results confirm what was expected from the mechanical data: the N/cyt ratio of these factors was very high in D-Pc grown on hard substrates compared to softer ones. Moreover, only in this cell line a similar effect was observed, while in E-Pc an increase of YAP and MRTF-A according to the increase in substrate stiffness did not occur (Figure 53 A). Then, the effect of substrate coating on the cellular localization of these factors was also evaluated. As concerns YAP N/cyt ratio, while D-Pc increased the nuclear localization of YAP as a function of fibronectin concentration, E-Pc did not. Conversely, MRTF-A modulation was not affected by the concentration of fibronectin. In order to explain which was the pathway involved in the observed YAP nuclear translocation, the amount of other factors involved in the Hippo pathway was investigated too (Figure 53, B, C). The level of phosphorylation of two regulatory serines and the status of the upstream regulator LATS-1 were not affected. On the contrary, levels of β-TRCP (an ubiquitin ligase involved in cytoplasmic YAP degradation) were significantly higher in E-Pc than in D-Pc.

Altogether, these results indicate that E-Pc are less effective in transducing biochemical and mechanical stimuli into modulation of gene transcription.

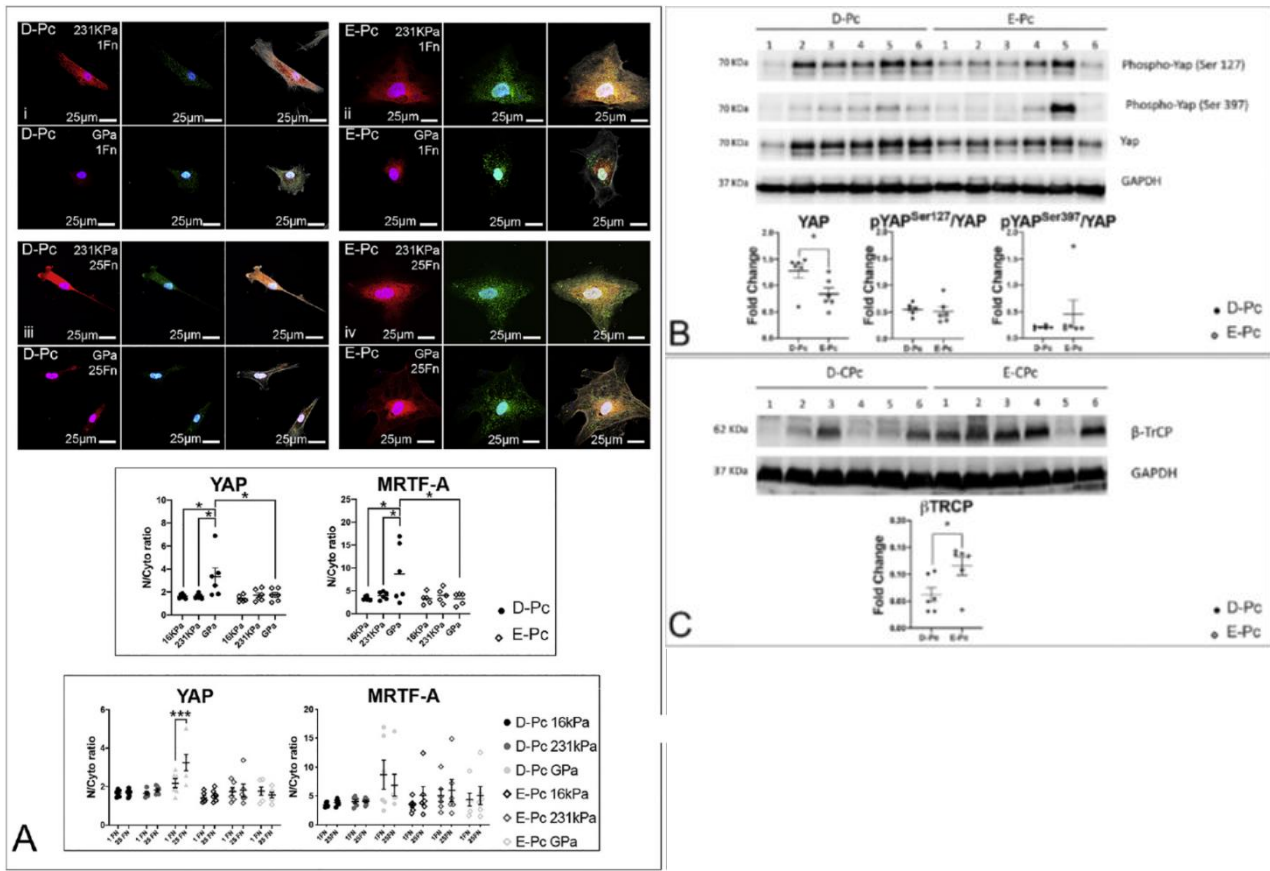


Figure 53: (A) immunofluorescence of YAP (in red) and MRTF-A (in green) in E and D-Pc on different substrates and different fibronectin concentration conditions. The corresponding dot plots show the ratio between the fluorescence intensity of the respective signals in the nucleus and the cytoplasm. (B) western blot showing the significative increase of YAP amount on hard substrates for D-Pc compared to E-Pc, (C) the significative increase of  $\beta$ TRCP for D-Pc compared to E-Pc when seeded on hard substrates

#### 4.4 Possible regulation of YAP nuclear translocation by different drugs

The effect of treatments with different drugs affecting upstream regulators of Hippo pathway was tested in order to better investigate the molecular pathways involved in YAP nuclear translocation and to assess the possibility to reverse Pc dysfunction.

The effect of serum starvation was evaluated, as LPAR2 (lysophosphatic acid receptor), a known YAP activator, was found to be more expressed in D-Pc compared to E-Pc. The effect of a ROCK inhibitor and also the sensitivity of D-Pc and E-Pc to latrunculin A, an inhibitor of actin cytoskeleton assembly, were tested. All the drug tested showed a reduction of YAP nuclear transfer after the treatment, in some case influenced by the increased fibronectin concentration.

The most interesting result, however was obtained when cells were treated with a MEK inhibitor, able to reduce the levels of total ERK. MAPK/ERK are emerging pathways that has been postulated to be involved in the modulation of YAP activation. E-Pc exhibit an increased level of ERK and phosphorylated ERK compared to D-Pc (figure 54, A, B).

The reduction of total ERK have as a result the increase in YAP nuclear localization in both D and E-Pc, independently from the fibronectin concentration (Figure 54, C).

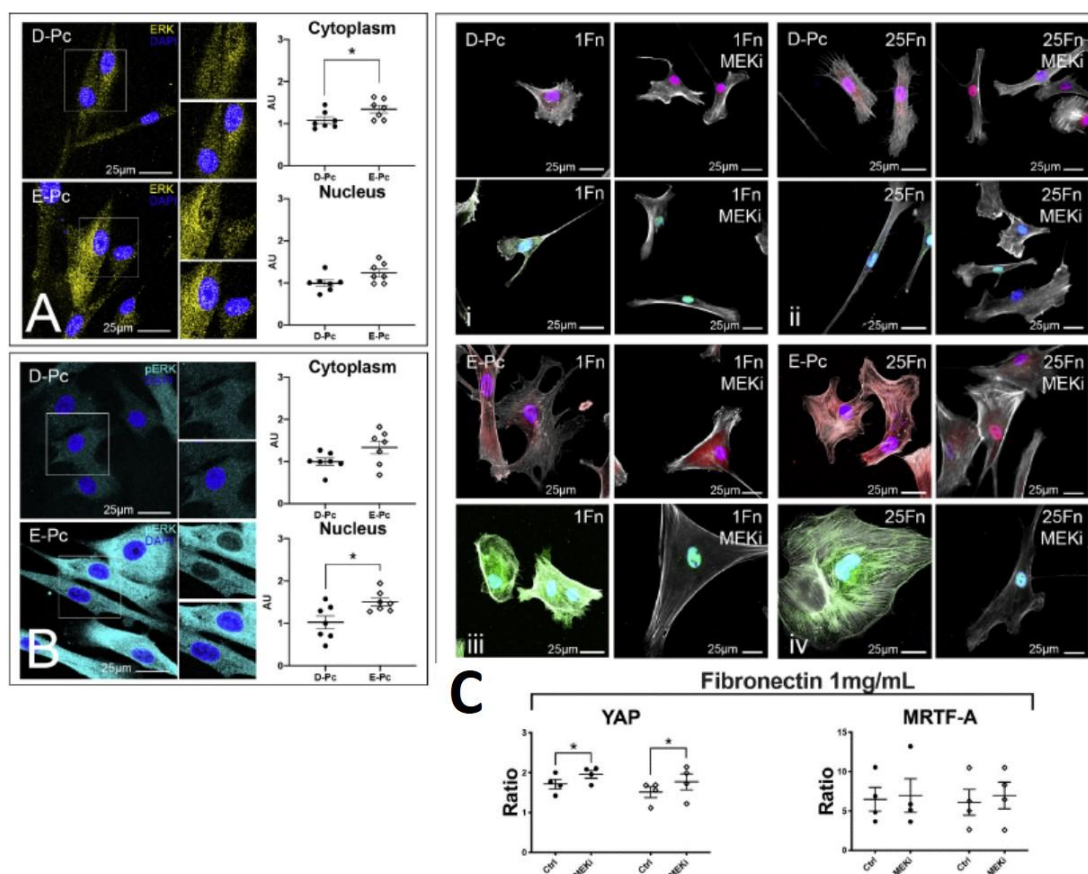


Figure 54: (A, B) immunoblot highlighting ERK and phospho-ERK concentration on pericytes. The amount of both is higher in E-Pc, (C) the effect of MEK inhibitor in increasing YAP (in green) and MRTF-A (in red) nuclear levels is shown in the microphotographs and highlighted in the dot plot where the ratio of N/cyt YAP is depicted, showing an increase in both D and E-Pc when the sample was tested with the drug

## 4.5 Conclusions

Ischemic heart disease (IHD) is a leading cause of mortality. Obstruction of the coronary arteries is the main studied effect, but the importance of microcirculation in dictating symptoms and prognosis is recently emerged.

Microcirculation disease can coexist with macrovascular atherosclerosis and as in the case of chronic ischemia, lead to myocardial hibernation (Ryan, 2018). Indeed, hibernated, reperfused hearts are characterized by reduced capillary density, inflammation, ongoing cardiomyocyte de-differentiation and cell death. The microvascular status of patients affected by end-stage heart failure is here analyzed. In most cases patients experienced an acute myocardial infarction ten years before transplantation and had a severely depressed cardiac function, only a minor portion of these patients had a known history of diabetes.

Experimental revascularization therapies could contrast hibernation and sustain myocardial function by promoting microvascular repair (Krichavsky, 2011). It was previously shown that administration of cultured pericytes could improve myocardial performance and promote angiogenesis after ischemic injury (Avolio, 2015).

Pericytes are contractile cells localized around the capillaries, they are surrounded by the basement membrane and have a branched, heterogeneous morphology and exert critical functions as blood flow regulation, immune cell trafficking and hemostasis to form blood-brain barrier. They recruit and stabilize endothelial cells in neovascularization processes (Attwell, 2016) (Nees, 2013).

Diverse functions can be exerted by different pericytes subpopulations and even though they display in vitro multilineage differential potential, whether Pc behave as multipotent cells in vivo is still debated (Su, 2020) (Guimaraes-Camboa, 2017).

The ability to stimulate angiogenesis has been linked to their mechano-transduction properties via Rho/ROCK signalling that in turn is a critical regulator of YAP/TAZ pathway (Aragona, 2013). Here, a reduction of nuclear translocation of YAP is shown in pericytes from ischemic hearts. At the

same time, a reduced ability of these cells to promote in vitro vascular network formation is demonstrated.

To find the molecular mechanism responsible for E-Pc dysfunction, the main regulatory pathways of YAP signalling have been investigated.

Defects in both mechanosensing and mechanotransduction were documented: a defective activation of FAK and a trend in reduced phosphorylation of p130Cas on hard substrates. Consistently, a significantly lower ability to modulate the cell mechanical properties as a function of substrate one was measured. Moreover, significant alterations in cytoskeletal components involved in these pathways were detected (change in focal adhesion and actomyosin). Other than biophysical stimuli, also biochemical ones as the concentration of fibronectin modulate the mechanical responsiveness of healthy pericytes (expressed by YAP nuclear translocation and changes in the cytoskeleton) but did not cause any response in E-Pc.

Then, Rho-GTPase, other well-recognized YAP regulators, were studied (Piccolo S. D., 2014). Lower levels of G-protein coupled receptors (as lysophosphatidic acid) in E-Pc were detected. The effect of serum starvation was F-actin disassembly and inhibition of YAP nuclear shuttling.

As cytoskeleton tension is essential for YAP function, the levels of another factor having a role of in actin dynamics was investigated (Moreno-Vincente, 2019). CAV-1 was more expressed in D-Pc than in E-Pc. Consistently, E-Pc were only modestly affected by the treatment with ROCK inhibitor that instead inhibited YAP nuclear translocation in D-Pc grown on stiff substrates.

Last, the impact of MEK/ERK signalling on YAP nuclear localization was studied as an upregulation of this pathway has been recently associated with CAV-1 deficiency and an activation of this pathway in E-Pc have been demonstrated (Strippoli, 2015). Importantly an increase of YAP nuclear translocation following MEK inhibition was observed in both D and E-Pc. This was explained with a downregulation of β-TRCP (a ubiquitin ligase that involves YAP degradation induced by MEK). These results are consistent with previous ones showing the independence between MEK/ERK and MST/Hippo pathways (Li, 2013).

Also the nucleus/cytoplasmic shuttling of the co-transcriptional activator MRTF-A was analyzed, since MRTF/SRF and YAP/TEAD pathways are mutually dependent. Similar to YAP, also MRTF-A nuclear localization was influenced by substrate stiffness and serum, but less dependent to fibronectin concentrations. Also for this factor, a reduction of its responsiveness to stimuli was observed in E-Pc. In conclusion, this study allowed to shed light on the mechanotransduction pathways impaired in pericytes derived from ischemic hearts that correlate with the reduced ability to sense and transduce environmental and mechanical stimuli. Modulation of upstream regulators of YAP pathway by means of small molecules (like MEK inhibitors) could be evaluated as a way to reverse Pc dysfunction and contrast CMD in heart failure.



# Chapter 5

## 5.1 Introduction

The pool of oocytes, with which a female mammal is provided, starts the meiotic maturation during the foetal development. At the birth, oocytes are arrested at the first meiotic prophase and are characterized by the presence of the germinal vesicle (GV). The breakdown of the nuclear envelope will not occur before the puberty, when oocytes enter the first meiotic division (MI). At the time of ovulation a mature oocyte (MII) is released from the ovarian follicle. After the release the oocyte is ready to be fertilized (Figure 55).

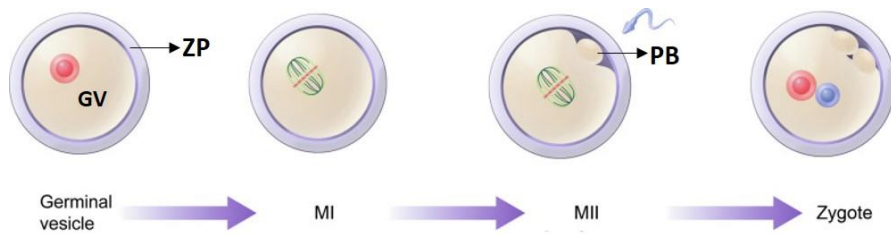


Figure 55: Maturation stages of an oocyte and main morphological features, an immature oocyte is characterized by the presence of the germinal vesicle (GV), that is no longer visible once the oocyte enters the meiosis (MI). At the end of the first meiotic division, the product of the meiosis, namely the first polar body (PB), is visible. The mature oocyte (MII) is fertilized leading to the zygote that will develop into the embryo. In the absence of fertilization MII oocyte goes through a process of apoptosis

In the absence of fertilization, the mature oocyte goes through a process of slow degradation culminating in apoptosis.

This phenomenon is called “post-ovulatory ageing” and the duration of this process varies according to species: in human the useful time window for fertilization is lasts up to 24h, while in mice is shorter than 8-12h (Miao, 2009). The oxidative-stress is thought to be the main responsible of the ageing processes, which lead to different events: a decreased level of the maturation promoting factor (MPF, a cellular factor involved in maintaining the cell cycle on idle); the mitochondrial dysfunction related to the damage of DNA and membranes; the impairment of  $\text{Ca}^{2+}$  channels and ATPases that affects

$\text{Ca}^{2+}$  homeostasis and variations in the dynamics of actin-tubulin assembly that are related to the formation of the meiotic spindle (Lord, 2013) (Fissore, 2002).

A further key event related to the post-ovulatory ageing is the occurrence of a spontaneous cortical granule (CG) exocytosis (Miao, 2009). CG exocytosis is a reaction that normally occurs as a direct consequence of fertilization and it involves the release of ovastacin, a protease that cleaves and cross-links the ZP2 one of the three glycoproteins of the ZP (Monnè, 2011). This event causes considerable changes of the ZP structure: the thickness of the fibrils increases, and the mechanical properties change as shown by the increase in the stiffness and proteolytic resistance after the fertilization (Coy, 2008) and, finally, it is thought to avoid the occurrence of the polyspermy by hindering the penetration across the ZP of an excess of spermatozoa (Avella, 2014) (Burkart, 2012) (Papi, 2010). However, this ovastacin-mediated “zona hardening” is a slow reaction taking place in hours from the fertilization. A fast block of the polyspermy occurring at the level of oocyte ZP has only been postulated, the main hypothesis being related to the release of some molecules or ions (as  $\text{Zn}^{2+}$ ) able to directly induce a fast crosslinking of this glycoproteic layer (Que, 2017) (Figure 56).

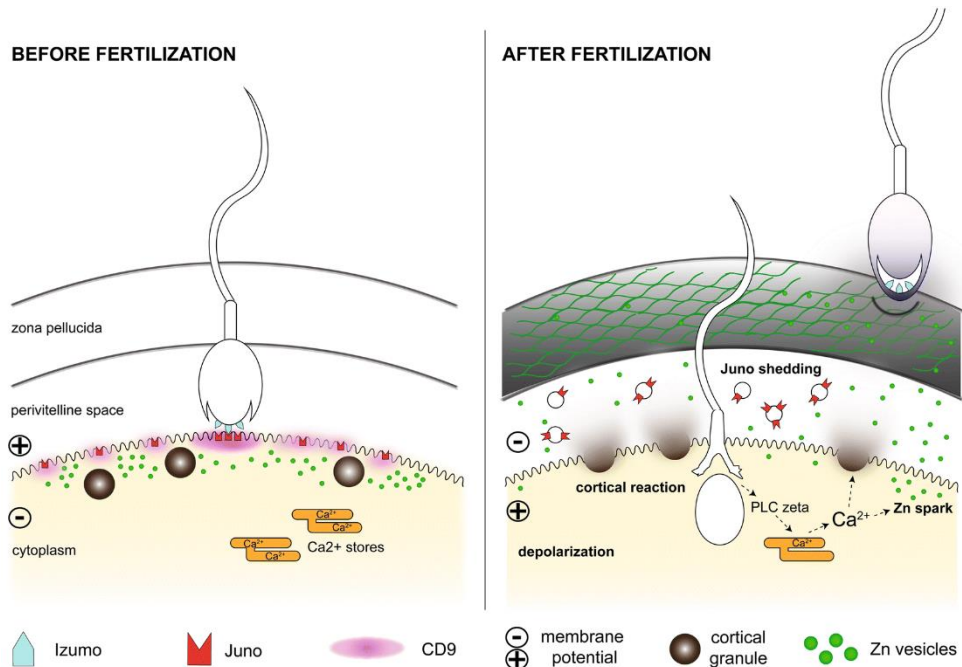


Figure 56: sperm-egg interaction during fertilization, after the sperm entry the release of  $\text{Ca}^{2+}$  induces the CG exocytosis. One of the released factors are  $\text{Zn}^{2+}$ ions, that are thought to mediate the ZP cross-linking providing a fast block of the polyspermy

The occurrence of a similar reaction in the aged oocyte has been demonstrated in mouse during the oocyte post ovulatory ageing. In particular, CG release remains constant for a certain time window after ovulation until an altered CG distribution on the cortex can be detected due to the postovulatory ageing progression. This change in the CG distribution is an important indicator of egg cytoplasmic degeneration that frequently occurs before the appearance of ageing related spindle abnormalities (Ducibella, 1990). This event should provide valuable information about the egg's normal fertilizable lifespan and the presence of this reaction during the oocyte postovulatory ageing could involve a change in the ZP structure that aims to prevent the fertilization of the aged oocyte.

The clinical implications of post-ovulatory aging include the decreased rates of fertilization (as it occurs in “rescue ICSI (Intra Cytoplasmic Sperm Injection)” performed on failed-to-fertilize oocytes), the loss of the embryo uterine implantation capacity and the impaired development during embryogenesis. Moreover, dysfunctional mitochondria and altered epigenetic profile can cause abnormalities in offspring (growth retardation, decreased reproductive fitness and longevity) (Tari', 2002) (Kuczynski, 2002).

In the in vitro fertilization (IVF) practice, in order to increase the number of the competent oocytes, women are treated with different gonadotropin stimuli to induce superovulation, therefore the retrieved oocytes can have different maturation stages. The embryologist selects competent MII oocytes looking at those visual morphological features that are commonly related to mature healthy oocytes. In figure 57, different oocyte dysmorphologies are depicted. The presence of the first polar body (PB), the regular structure and thickness of the zona pellucida (ZP) and the absence of cytoplasmic granularity are only some of the key parameters considered (Sauerbrun-Cutler, 2015) (Gabrielsen, 2001).

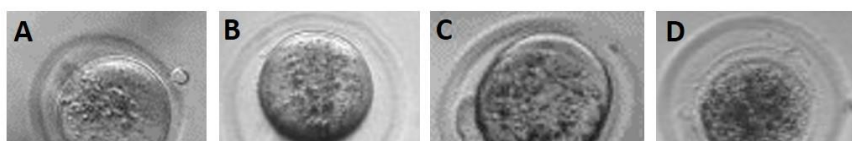


Figure 57: (A) An oocyte with healthy morphological features and the presence of the polar body (PB) and (B-D) different oocyte dysmorphologies as a too large perivitelline space (PVS) (B), a fragmented ooplasm (C) and the occurrence of oolemma rupture (D)

While the maturation phase of an oocyte can be identified with the help of an optical microscope, the post-ovulatory age has no visible morphological features. Visual inspection allows to separate apoptotic oocytes from those showing still “healthy features”, but among them only a few have the potential to generate live birth. Often fertilization does not occur, the embryo development stops at the first divisions or results in the blastocyst adhesion failure to the endometrial tissue. As the precise moment of the entry in meiosis phase cannot be known, it should be considered that oocytes retrieved from the superovulation practice may have different post-ovulatory age, and thus different chances of a positive outcome of the IVF practice.

The epigenetic profiles are different in the aged oocytes and this leads to a change in the genetic expression and errors during the meiosis (Miao, 2009). Abnormalities can be detected in the location of the microtubules and the shape of the mitotic spindle. The possibility to delay this process by controlling the activity of some key factors like maturation promoting factor (MPF) has been investigated (Kikuchi, 2000). In particular, factors that accelerate this process are reactive oxygen species, on the contrary caffeine has been shown to delay the ageing process. To determine the stage of MII oocyte, further analytical approach, beyond visual inspection, have been proposed such as genetic screening, spectroscopy-based metabolomic profiling, enzymatic activity assays, protein expression analysis on follicular fluids and polscope-based spindle imaging (Mehta, 2013) (Han, 2011) (Assou, 2010) (Tomari, 2018). However, the majority of the techniques used to evaluate the ageing occurrence are invasive and involve the oocyte deterioration, and are potentially dangerous for the embryo’s fate. (Sun Q. W., 2007).

A quicker and non-invasive alternative is needed to precisely determine the MII stage of the oocyte. Recently there is a growing attention to the cellular mechanical properties for their relation to the physiological or pathological cell status (Hang, 2021) (Butcher D. T., 2009) (Katira, 2012).

A first hit of the importance of the mechanical properties of the oocytes with respect to the yields of IVF can be found in the correlation between the force loading necessary to pierce the ZP during the ICSI practice and the embryo yields. The optimal penetration depth of the injection needle prior to

puncture of the ZP is at the centre of the oocyte, if puncture occurs before or after that point the ICSI failure probability increase (Khalilian M. V.-Y., 2013).

Biomechanical parameters, evaluated by means of different techniques here shortly depicted in Figure 58 for what concerns oocyte applications and described in detail in the second chapter of this essay, has been proved to be good non-invasive predictors for embryo and zygote viability as well as for the detection of the maturation phases of the oocytes (Yanez 2016). Micro-tactile sensors and micropipette aspiration of whole oocytes allowed to investigate the “zona hardening” phenomenon that results in a ZP stiffening after fertilization (Y. Murayama 2006) (Khalilian M. N., 2011).

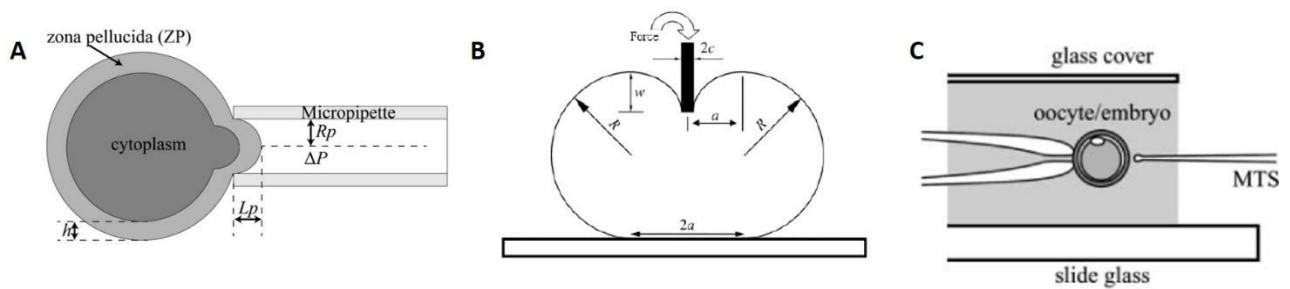


Figure 58: Three different methods used for the investigation of oocyte mechanical properties, (A) micropipette aspiration, (B) micropipette indentation, (C) micro-tactile sensor

Indentation measurements performed by Atomic Force Microscopy (AFM) of isolated ZP allowed to identify the contribution of two layers with different mechanical properties, which were observed to be involved in the post-fertilization cross-linking of this glycoproteic membrane (A. Boccaccio 2012).

AFM based indentation performed on whole human oocytes allowed to detect a significant difference in ZP stiffness among immature, competent (classified by visual inspection) or rejected oocytes, thus suggesting that the AFM approach can be particularly attractive for the small deformations and the range of force applied compared to the previously mentioned techniques (L. Andolfi, 2016). As stressed in Figure 59 in which different techniques used for this purpose are compared, in general the higher are the force loading range and the deformation values applied to the cell, the higher is the value of the Young modulus ( $E$ ) measured.

Method	Force loading /ΔP applied	Deformation/ Aspiration lenght	E (Young modulus)	Model
<b>Micropipette indentation</b>	7,5µN	44 µm	17,9 kPa	Biomembrane Point Load model (Sun et al., 2003)
	0,5µN	35 µm	3,1 kPa	Maugis-Dugdale model (Liu et al., 2012)
<b>Micropipette aspiration</b>	0,8 kPa	28 µm	11,8 kPa	Cortical shell-liquid core model (Khalilian et al., 2011)
<b>Microtactile sensor (MTS)</b>		10 µm	8,26 kPa	Hertz model (Murayama et al., 2006)
	1 nN	1-2 µm	0,15 kPa	Current study
<b>AFM-nanoindentation measurements</b>				

Figure 59: Different techniques used for measuring mouse oocytes mechanical properties, the range of forces and deformation applied and the calculated Young modulus

## 5.2 Methods

### 5.2.1 Mouse oocytes retrieval and cumulus cells removal

Mature oocytes (MII) were retrieved from seven weeks old C57BL/6 superovulating mice, that were previously subjected to injection of different gonadotropin stimuli: 7.5 IU of PMSG followed 48 h later by injection of 7.5 IU of hCG. Mice were sacrificed by cervical dislocation and oocytes were recovered from ovaries 16 h after the hCG injection into α-MEM supplemented with BSA (4%). Cumulus cells (CCs) were removed by means of a mechanical treatment by pipetting COCs (cumulus oocytes complexes) with 100µm inner diameter sized flexipets in α-MEM supplemented with 0.03% hyaluronidase (as shown in Figure 60). Every step, from the retrieval to the CCs removal was performed in drops of 100-200 µl to fast and ease the manipulation procedures. Finally oocytes were

transferred to a petri dish filled with fresh medium ( $\alpha$ -MEM) supplemented with BSA and they were left to recover for 1hour.

Then, oocytes were either immobilized on the surface of petri dishes in  $\alpha$ -MEM supplemented with HEPES without BSA, in order to perform the measurements, or frozen.

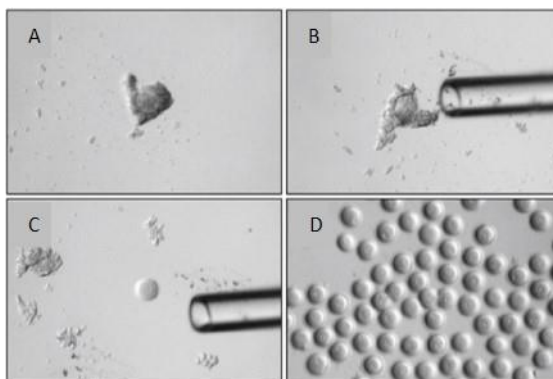


Figure 60: COCs retrieval (A) and cumulus cells removal by the mechanical treatment in the hyaluronidase solution (B-C)

### 5.2.2 Oocyte freezing and thawing procedure

After the removal of the cumulus cells, oocytes were transferred, by the help of micropipettes for the manipulation, into a drop of  $\alpha$ -MEM supplemented with 20% FBS and incubated at 37°C 5% CO<sub>2</sub> for 30min. The incubation with the serum allows to avoid damages to the ZP during the freezing procedure.

In the meanwhile, cryogenic tubes were put inside a box with ice and for each one 5  $\mu$ l of PB1 supplemented with 1M DMSO were added (Nakao, 1997). There, oocytes are transferred to the same 1M DMSO solution. It is important to stress here that this is a very delicate step and everything has to be done very fast to avoid the oocytes degradation. Oocytes are transferred to the cryovials (5 oocytes/vial) with the micropipettes and left in ice for 5/10 minutes. After that, 45  $\mu$ l of

cryoprotective agent (DAP213) were added for each vial and left equilibrate again for 5/10 minutes before plunging in liquid nitrogen (LN). The procedure is shown in Figure 61 (Nakagata, 2013).

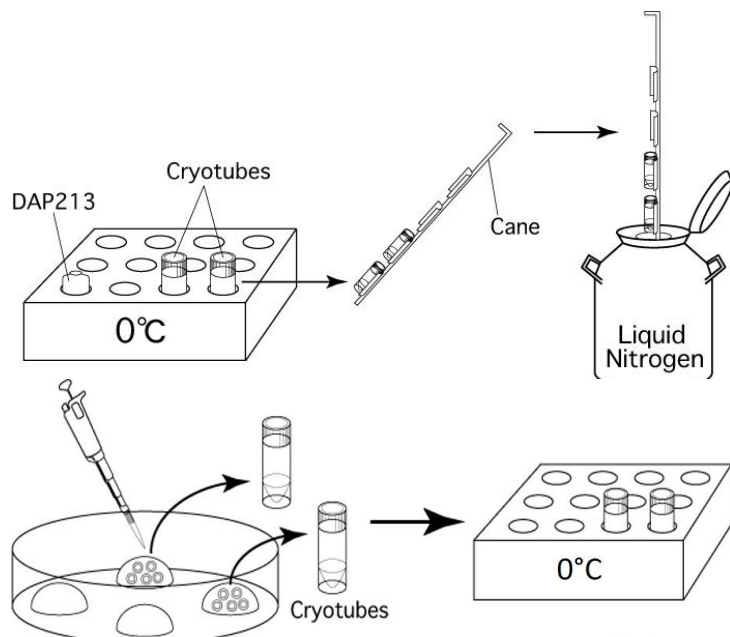


Figure 61: Cryotubes loading and slow freezing procedure consisting in a first step freezing with DMSO and a second one with DAP213 before plunging the sample in liquid nitrogen

For oocytes thawing, 0.25M sucrose solution in PB1 was prepared and warmed before use. At the same time 2 ml of fresh medium ( $\alpha$ -MEM with 4% BSA) were warmed in a 35 mm petri dish. A vial is removed from liquid nitrogen and, after LN discarding, 1.5 ml of thawing solution was put inside, by gently pipetting the sample was dissolved and the drop transferred to a petri dish. Also, this step is very delicate and has to be performed very quickly in order to avoid oocyte degradation. Here, with the help of manipulation pipette, oocytes are transferred to the petri dish with the  $\alpha$ -MEM medium inside and left to recover in the incubator for at least 30-40 minutes.

### 5.2.3 AFM-indentation measurements

After removing the cumulus cells, oocytes were immobilized on the surface of petri dishes in  $\alpha$ -MEM medium, without BSA, with incubation of 1h in 5% CO<sub>2</sub> at 37°C. MII oocytes were selected by visual inspection according to the presence of the first PB. Only MII oocytes with a round-shaped ooplasm, a regular ZP and perivitelline space (PVS) were considered for the analysis. AFM-indentation measurements were performed after 1h from the retrieval with a Nanowizard II AFM equipped with an inverted optical microscope. The selected indenter was a bead mounted cantilever whose fabrication and calibration procedures are described in Chapter 4, section 4.3.5.

Measurements were performed directly in the petri dishes, on a squared grid of 3x3 $\mu$ m at the centre

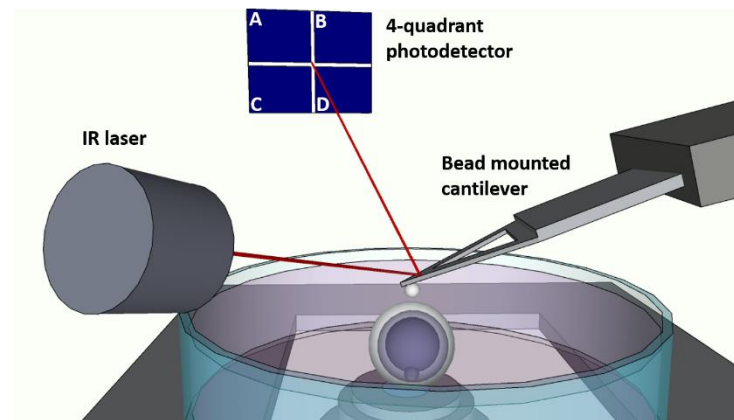


Figure 62: the oocyte is anchored at the centre of the petri dish and measured by AFM-indentation with a triangular cantilever with a glass bead glued on the tip. The deflection of the cantilever during the indentation is measured by the displacement of the IR laser on the 4-quadrant photodiode.

of the oocyte (as shown in Figure 62). For each point 3 force-distance curves were acquired, for a total of 27 curves for each oocyte. Between subsequent measurements a recovering time of 5/10 s was imposed. This time is sufficient to avoid the measurements to be impaired by the first loading as it is confirmed by the oocyte constant mechanical features up to 90 min detected in the absence of external stimuli addition (Figure 85F, section 5.3.6). A maximum force load of 1 nN at a rate of 5  $\mu$ m/s in z closed loop feedback mode was used. The complete measurement acquisition takes no more than 5 min for each cell.

Force-distance curves were converted into force-indentation curves as previously described in Chapter 3 and 4. In order to take into account the contributions of different layers with different elastic moduli, like already shown for human oocytes (Andolfi L. M., 2016), the resulting curves were fitted by using a Sneddon modification of the Hertz model for the elastic indentation of a soft sample by a stiff sphere, in which two contact points ( $z_1$  and  $z_2$ ) can be identified corresponding to two different layers. The first part of the curve (when  $z_1 < z < z_2$ ) has one contribution and is described by the Hertz model:

$$z \in [z_1, z_2] \quad f_0 = \frac{4}{3} \sqrt{R} \left[ \frac{E_1}{1 - \nu^2} (z - z_2)^{\frac{3}{2}} \right]$$

Where R is the radius of the bead,  $\nu$  is the Poisson ratio (conventionally set to 0.5 for cells),  $f_0$  the applied force and  $E_1$  the Young modulus corresponding to this layer.

The second part of the curve (when  $z > z_2$ ) is a sum of the internal and external layer contributions:

$$z > z_2 \quad f_0 = \frac{4}{3} \sqrt{R} \left[ \frac{E_1}{1 - \nu^2} (z - z_1)^{\frac{3}{2}} + \frac{E_2}{1 - \nu^2} (z - z_2)^{\frac{3}{2}} \right]$$

Where  $E_1$  is the Young modulus of the first layer and  $E_2$  of the second one, as shown in Figure 63.

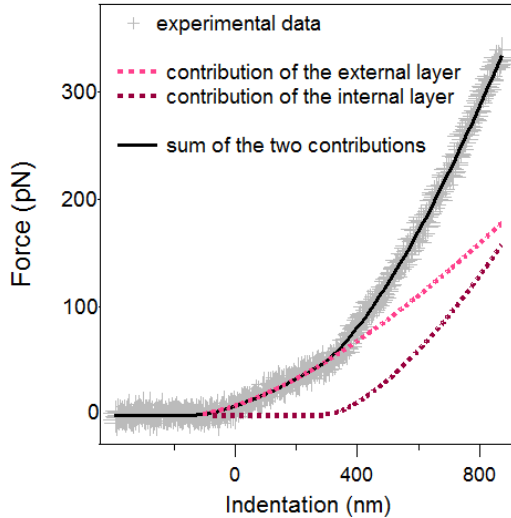


Figura 63: The force-distance curves are fitted through a modified Hertz model that takes into account the contribution of two layers (dashed lines)

This equation provides the phenomenological description of the indentation. The interplay between the mechanical properties of the two layers is not considered. This model reproduces the data quite well and is more than enough to interpret our data.

The fitting procedure and the Young moduli calculations for each oocyte was performed by an Igor procedure.

By the force distance curves, another parameter can be also calculated by integrating the area included between the approach and the retraction curves in the positive force region (Figure 64). This is the dissipated viscous energy and is directly related to the cell viscosity (Yun, 2017): the dissipation energy was evaluated using a MatLab routine developed on purpose.

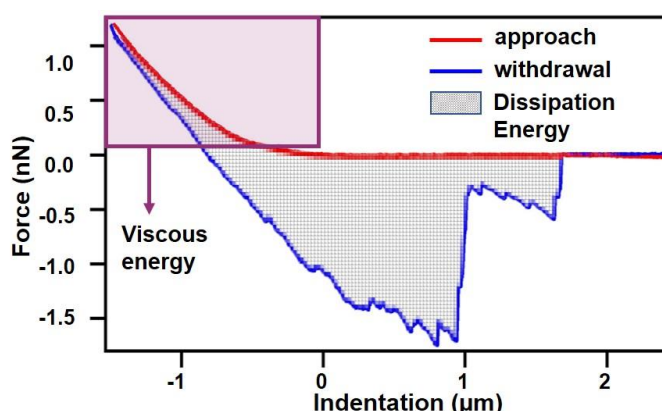


Figure 64: The dissipation viscous energy is shown in the figure as the area between the approach and the retraction curves in the positive force region.

#### **5.2.4 Macro-probes fabrication**

For stress-relaxation measurements, we designed and fabricated AFM-macro probes that allow to uniformly compress the whole oocytes with forces in up to few hundreds of nN, measuring the viscoelastic properties of the oocyte two main components: the ZP and the ooplasm. The design of the probes was carefully modelled to establish the geometrical features that provide an effective spring constant of 7N/m, which could allow to compress easily a large heterogeneous biological sample. For this reason, the selected geometry was a square area of 300 x 300 µm in size connected with the solid chip with two arms of 100 x 100 µm.

The main fabrication steps are shown in Figure 65. On a silicon wafer (thickness 500 µm), covered by a layer of silicon nitride with a thickness of 2µm on both sides, a thin layer of chromium (100 nm) was deposited by sputtering on both sides. One side of the wafer was spin-coated with a photoresist sensitive to UV radiation and a glass mask with the bottom side of the macro cantilevers was positioned on top. After UV exposure to impress the pattern, it was immersed in the appropriate solvent to develop the resist. After this step, the chromium was patterned by wet etching using the appropriate etching solution, leaving parts of the silicon nitride unprotected. A reactive ion etching (RIE) step etched the SiN exposing the silicon underneath, which was then removed by wet etching down to a depth of 450 µm. The pattern impressed on the back side of the silicon nitride included alignment holes which were punched after the silicon etching. The previously described process was repeated on the front side of the wafer, where the pattern impressed included the shape of the chip and the probes. The final step was the etching of the residual silicon layer to suspend the silicon nitride macro-probes.

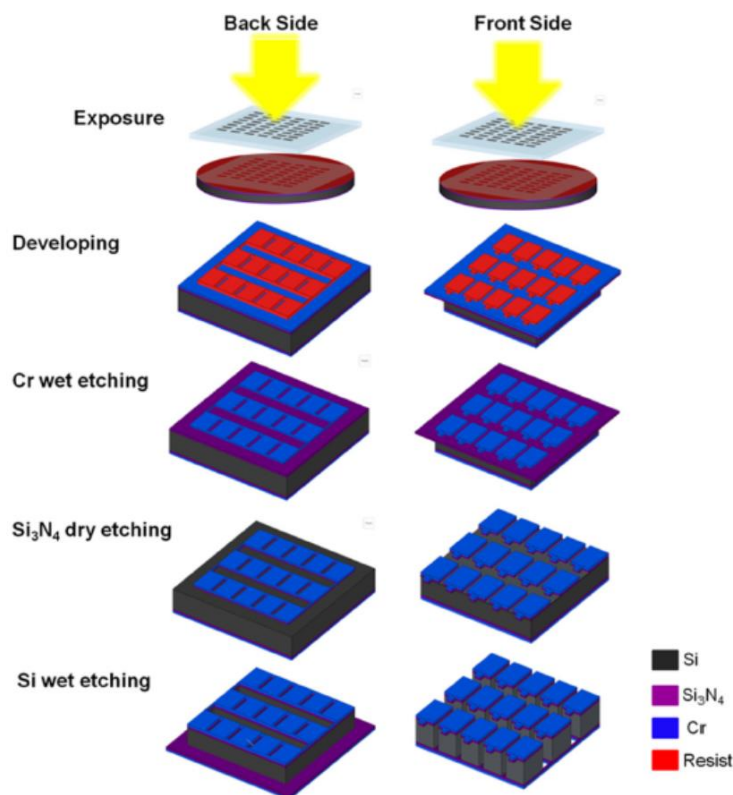


Figure 65: Fabrication procedure of the macro probes. Resist exposure and development and following etching steps for Cr, Si<sub>3</sub>N<sub>4</sub> and Si removal

At the end of the fabrication process, a polymeric wedge was added below the squared probe, in order to provide a parallel compressing surface and to correct the cantilever mounting tilt. A drop of a UV-curable glue was placed on an hydrophobic support. Then the probe was brought into contact with the glue and illuminated with UV laser light for few minutes. The result is shown in Figure 66.

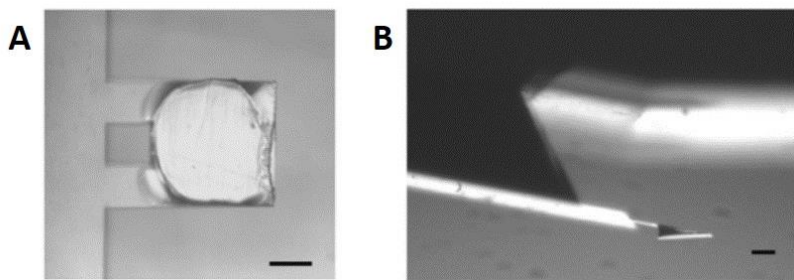


Figure 66: optical images of wedged macro-probe, bottom view (A) and side view (B)

### 5.2.5 AFM stress-relaxation measurements

The spring constant of macro-cantilevers was calibrated by the spring on spring method (Gates, 2007). In this procedure a cantilever with known spring constant was used as a reference. The spring constant of the macro-AFM probe ( $K_c$ ) was calculated according to the equation:

$$K_c = Kr \left( \frac{Sr}{S} - 1 \right)$$

where  $K_r$  is the elastic constant of the reference cantilever,  $S_r$  is the sensitivity (nm/V) of the combination of macro-probe and reference cantilever, and  $S$  is the sensitivity of the macro-probe. As reference, a commercial cantilever whose actual spring constant was previously evaluated to be 0.8 N/m was used. The AFM macro-probe was then mounted on the AFM-glass cube and, after the laser alignment, it was first pressed against the reference cantilever to obtain  $S_r$  and then against the edge of the reference chip to obtain  $S$ . The AFM macro-probes used here had a spring constant average value of  $1.7 \pm 0.4$  N/m.

Oocytes were immobilized into an overhanging support consisting of a plastic coverslip glued on a microscope glass slide, all placed in a plastic petri dish. The sample was located into a drop of medium placed on the border of this stepped coverslip. This setup, shown in Figure 67, allowed the side view of the sample through the use of an holder bearing a mirror positioned in front of the cantilever and prevents the crashing of the side-view mirror on the sample support while performing the measurements.

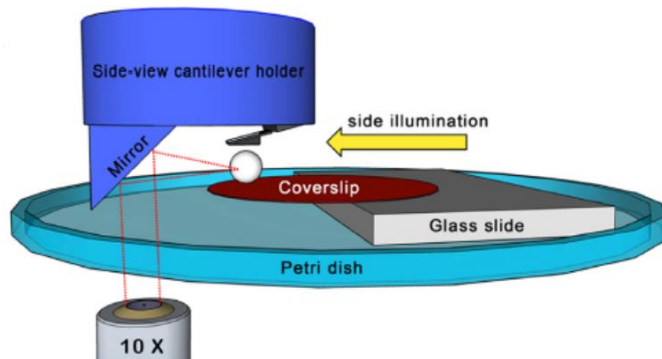


Figure 67: schematic diagram of the setup used for side-view imaging and stress-relaxation measurements, oocytes are put at the border of a “overhanging” plastic coverslip, with the help of a side illumination it is possible to look at the side image of the sample reflected on the mirror

The cantilever was brought into contact with the sample and the petri dish lid containing the support was filled with the medium. At this point, the sample and the cantilever stages were displaced to allow the objective to focus on the mirror and switch, by the help of a side illumination, to the side-view imaging. The macro-probe was then approached and put in contact with the sample. A CellHesion module that allows to extend the range of the piezo from 15 µm to 100 µm was used. The sample was compressed of 20 µm from the contact position with a speed of 2 µm/s and a closed-loop piezoelectric control was used to maintain the deformation constant for 30s.

During this time, the time evolution of force exerted by the cell on the probe (force -relaxation) was measured. At least 5 curves per cell were acquired. The force-relaxation curves can be fitted with a generalized Maxwell model to account for the contribution of different layers, as already discussed in chapter 2. In agreement with previous studies, two Maxwell elements were sufficient to describe the experimental data (Shen, 2019). The equation that describes the model is the following:

$$F(t) = a_0 + a_1 \exp\left(\frac{-(t-t_0)}{\tau_1}\right) + a_2 \exp\left(\frac{-(t-t_0)}{\tau_2}\right)$$

Where  $a_0$  is the coefficient of the elastic portion of the strain,  $a_1$  and  $a_2$  are the coefficient of the viscoelastic portion of the strain and correspond to the two Maxwell elements.  $\tau$  is the relaxation time defines as:  $\tau = \frac{\eta}{E}$  where  $\eta$  is the viscosity of the sample and E the Young's modulus. An Igor procedure was used to fit the data and calculate the relaxation time.

### 5.2.6 Cortical granule staining

The CG exocytosis was evaluated in real time after the previously mentioned oocyte immobilization on the supports. A fluorophore (25µg/ml of FITC-LCA) that binds to the  $\alpha$ -mannose that is part of the glycosylated components released by the exocytotic process together with other molecules (mostly enzymes like proteinases and glycosidases) was added to the culture medium without BSA. As long as CG exocytosis takes place, the concentration of  $\alpha$ -mannose in the perivitelline space

(PVS) increases and this could be detected by the localized increase of the fluorescence in that area, as shown in Figure 68 (Cappa A. I., 2018). Images with an exposure time of 500 ms were acquired every hour to monitor this process in relation to post-ovulatory ageing or every 5sec when monitoring the process of the oocytes parthenogenetic activation,. The fluorescence intensity profile was drawn and the area underneath the peak corresponding to the PVS was calculated for different profiles of the same cell for a given time. The background fluorescence, originated by unbound molecule, a-specifically dispersed in the medium, was subtracted and the mediated values were plotted.

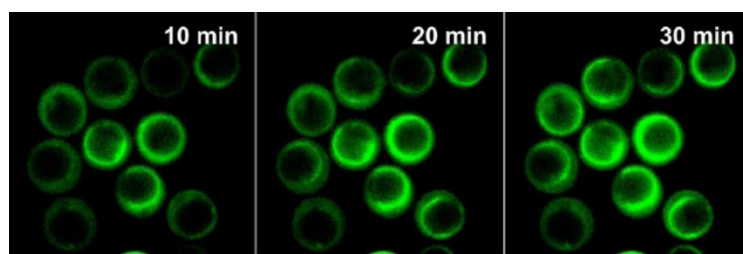


Figure 68: Epifluorescence images showing the increased fluorescence of FITC-LCA in the PVS after addition of the parthenogenetic activator (after 10, 20 and 30 min)

### 5.2.7 ZP removal

Oocytes were transferred to a drop of acid Tyrode's solution (Nagy, 2006) and mechanically pipetted with micropipettes having a capillary diameter of 100-150 $\mu$ m. This step has to be performed quickly (less than 10 s) in order to avoid the collapse of the ooplasm. Oocytes were then transferred to a second drop of medium with BSA and left equilibrate for at least 15 min before performing the measurement.

This procedure does not affect the oocyte quality as it has been optimized to implement the rate of the implantation after the fertilization of zona-free oocytes (Jelinkova, 2003).

### 5.2.8 Cumulus cells retrieval and culture

To enable the measurement of the oocytes, the removal of the cumulus cells, as previously described, was necessary. However, the release of sperm attractive factors by these cells influence spermatozoa

binding and penetration increasing the yields of the fertilization (Huang, 2010). Therefore, to encompass this limitation, cumulus cells were plated and grown for one or two days inside the fertilization drops before the oocyte transfer (Figure 69). For the cumulus cell retrieval, cumulus oocytes complexes (COCs) were transferred to a drop of 10 $\mu$ l of  $\alpha$ -MEM supplemented with 0.03% hyaluronidase by the help of a serological pipette. Then oocytes are mechanically treated with the micropipettes (as previously described) and once CCs are detached they are set aside while at least 100 $\mu$ l of  $\alpha$ -MEM with 20% FBS are added to the CC drop in order to dilute the enzyme solution (1:10). Then, in order to avoid the drop evaporation and to prevent contaminations, the petri dish is filled with paraffin oil. Therefore, the petri is left in the incubator (5%CO<sub>2</sub>, 37°C) for 2-3h, the time sufficient for the CCs to adhere. Then, 2-3 washing steps are performed by removing the medium (always operating under paraffin oil) and replacing it with warm PBS. Finally, an incubation medium (we used  $\alpha$ -MEM without HEPES and supplemented with Pen/Strep 1%) was put inside the drop and cells can be cultured until reaching the confluence and more times harvested up to 30 days of culture (Chermuła, 2020). But, for our purpose, 1-2 days were sufficient.

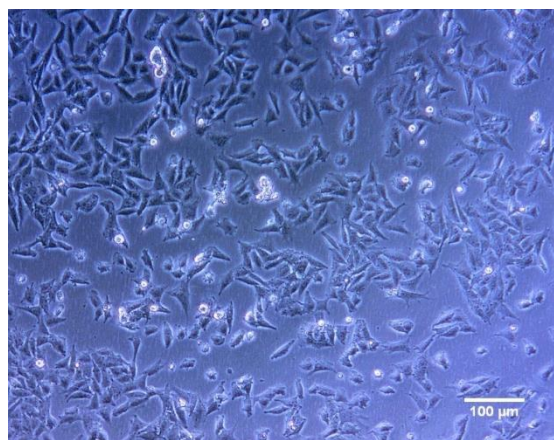


Figure 69: phase contrast image of in vitro cultured cumulus cells

### 5.2.9 In vitro fertilization

7-8 weeks old male mice were sacrificed and sperm cells were recovered from the cauda epididymis and transferred in a drop of medium (90 $\mu$ l/mouse) under paraffin oil. The medium was prepared according to the protocol described by the EMMA (European Mouse Mutant Archive) organization

(Takeo T. H., 2008) (Quinn, 1985). Briefly, for the sperm cell capacitation, a medium with a high level of  $\text{CaCl}_2$  was used in which 0.1% methyl- $\beta$ -cyclodextrin (MBCD) was added. This molecule, together with  $\text{Ca}^{2+}$  are needed for the sperm hyperactivation that consists in the change in sperm motility from straight trajectories to circular ones (Ho, 2001). Sperm cells are incubated for one hour in this medium. In the meanwhile, the drop with the cumulus cells in culture was took and the medium was substituted with the fertilization medium (HTF supplemented with 0.07% reduced glutathione) (Takeo T. N., 2011). For an effective fertilization, the drop of medium has to be very small ( $100 \mu\text{l}$ ) as the yields of the procedure depends also from the concentration of sperm cell and oocytes per drop (Hasegawa, 2014). In our experiment, we used at least 5 oocytes per drop with the

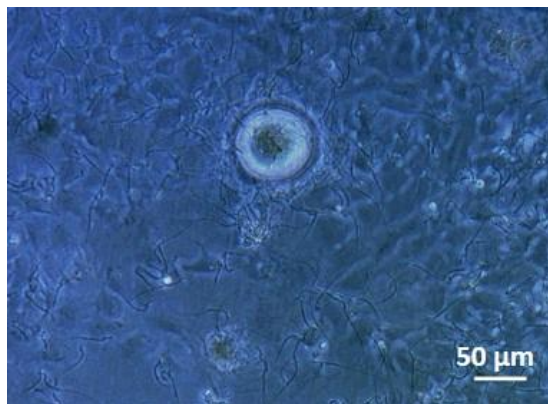


Figure 70: Phase contrast image of oocyte and spermatozoa inside the incubation drop above the layer of cumulus cells

addition of  $5\mu\text{l}$  of sperm suspension. When collecting the sperm cells, only the ones at the border of the drop has to be taken as in that region accumulate the capacitated spermatozoa. After the addition of the gametes, the fertilization drop is stored in the incubator. One oocyte inside the fertilization drop is shown in Figure 70, the layer of cumulus cells is visible below.

After three hours, oocytes are removed from the droplet and moved to another drop of HTF medium without reduced glutathione in order to remove the excess of sperm cells and the cell debris. At this time, fertilization has already occurred. The following steps are the formation of male and female pronuclei (6h from the fertilization) and, 24h later, of the 2-cell embryos. The timeline of mouse embryo development is depicted in Figure 71.

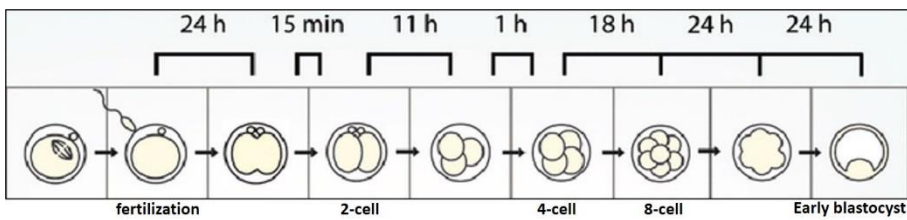


Figure 71: timeline of the embryo development from fertilization to the last step of in vitro culture, the blastocyst

## 5.3 Results

### 5.3.1 AFM investigation of the mechanical properties of mouse oocytes

We investigated the mechanical properties of the whole mouse oocyte by performing AFM indentation measurements on a population of 20 denuded MII mouse oocytes retrieved from 6 different superovulating mice. We used tipless triangular cantilevers with  $4.5\mu\text{m}$  beads glued at their ends that were approached to a small region at the top of the cell.

To average the local inhomogeneities that characterize the outer layer of the ZP, the AFM indentation were performed on a  $3\times 3 \mu\text{m}$  grid, like exemplified in Figure 72.

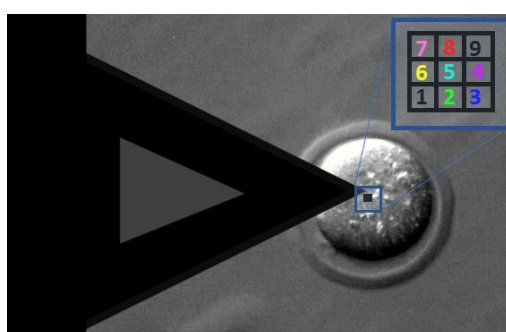


Figure 72: Tip position at the centre of the cell, the measurement is performed on a grid of 9 points in a squared area of  $3\times 3 \mu\text{m}$

The analysis of force-indentation curves highlighted the presence of two slopes similarly to what observed for human oocytes (Andolfi L. M., 2016), therefore we used the fitting procedure described

previously based on the modified Hertz model to take into account the presence of the two contributions.

As a result, two elastic components were obtained: a first Young modulus (E1) related to the outermost layer of the ZP and a second Young modulus (E2) associated with the more internal part of the ZP (as shown in Figure 73).

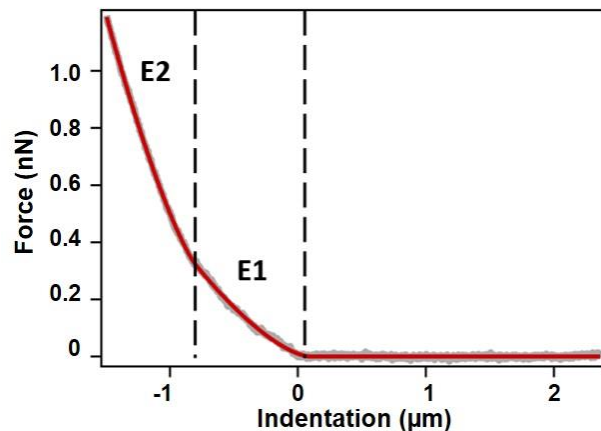


Figure 73: A force-distance curve is shown, in which the presence of two different layers having a different value of the Young's modulus (E1 and E2) is highlighted

Lateral imaging of the indentation process highlighted that the contribution of the rest of oocyte such as PVS and ooplasm, if present, is negligible (Figure 74). For this reason we considered the moduli E1 and E2 only related to the zona pellucida.

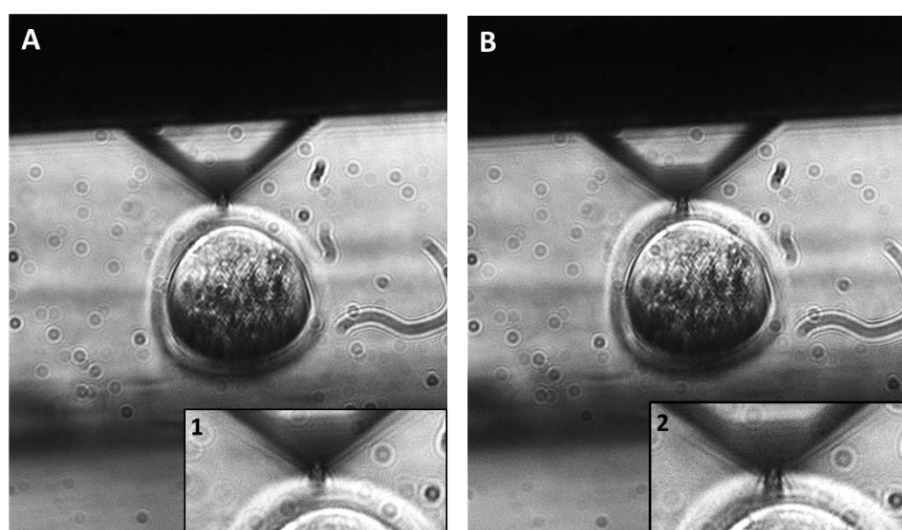


Figure 74: side view imaging of an oocyte indented by a bead-mounted triangular cantilever, the position at static contact (A, 1 zoomed) and the maximum indentation depth (B, 2 zoomed) is shown: no deformation of the PVS and ooplasm is observed. From this evidence we conclude that both measured Young moduli should be referred to the ZP.

The resulting E1 and E2 values obtained for each point of the grid are reported for several oocytes in Figure 75. Within the same oocyte, the E1 values are scattered with a variability comparable to the variability from cell to cell. Due to the micrometric irregularities, glycoprotein protrusions and the porous mesh-like structure of the mature oocyte ZP present on the surface of the oocyte the mechanical properties of the outer layer are not uniform (Figure 75 A, B), and depend strongly on the specific measurement location (Figure 75 C) which, hinder the use of this parameter to produce a meaningful discrimination between different cells.

On the contrary, the E2 values obtained on different positions of the same cell resulted narrowly distributed and allowed its selection as a marker to identify different oocytes (Figure 75 D). Indeed, the analysis of E2 returned consistently different values for different oocytes, and distinguishable values also for different positions within the same oocyte.

These observations suggested the choice of E2 as a reliable and sensitive parameter to investigate the evolution of the mechanical properties of ZP and the oocyte upon postovulatory ageing process

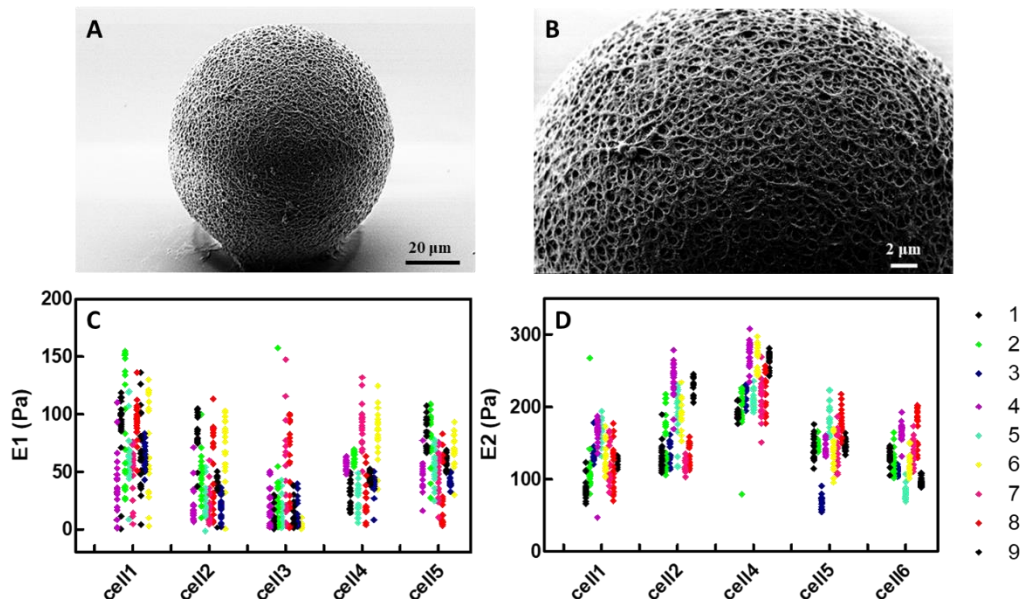


Figure 75: (A,B) SEM microphotographs of the oocyte highlighting the porous network of the ZP (C) E1 values distribution within the same cell is larger than value distribution on different cells and does not allow to appreciate position and cell heterogeneity; (D) E2 values distribution within the same cell is small enough that values distribution changes according to the probed area and the difference between the mean values of individual cells can be appreciated

For practical reasons linked to the specific experimental procedures used required to maintain a sufficient precision on the evaluation of the ageing time, the number of oocytes analysed for each set of measurement do not exceed 7-10 oocytes: therefore tens of oocytes extracted in excesses had to be discarded. To try to use also the excessed oocytes, increase the sample size and reduce at the same time the number of sacrificed animals, we investigated the effect of the freezing procedure on mice oocytes. The E1 and E2 values were evaluated for freshly retrieved oocytes and for oocytes subjected to a freeze-thaw procedure. As shown in Figure 76, the mean E1 and E2 values of thawed oocytes are respectively  $50 \pm 5$  and  $160 \pm 10$  and are not significantly different from those obtained for freshly retrieved oocytes respectively  $43 \pm 4$  and  $147 \pm 7$ , in agreement with what observed for human oocyte (Giolo, 2019).

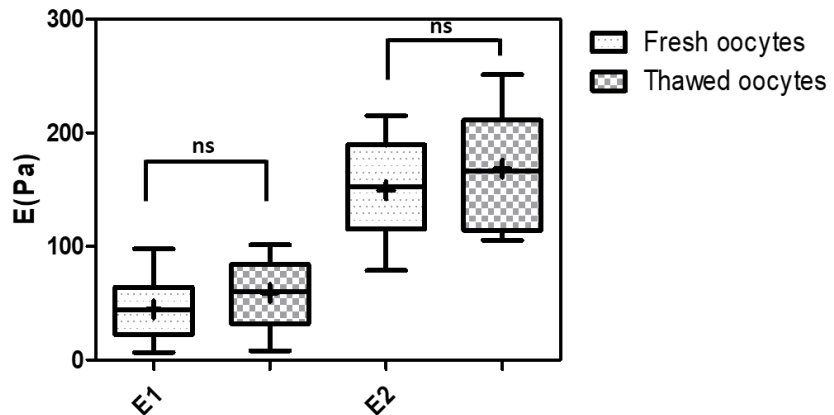


Figure 76: Comparable values of the distribution of E1 and E2 for fresh and thawed oocytes (6mice, N=20 for each condition) show that mechanical properties of ZP are not affected by freezing procedure. The values inside the box-whisker plots represent the first (25%) and third quartile (75%), the (-) indicate the maximum and minimum observations; the line within the box represents the median value (50%); while the mean value is indicated in the plot as (+); p value > 0.1

These data confirmed that the freeze/thaw procedure does not affect the mechanical properties of the oocyte. Therefore, freshly retrieved and thawed oocytes were not distinguished in the next experiments and data were used together to describe the postovulatory aging process.

### 5.3.2 Is post-ovulatory ageing affected by AFM indentation?

In order to rule out the possibility that the indentation measurements itself can impair the dynamics of the post-ovulatory ageing, we used cryo-conserved oocytes to investigate if there is a correlation

between degradation time and indentation force. Three groups of oocytes were mechanically stimulated at the beginning of the measurement by a single indentation with the bead-mounted cantilevers, for each group a different force loading was applied (1nN, 10nN and 20nN). Then the mean elapsed time between thawing and the onset of the visually-detected morphology change. No significant change in this time was observed and all the conditions tested were similar to the control group, in which no force was applied (Figure 77).

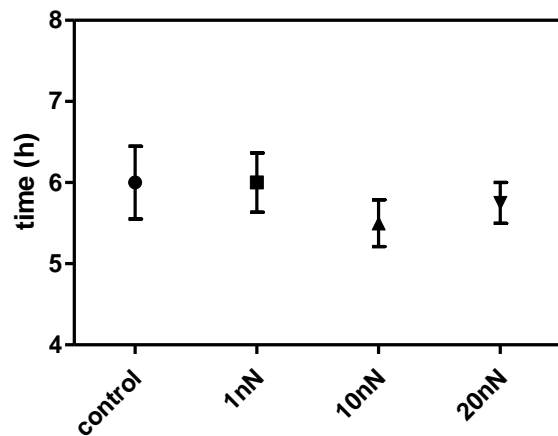


Figure 77: Mean values and standard deviations (SD) of the post-ovulatory oocyte lifespan in three groups of oocytes in which different force loading were applied (1nN, 10nN, 20nN), and the control group in which no force was applied (N=6, for each condition)

To better monitor in vitro the effect of the AFM indentation on the health and postovulatory evolution of freshly retrieved oocytes the correlation between CG exocytosis and force of AFM indentation was investigated. To this purpose the solution of FITC-LCA was added to the culture medium. Initially a background fluorescence can be observed everywhere; after the occurrence of spontaneous GC exocytosis the  $\alpha$ -mannose concentration in the PVS peaks, and so do the bound fluorophores, resulting in a weak, but detectable, local increase of the fluorescence.

Different forces were applied on the oocytes by AFM with a bead modified cantilever, as previously described: starting from the thawing time up to oocyte visible degradation, forces of 1nN, 10 nN and 20 nN were applied to three different oocytes groups with a single indentation at the beginning of the experiment. Epifluorescence images were taken every hour. Between measurements the oocytes

were kept at 37°C in the incubator (5% CO<sub>2</sub>) and extracted only for the time needed for image acquisition. Their morphology was monitored by bright field microscopy, considering healthy specific visual features such as the presence of a round-shaped ooplasm, a regular ZP and the presence of the PB. Oocyte degradation was identified when anomalous morphological features appeared such as increase of cytoplasm granulometry, a visual deformation of the ooplasm and the oolemma break down resulting in the disappearance of the perivitelline space (PVS) (Lim E. A., 2004).

Figure 78 A displays the merging of bright field and fluorescence images of the same oocyte at three different ageing times. To compare the ageing-related fluorescence variations of different oocytes, the occurrence of visual degradation was chosen as the time reference zero, to which data from different oocytes are backward aligned. As a result, the data acquired before the degradation are plotted on a negative timeline: the time before degradation.

The oocyte in vitro evolution as monitored by granules exocytosis, observed at different applied forces and in absence of the applied force is shown in Figure 78B. Approximately two hours before any visual morphological changes related to oocyte degradation, we observed that the CG-related fluorescence signal increased both in absence and in presence of applied forces, with a smooth broadening in time of the GC response when a force of 20 nN was applied. We concluded that applied forces of 10nN and below do not affect CG exocytosis and do not induce a premature in vitro oocyte ageing.

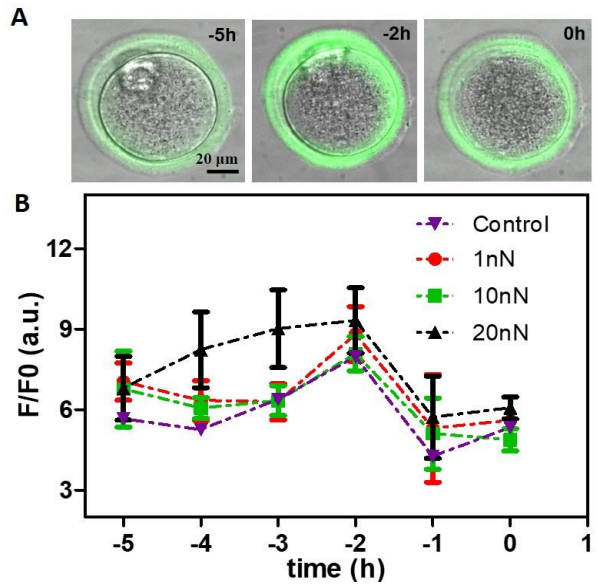


Figure 78: (A) Merged images of bright field and fluorescence show the variation of the oocyte morphology related to ageing and the increase in the intensity of the fluorescence related to the CG release about two hours before the occurrence of the visual degradation, (B) The change in the fluorescence related to CG exocytosis was monitored during in vitro post-ovulatory ageing for three groups of oocytes subjected to mechanical loading of 1nN, 10nN and 20nN (in red, green and black) and the control (in violet) where no forces were applied. To compare data from different oocytes, the values of the fluorescence intensity were aligned backward on the time scale starting from the time of visual degradation occurrence (the zero time) (N=6, for each condition)

On the base of our results we selected 1nN force for the postovulatory in vitro mechanical assay, to operate in a non-invasive condition, with a minimal stress for the oocyte.

### 5.3.3 The mechanical properties of the oocyte depend on the postovulatory aging

The post-ovulatory mechanical properties of both freshly retrieved and cryo-preserved oocytes were evaluated by AFM indentation measurements as a function of ageing time. Measurements were taken at one-hour intervals, while between two subsequent measurements, the oocytes were kept in incubator conditions and taken out for approximately only 10 minutes for each measurement.

According to their morphological features the oocytes were divided into two groups: those that maintained the “healthy morphology” 6 hours after the retrieval/thawing and those that during the experiment reached a visible state of degradation (Figure 79). Indeed, although the same procedures and the same experimental conditions were adopted for all the oocytes investigated, such as the age

of the mice, the time from the superovulatory injection and the retrieval surgical procedure, different MII oocytes showed significantly different degradation times.

The average values of E2 at every hour for the two oocyte groups are shown in Figure 79. As for the

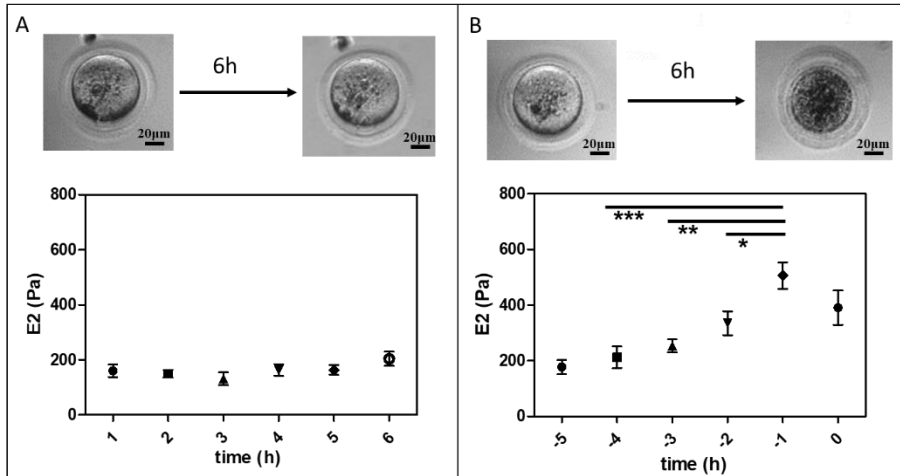


Figure 79: (A) Oocyte morphology and E2 variation during in vitro ageing for oocytes that did not reach degradation during the observation period (up to 6 hours from the retrieval/thawing). The variation is not significative ( $p > 0.05$ ). Time scale is numbered in hours from the retrieval ( $N=15$ ). (B) A healthy oocyte is characterized by a clear moderately granulate cytoplasm and a round-shaped ooplasm. Within 6 hours, oocyte degradation occurs. Visual features related to cell degradation are a brown cytoplasm and an indistinct plasma membrane. E2 variation is showed during in vitro ageing for oocytes that reached degradation during the observation period (up to 6 hours from the retrieval/thawing).. Data of each cell are aligned on the time of degradation and plotted backward against the time scale of the time before degradation. A significative increase in ZP stiffness is observed one hour before the visual degradation ( $N=20$ ). The significance level was set at  $*p < 0.01$ ,  $**p < 0.001$ , and  $***p < 0.0001$

data previously shown for the fluorescence, to compare the ageing-related stiffness variation of different oocytes, the data acquired before the degradation were plotted as “time before degradation” choosing the occurrence of visual degradation as the zero of the time scale. We first observed that for the oocytes that preserve healthy morphological feature no changes in stiffness can be detected (Figure 79A). On the other hand, the oocytes with features associated with a degraded status at the end of observation period showed significant stiffness variation before degradation (Figure 75B). Specifically, before any visual morphological change can be observed, a sudden increase of the E2 values occurred, followed by a lowering of the E2 value. In addition to the Young moduli values, the dissipated viscous energy was calculated. This allowed to estimate the viscous contribution during the compression process (Yun, 2017).

The dissipation energy and the E2 values plotted in Fig. 80 as function of the time from the thawing (A) and before degradation (B) show an opposite behaviour: one hour before the visual degradation the energy dissipated during indentation, showed a sudden decrease. These data together are consistent with the occurrence of a cross-linking of the ZP glycoproteins, similarly to the reaction that occurs in the egg after the fertilization.

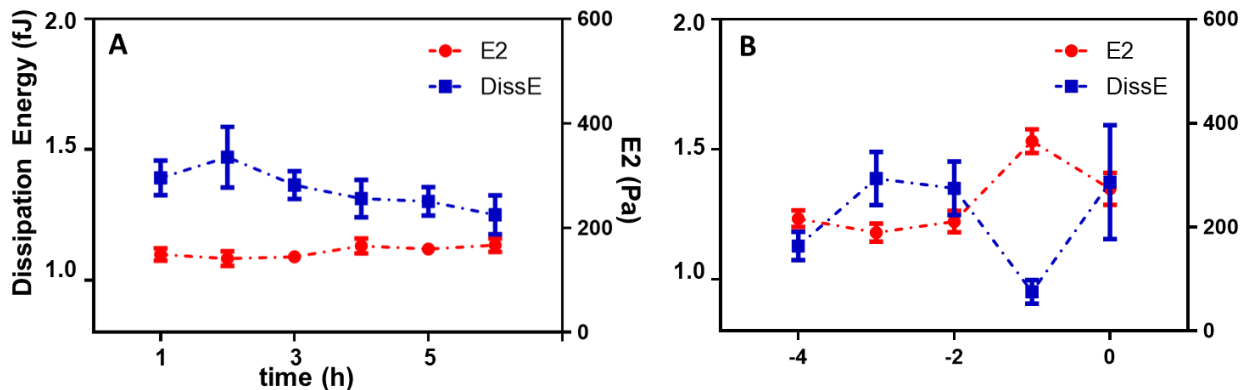


Figure 80: The trend of two parameters is shown during in-vitro ageing, while the stiffness (represented by the variation of E2 in red) increases, the dissipation viscous energy (in blu in the plot) decreases and vice-versa. (N=20), (A) for oocytes that did not reach degradation during the observation period, (B) for oocytes that reached degradation during the observation period

### 5.3.4 The mechanical properties of the oocyte during the postovulatory aging do not depend on the measurement approach.

To further confirm that the observed effects do not depend on the specific measurement approach adopted, but rather reflect the actual status of the whole oocytes, we performed whole oocytes stress relaxation measurement (Figure 81, A, B). As depicted in Figure 81 B, stress relaxation tests the decrease in time of the force that the sample opposes to an external strain.

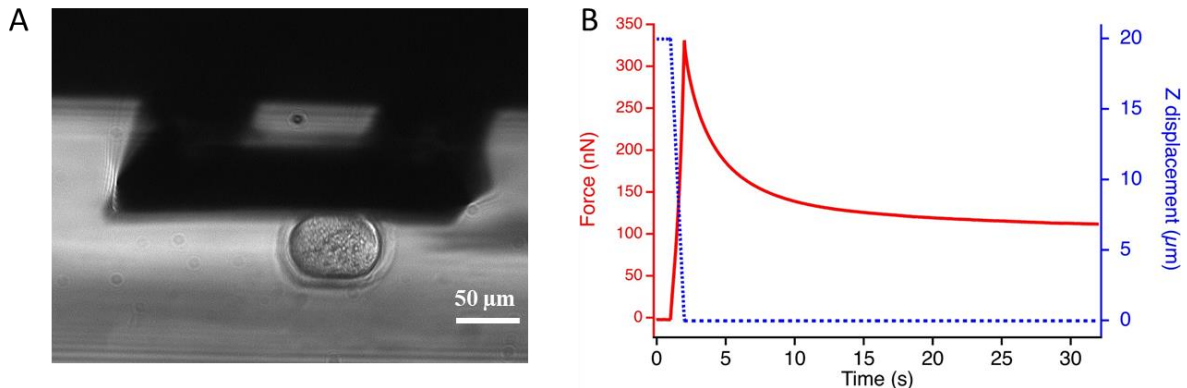


Figure 81: (A) side-view of the oocyte compressed by the macro-probe, (B) stress-relaxation measurement of an oocyte, in which a deformation of  $20\mu\text{m}$  is applied for 30 sec (displacement is depicted in blue). During this time the force exerted by the cell on the probe could be measured (in red)

The velocity of this change is expressed by the relaxation time( $\tau$ ) that depends on the ratio between the sample viscosity ( $\eta$ ) and sample stiffness (E) and is expressed by the equation:  $\tau = \eta/E$ . We observed that the stress relaxation curve should be described by at least two Maxwell elements in series, each with a different time relaxation constant:  $\tau_1$  and  $\tau_2$ .

The lower the viscosity and the stiffer the sample, the faster is the relaxation process. According to the local indentation data discussed in the previous paragraph, if reported to the whole cell, we would expect to observe the halving of the relaxation time one hour before the degradation. Therefore, we performed whole cell relaxation measurements of 5 oocytes at different time from retrieval, using the macro-cantilevers previously described.

The distribution of the values of these two parameters mediated for different cells is depicted in Figure 82 A, for each cell 12-15 curves were acquired. As we can observe,  $\tau_2$  is significantly higher than  $\tau_1$ . Moreover, the distribution in time of the values (shown in Figure 82 B) highlights a decrease in time of  $\tau_1$ .

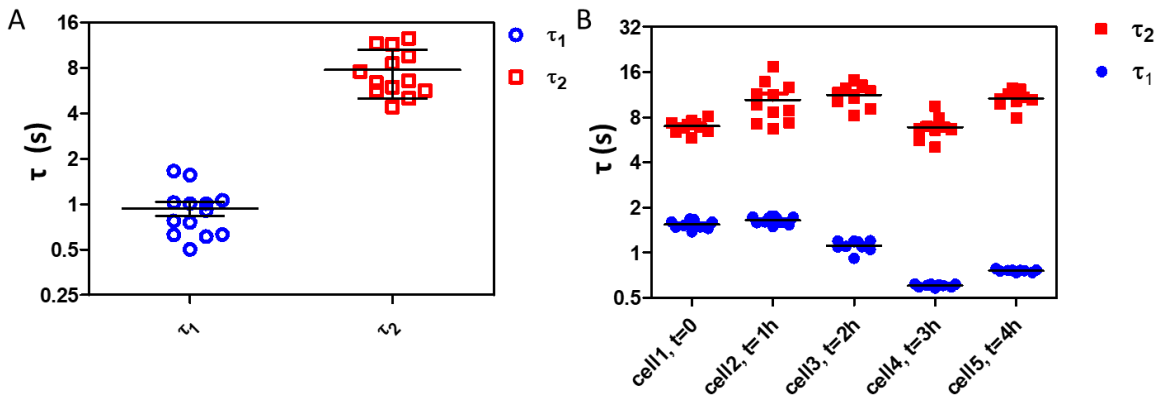


Figure 82: (A) Relaxation time ( $\tau_1$  and  $\tau_2$ ) mediated for 5 oocytes are shown,  $\tau_2$  (in red) being consistently higher than  $\tau_1$  (in blue), (B) the variation in time during oocyte post-ovulatory ageing of these two parameters for 5 cells. Each point here corresponds to a single measure

Since, as a contrary to indentation measurements, stress relaxation performed with larger indenters probes also the mechanical properties of the internal layers of the oocytes (Shen, 2019), it is reasonable to assume that the two time constants are related to either the ooplasm or the ZP, but the proper assignment is not trivial. To help in this task, we measured the Young modulus of the bare Ooplasm, mechanically deprived by the ZP. The same oocyte was measured by AFM-indentation before and after the ZP removal. The dissipated viscous energy was also calculated and the mean values for these different oocyte compartments is shown in Figure 83, where two force-distance curves are also shown.

The difference between the two slopes is reflected by the distribution of the Young moduli: E2 is significantly higher for the ZP-surrounded oocytes (ZP-Oo) than for the Ooplasm (Oo) ( $280 \pm 80$  and  $90 \pm 30$ , respectively). At the same time, the energy dissipation is much lower on ZP-Oo than on Oo, indicating that the ooplasm is a more viscous and softer structure.

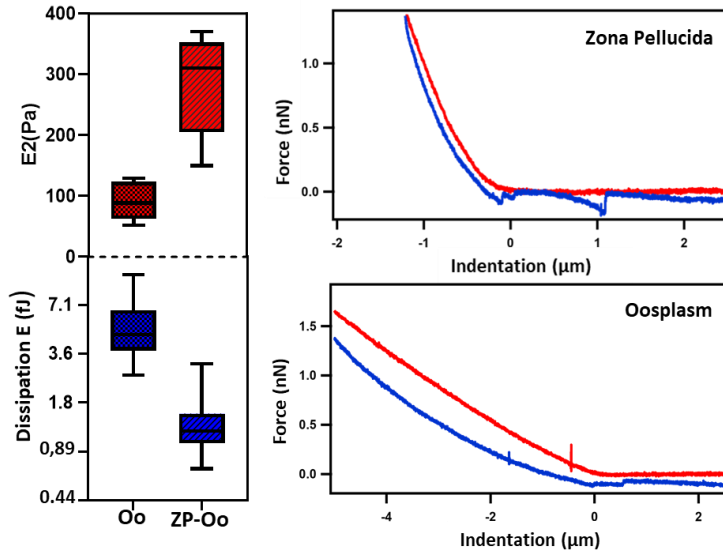


Figure 83: mechanical characterization of Ooplasm (Oo) and oocytes surrounded by ZP (ZP-Oo), ooplasm is characterized by an higher dissipation energy (in blu) and a significantly lower stiffness (in red) compared to ZP, as is highlighted by the force-distance curves shown on the right

Following these observations, we decided to assign the faster relaxation time  $\tau_1$ , to ZP and  $\tau_2$  to the ooplasm, that relaxes over a longer time interval.

With this assignment the decrease in time of  $\tau_1$  three hours after the retrieval reproduces what we previously observed with AFM-indentation: during post-ovulatory ageing, ZP becomes stiffer and the viscosity decreases, consistently with the occurrence of a cross-link of this layer. In conclusion we confirm that the evolution of the mechanical properties of the oocytes can be used as an indicator of post ovulatory ageing and that they can be evaluated alternatively by measuring the Young modulus performing AFM-based local indentation or by measuring the relaxation time by whole oocyte stress relaxation investigation, with equivalent significance. Alternatives approaches between those described in Chapter 2 can also be adopted in order to develop a commercial oocyte sorter based on mechanical properties; however, the design and realization of such instrument is beyond the scope of this thesis work and will be addressed by our laboratory in a separate study.

### 5.3.5 The mechanical properties of the oocytes depend on the release of the GC

In order to understand whether a release of GC was involved in the observed increase in stiffness, we repeated the AFM indentation measurements in combination with epifluorescence microscopy to monitor GC exocytosis during in vitro oocyte ageing. In Figure 84 A we display the epifluorescence image of the same oocyte at three different ageing times, while fluorescence intensity and the E2 values recorded at 1-hour intervals until oocyte degradation are shown in Fig. 84 B. An increment in the fluorescence intensity was detected about 1 hour before the variation of E2.

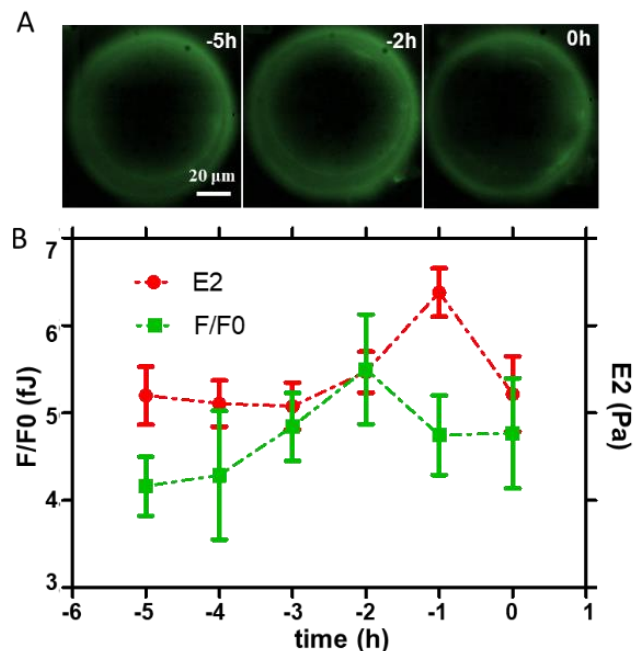


Figure 84: (A) the variation of the fluorescence intensity CG related is shown at three different times before the occurrence of the visual degradation; (B) the same cells ( $N=25$ ) were probed for the FITC-LCA intensity signal (in green) and the E2 variation in time (in red), the results show a progressive increase in the stiffness of the aged oocyte that is anticipated by an increase in the fluorescence related to the CG release.

These data suggest that the ZP stiffening in the oocyte just before degradation may be caused by the CG exocytosis which happens naturally anticipating by roughly one hour the observed ageing-induced zona hardening.

### **5.3.6 ZP Stiffness variation in parthenogenetically activated oocytes**

In order to further understand if there is a direct correlation between CG exocytosis and ZP mechanical properties, we chemically induced the CG exocytosis adding to the medium a well-known parthenogenetic activator, SrCl<sub>2</sub>. The main effect of SrCl<sub>2</sub> is the Ca<sup>2+</sup> release from the internal compartments of the cell. Ca<sup>2+</sup> oscillations involve the activation of the meiotic resumption and eventually the formation of the two pronuclei of the parthenogenetic embryo. This chemical activator has been already proved also to elicit the cortical granule reaction in the MII oocyte (Cappa A. I., 2018).

After the incubation with the fluorophore, oocytes were activated with 30mM of SrCl<sub>2</sub> and the change in the mechanical properties as well as the variation in the FITC-LCA fluorescence intensity were continuously recorded for up to 90 minutes. Few minutes after the addition of the activator, CG exocytosis was detected by a sudden increase of the fluorescence signal, which reached the maximum intensity within 30 minutes and then gradually decreased. This behaviour was consistently observed on all the oocytes investigated. On the contrary, although the activator had a clear influence on the ZP stiffness, it was impossible to identify a general behaviour. The activator determined strong oscillation on the stiffness with times, frequency and intensity strongly dependent on the oocyte investigated, which made impossible to extract a common trend (Fig.85 A-E). On the contrary, the negative control, in the absence of the activator, did not show significant oscillations, neither in the fluorescence intensity nor in the E2 values, but only a monotonic slow decrease, in the 80 minutes of time interval monitored during the experiment (Fig. 85 F). One of the reasons of the observed oscillation in E2 values could be linked to the fact that the GC release stimulated in this way is higher in some specific location of the oolemma; as a consequence also the ZP hardening could vary significantly depending on the position and the measurement approach adopted does not allow to select the measurement point where the exocytosis effect is maximum. A more precise evaluation of the fluorescence limited to the indentation area could allow to solve this problem.

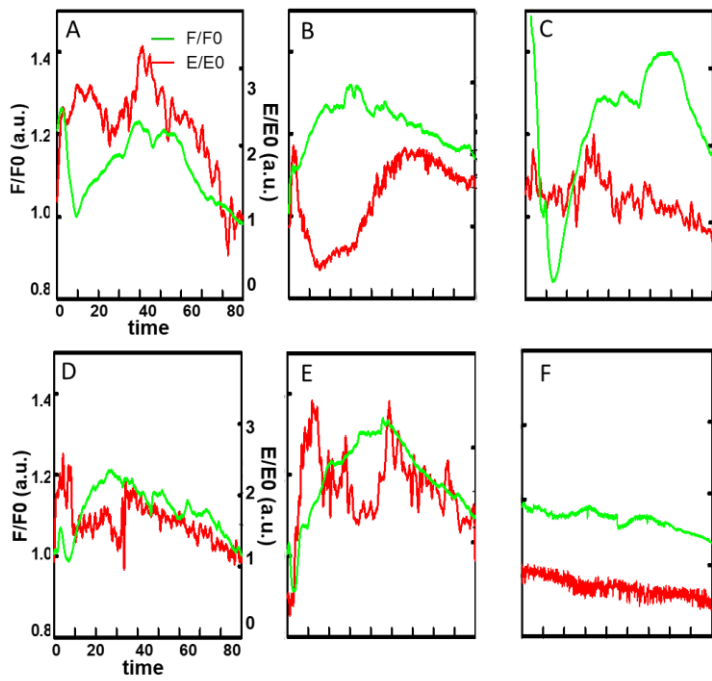


Figure 85 After addition of the  $\text{SrCl}_2$  the intensity of the fluorescent signal related to the CG exocytosis (in green) rapidly increases reaching the maximum intensity after 30-40 min, then progressively decreases; also the second Young modulus (in red) undergoes an increase after the addition of the activator, but the dynamics of this variation are different in 5 different cells (A-E); Negative control: much smoother and less important variations are recorded both in fluorescence and in stiffness in absence of chemical activation (F). All Data are normalized to the first value which corresponds to the  $\text{SrCl}_2$  addition.

### 5.3.7 ZP stiffening in the aged oocytes correlates with a decrease in the IVF yields

In order to investigate how the observed ZP stiffening affects the ability of oocytes to be fertilized, IVF was performed and the yield of embryo development was evaluated after 24h (2-cell embryo stage), and after 102h (blastocyst stage). Two groups of 6 oocytes were measured by AFM-indentation 1h and 6h after thawing. The values of  $E_2$  and of the dissipation viscous energy are shown in Figure 86, in which the mean values and SD are also depicted. After 6h, two out of six of the oocytes showed a significative increase of  $E_2$ , indicating that they were probably close to degradation and potentially infertile. Unfortunately, with the current experimental set-up it was impossible to track the oocyte and associate the yield of fertilization to each individual oocyte. Obviously, giving the stochastic character of oocyte ageing, each group can be described as

composed by an heterogeneous population and performing a statistical analysis does not provide useful information: indeed, no statistically significative increase can be detected between the two groups, even if a trend consisting in the increase of E2 and the decrease in the dissipation viscous energy is highlighted. In Figure 86 A, an oocyte in the fertilization drop, surrounded by the sperm cells is shown. The other images show a 2-cell embryo (Figure 86, B), an apoptotic fragmented oocyte (Figure 86, C) and an early blastocyst stage (Figure 86, D). When considering the yields of the 2-cell embryos, we noticed a significative decrease in the 6h aged sample: in the group “freshly thawed” oocytes 4 out of 6 developed into a 2 cell-embryo, while in the “aged” group only one oocyte succeeded in reaching this stage. At the same time the amount of fragmented apoptotic oocytes increased in this sample, from 0 to 2 out of 6. When looking at the development of the blastocyst, 3 oocytes out of 6 arrived at this stage in the first sample, while in the 6h aged sample no blastocyst was observed. The results are summarized in table 2.

Time elapsed from thawing	N total	N 2-cell	N ooplasm fragmentation	N blastocyst	Stiffness (E)
3h	6	4	0	3	218+/-70 Pa
8h	6	1	2	0	306+/-160 Pa

Table 2: Yields of IVF and mechanical properties of two groups of oocytes after 3 and 8 hours from the thawing.

At this stage it is impossible to extract from the clear correlation between ageing and fertilization yield, a correlation between ZP stiffening, as an anticipation of oocyte degradation. Further experiments with identifiable oocytes need to be performed.

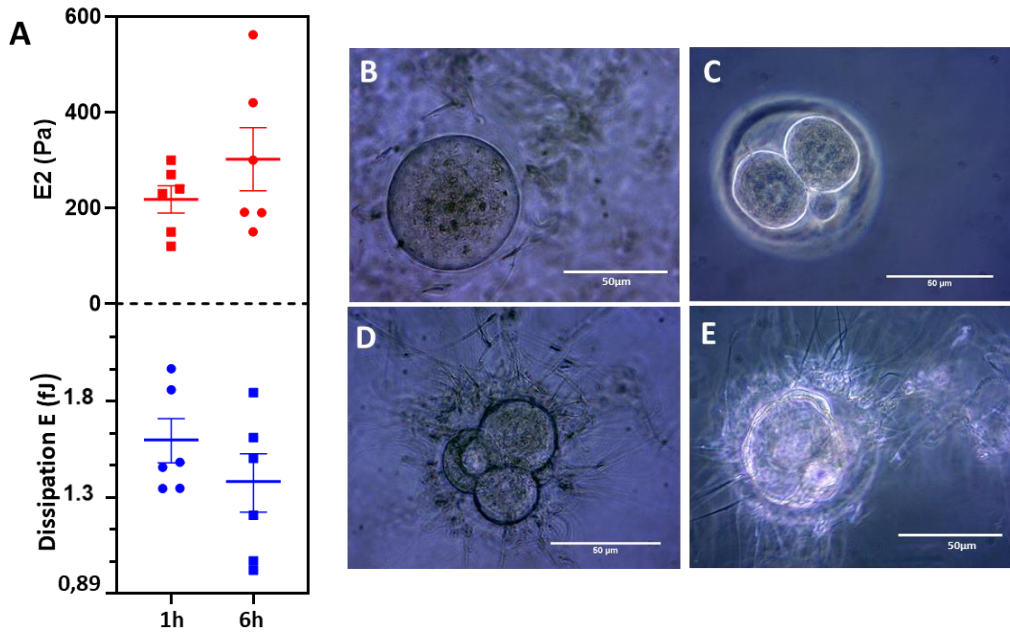


Figura 86: (A) The variation in Dissipation energy (in blu) and E2 (in red) for two groups of 6 oocytes 1h after thawing and 6 h later. Only for few of them it was possible to observe a change in the mechanical parameters in the aged sample, (B) optical image of oocyte in the fertilization drop, (C) 2-cell embryo, (D) fragmented apoptotic oocyte, (E) early blastocyst

## 5.4 Conclusions

In this work, the mechanical properties of oocytes are investigated during post-ovulatory ageing, one of the processes responsible for the decreased yields of in vitro fertilization. The mammalian oocytes are surrounded by the zona pellucida (ZP), a glycoproteic membrane whose mechanical properties change consistently during the oocyte maturation and after the occurrence of the fertilization, resulting in an increase in the stiffness of this layer.

Here, by AFM-indentation measurements, an increase in the ZP stiffness (expressed by the Young's modulus) of the aged oocytes was observed 1-2 hours before any morphological change due to apoptosis.

This is complemented by a decrease in the viscosity of this layer evaluated through the analysis of dissipation viscous energy that prompts us to postulate the occurrence of a cross-linking reaction in this layer. We found out two mechanical parameters that we can relate to the ageing status of the oocyte before the change in any visual feature due to degradation. By stress-relaxation measurements with a fabricated macro-probe, it was possible to distinguish between the mechanical properties of the ooplasm and the zona pellucida, by the analysis of two relaxation time ( $\tau_1$  and  $\tau_2$ ). By separately measuring the mechanical properties of oocyte with and without ZP, we found out that these cell compartments have different mechanical properties: while the ooplasm is a viscous and softer structure, ZP is less viscous and stiffer.

In this way, we were able to assign  $\tau_1$  and  $\tau_2$  to ZP and the ooplasm, respectively. At the same time, these results confirm what we previously showed with indentation measurements:  $\tau_1$  that is a measure of the ratio between the ZP viscosity and elasticity decreases in time during the post-ovulatory ageing. Then, to understand the origin of the observed phenomenon, epifluorescence measurements to detect the release in time of the cortical granules (CG) were performed, simultaneously to the indentation measurements. In this way the occurrence of a CG exocytosis in the aged oocyte temporally related to the change in the mechanical properties of the ZP was demonstrated, even

though the molecular mechanism involved in the ZP cross-linking still remains to be investigated. By inducing the CG release by a parthenogenetic activator and simultaneously detecting the change in the cell mechanical properties, we tried to further confirm the cause-effect relation between these two events. An increase in the stiffness of the ZP after the CG release was observed in all the oocytes tested, but the dynamics of this process changed according to the oocyte considered.

To prove that indentation measurements did not affect the cell viability inducing a premature ageing of the oocytes, the possibility to trigger the CG release with the application of different forces was also investigated. The dynamics of this mechanism do not change in the range of the force loading applied (up to 20nN), allowing to prove that the mechanical measurement does not interfere with the ageing progression. Moreover, two groups of oocytes (“freshly thawed” and “aged” oocytes) were measured by AFM-indentation and then subjected to the IVF procedure, providing a first hint between the yields of embryo development and the oocyte mechanical parameters: the “aged” oocytes, in which the stiffness significantly increased, did not develop into embryos. At the same time, for the oocytes in which the measured stiffness was lower, the number of embryos was higher, allowing to prove that the mechanical measurements do not interfere with the embryo viability and the yields of IVF.



## General conclusions

The potential of the investigation of cellular mechanical properties as an effective indicator for the evaluation of the cell physiological state has emerged as a hot topic in the last decade as well as the development of new diagnostic tools based on the use of a sensitive technique able to detect small changes in the mechanical response of the cells. In this framework, this thesis work addresses the importance of cellular mechanics in three biomedical fields which are of dramatic relevance in human health: the cancer progression, the cardiovascular microcirculation diseases and the assistive reproductive techniques (ART) that are intended to solve the problems of male and female infertility.

In the first example, the role of T $\beta$ 4, a small polypeptide that modulates actin polymerization by sequestering G-actin, was investigated in different melanoma cell lines expressing higher or lower levels of this factor. The clonogenic and tumorigenic potential was increased in the cells with higher levels of this polypeptide even though the stemness markers, that are normally associated with a mesenchymal phenotype, were not homogeneously increased. Nevertheless, the levels of T $\beta$ 4 affected the cytoskeletal organization resulting in a subsequent change of the cell mechanical properties. Lower levels of this polypeptide changed the location of intermediate filaments across the cell body resulting in the concentration around the nucleus of Vimentin and Nestin, increased the number of actin stress fibers and the number and the morphology of focal adhesions to allow a better cell spreading. All these morphological changes resulted in an increased cell stiffness, evaluated through AFM-indentation, compared to the cell lines with an higher level of T $\beta$ 4, that were characterized by a lower stiffness, a less organized distribution of intermediate filaments across the cell body and a decrease in the number and density of actin stress fibers. The changes in the mechanical phenotype of more invasive cell lines with increased levels of T $\beta$ 4 could be exploited for the detection of these cells in a tumorigenic population, and T $\beta$ 4 evaluated as a potential therapeutic target. Nevertheless, the phenotypic heterogeneity due to the “noise in gene expression” of these cells

did not allow to establish a precise relation between the biomechanical properties and the stemness level.

In the second example, a different topic in mechanobiology, namely mechanotransduction, and more precisely the capability of all the cells to adapt their mechanics to the environmental condition was investigated on the effect of a heart failure on cardiac pericytes. These cells are localized around the capillaries where exert important functions such as the blood flow regulation, and the recruitment and stabilization of endothelial cells in neovascularization processes. It has been recently found that pericytes administration promote angiogenesis in hibernated hearts after myocardial infarction. As this effect has been linked to their mechanotransduction properties, the impairment of these mechanisms in pericytes recovered from patients affected by end-stage heart failure (E-Pc) was evaluated, compared to the one coming from healthy patients (D-Pc). The pericytes responsiveness to different substrate coating and substrate stiffness was evaluated. As expected, the modulation of cell mechanical properties of E-Pc on hard substrates was impaired, while D-Pc exhibited an increase in the stiffness that was accompanied by an increase in YAP nuclear translocation, a co-transcriptional activator that is shuttled to the nucleus in response to mechanical stimuli. On the contrary, YAP nuclear traslocation was impaired in E-Pc. The other molecular pathways involved in TAP/TAZ signalling were investigated to look for the possibility to find a therapeutic target able to revert the YAP nuclear translocation. Interestingly, an upregulation of MEK/ERK pathway was found in E-Pc. MEK is a transcription factor involved in YAP degradation and when these cells were treated with a MEK inhibitor, the level of nuclear YAP was restored, suggesting that modulation of upstream regulators of YAP pathway could be evaluated as a way to reverse Pc dysfunction and contrast CMD in heart failure.

In the third example, that represents the core of the experimental activity performed during my PhD, the mechanical properties of oocytes have been identified as a scoring system to evaluate the quality of oocytes to be selected for the practice of the *in vitro* fertilization. Here the mechanical properties,

beside their application for diagnosis and therapy, revealed to be also useful for the active selection of the competent cells, thus adding a further value to the mechanobiology approach. In particular I investigated the evolution of the oocyte stiffness and viscosity during post-ovulatory ageing, one of the processes responsible for the decreased yields of in vitro fertilization. More in detail, an increase in the stiffness of the zona pellucida (ZP), a glycoproteic membrane that surrounds the oocyte, detected by AFM-indentation was observed before any morphological change due to apoptosis, and allowed to introduce a novel classification for pre-apoptotic and non-fertile oocytes.

This was confirmed by a decrease in the viscosity of this layer that is in accordance with the postulated occurrence of a cross-linking reaction. Here, two mechanical parameters were found, able to predict ageing status of the oocytes before any visual feature due to degradation. By stress-relaxation measurements with a fabricated macro-probe, it was possible to distinguish between the mechanical properties of the ooplasm and the zona pellucida, by the analysis of two relaxation time ( $\tau_1$  and  $\tau_2$ ). By separately measuring the mechanical properties of oocyte with and without ZP, we were able to assign  $\tau_1$  and  $\tau_2$  to ZP and the ooplasm, respectively. At the same time, these results confirm what previously shown with indentation measurements:  $\tau_1$  that is a measure of the ratio between the ZP viscosity and elasticity decreases in time during the post-ovulatory ageing. Then, epifluorescence measurements to monitor the release in time of the cortical granules (CG) were performed, simultaneously to the indentation measurements. The occurrence of a CG exocytosis in the aged oocyte temporally related to the change in the mechanical properties of the ZP was demonstrated. Finally, oocytes measured by AFM-indentation were subjected to IVF procedure. The “aged” oocytes, in which the stiffness significantly increased, did not develop into embryos. At the same time, for the oocytes in which the measured stiffness was lower, the number of embryos was higher, allowing to prove that the mechanical measurements do not interfere with the embryo viability and the fertilization yields and at the same time demonstrating that oocyte mechanical properties could be employed for the selection of the oocytes for IVF practice.

These three examples together consolidated the accepted paradigm that links mechanical properties to the physiological state of the cells, and could be employed for the study of complex pathologies for their detection, for the identification of a possible therapeutic target and for the selection of the cellular targets. Moreover, my experience confirms that the mechanobiological approach is universal, in the meaning that it is not specific to a single type of cell, organ or disease, rather can find application in nearly any field of biology and medicine. Moreover, one of the main relevant aspects is related to the non-invasiveness of the mechanobiological approach that could allow to select the sample of interest without any damage or degradation that often characterize many of the biomedical procedures based on molecular targeting by specific markers or time-consuming destructive methods. The development of devices based on this technology that can bring this powerful biomechanical tool to the clinics is therefore advisable.

## References

- Andolfi, L. B. (2014). Investigation of Adhesion and Mechanical Properties of Human Glioma Cells by Single Cell Force Spectroscopy and Atomic Force Microscopy. *PLoS ONE*.
- Andolfi, L. B. (2021). Scanning Probe Microscopies: Imaging and Biomechanics in Reproductive Medicine Research. *Int. J. Mol. Sci.*
- Andolfi, L. M. (2016). Investigation of the mechanical properties of zona pellucida of whole human oocytes by atomic force spectroscopy. *Int. Biol.*
- Aragona, M. P. (2013). A mechanical checkpoint controls multicellular growth through YAP/TAZ regulation by actin-processing factors. *Cell*, 1047-1059.
- Arbore, C. P. (2019). Probing force in living cells with optical tweezers: from single-molecule mechanics to cell mechanotransduction. *Biophysical Reviews*.
- Assou, S. H. (2010). Human cumulus cells as biomarkers for embryo and pregnancy outcomes. *Molecular Human Reproduction*, 531-538.
- Attwell, D. M. (2016). What is a pericyte? *J. Cereb. Blood Flow Metab.*, 451-455.
- Avella, M. A. (2014). A single domain of the ZP2 zona pellucida protein mediate gamete recognition in mice and humans. *J. Cell Biol.*, 801-809.
- Avolio, E. M.-A. (2015). Combined intramyocardial delivery of human pericytes and cardiac stem cells additively improves the healing of mouse infarcted hearts through stimulation of vascular and muscular repair. *Circ. Res.*
- Baibakov, B. G. (2007). Sperm binding to the zona pellucida is not sufficient to induce acrosome exocytosis. *Development*, 933-943.
- Basoli, F. G. (2018). Biomechanical Characterization at the Cell scale: Present and Prospects. *Frontiers in physiology*.

- Bernal, A. A. (2018). Nestin-expressing progenitor cells: Function, identity and therapeutic implications. *Cel. Mol. Life Sci.*, 2177-2195.
- Bird, J. L. (2000). Exercise-induced changes in proteoglycan metabolism of equine articular cartilage. *Equine Vet. J.*, 161-163.
- Birukov, K. G. (2009). Small GTPases in mechanosensitive regulation of endothelial barrier. *Microvascular Research*, 46-52.
- Bonny, A. F.-S. (2021). Orthogonal control of mean and variability of endogenous genes in a human cell line. *Nat. Commun.*, 1-9.
- Borowicz, S. V. (2014). The Soft Agar Colony Formation Assay. *J. Vis. Exp.*
- Burkart, A. D.-M. (2012). Ovastacin, a cortical granule protease, cleaves ZP2 in the zona pellucida to prevent polyspermy. *Journal of cell biology*, 37-44.
- Butcher, D. A. (2009). A tense situation: forcing tumour progression. *Nature Reviews Cancer*, 108-122.
- Butcher, D. T. (2009). A tense situation: forcing tumour progression. *Nature Reviews Cancer*, 108-122.
- Butt, H.-J. C. (2005). Force measurements with the atomic force microscope: Technique, interpretation and applications. *Surface Science Reports*, 1-152.
- Capp, J. P. (2012). Stochastic gene expression stabilization as a new therapeutic strategy for cancer. *BioEssays*, 170-173.
- Cappa, A. I. (2018). Live imaging of cortical granule exocytosis reveals that in vitro matured mouse oocytes are not fully competent to secrete their content. *Biology Open*.
- Cappa, A. I. (2018). Live imaging of cortical granule exocytosis reveals that in vitro matured mouse oocytes are not fully competent to secrete their content. *Biology Open*.
- Cárdenas-Pérez, S. C.-P.-M.-V.-V. (2018). Recent advances in atomic force microscopy for assessing the nanomechanical properties of food materials. *Trends in Food Science & Technology*.

- Cattin, C. J.-M. (2015). Mechanical control of mitotic progression in single animal cells. *PNAS*.
- Chen, C. W. (2013). Human pricytes for hischemic heart repair. *Stem Cells*, 305-316.
- Chen, J. (2014). Nanobiomechanics of living cells: a review. *Interface Focus*.
- Chermuła, B. K.-T. (2020). Human Cumulus Cells in Long-Term In Vitro Culture Reflect Differential Expression Profile of Genes Responsible for Planned Cell Death and Aging—A Study of New Molecular Markers. *Cells*.
- Chintalgattu, V. R. (2013). Coronaty microvascular pricytes are the cellular target of Sunitinib malate-induced cardiotoxicity. *Sci. Trans. Med.*
- Chtcheglova, L. (2004). *Quasistatic and dynamic force microscopy of single antigen-antibody complexes and fibrin-fibrinogen systems*. Lausanne, EPFL.
- Colin-York, H. F. (2018). The future of traction force microscopy. *Current Opinion in Biomedical Engineering*, 1-5.
- Coy, P. G. (2008). Hardening of the zona pellucida of unfertilized eggs can reduce polyspermic fertilization in the pig and cow. *Reproduction*, 19-27.
- Crespo, P. C. (2016). The Chick Embryo Chorioallantoic Membrane as an in vivo Model to Study Metastasis. *Bio-protocol*.
- Croft, D. R. (2004). Conditional ROCK activation induces tumour cell dissemination and angiogenesis. *Cancer Res.*, 8994-9001.
- Dalby, M. J. (2004). Investigating the limits of filopodial sensing: a brief report using SEM to image the interaction between 10 nm high nano-topography and fibroblast filopodia. *Cell Biol. Int.*, 229-236.
- Dang, C. (2012). MYC on the Path to Cancer. *Cell*, 22-35.
- Ducibella, T. D. (1990). Changes in the Distribution of Mouse Oocyte Cortical Granules and Abilityto Undergo the Cortical Reaction during Gonadotropin-stimulated Meiotic Maturation and Aging in Vivo. *Biology of Reproduction*, 870-876.

- Dufrêne, Y. F.-M. (2017). Imaging modes of atomic force microscopy for application in molecular and cell biology. *Nature Nanotechnology*.
- Durham, J. T. (2014). Pericytes contractility controls endothelial cell cycle progression and sprouting insights into angiogenic switch mechanics. *Am. J. Phys. Cell Phys.*
- Ellis, P. F. (2004). A Persistent Marker for Multipotential Neural Stem Cells Derived from Embryonic Stem Cells, the Embryo or the Adult. *Dev. Neurosci.*, 148-165.
- Engler, A. S. (2006). Matrix elasticity directs stem cell lineage specification. *Cell*, 677-689.
- Fan, Y.-L. Z.-C.-L.-Q. (2019). Mechanical Roles of F-Actin in the Differentiation of Stem Cells: A Review. *ACS Biomater. Sci. Eng.*, 3788-3801.
- Fang, D. N. (2005). A tumorigenic subpopulation with stem cell properties in melanomas. *Cancer Res.*, 9328-9337.
- Fang, D. N. (2005). A tumorigenic subpopulation with stem cell properties in melanomas. *Cancer Res.*, 9328-9337.
- Fernández, P. H. (2007). Shear rheology of a cell monolayer. *New Journal of physics*.
- Fissore, R. A. (2002). Mechanisms underlying oocyte activation and postovulatory ageing. *Reproduction*, 745-754.
- Foster, C. T. (2017). Mutual dependence of the MRTF-SRF and YAP-TEAD pathways in cancer associated fibroblasts is directed and mediated by cytoskeletal dynamics. *Genes Dev.*, 2361-2375.
- Fraser, D. K. (2009). A chance at survival: Gene expression noise and phenotypic diversification strategies. *Mol. Microbiol.*, 1333-1340.
- Freitas, Z. R. (2004). Melanoma heterogeneity: Differential, invasive, metastatic properties and profiles of cathepsin B, D and L activities in subclones of the B16F10-NEX2 cell line. *Melanoma Res.*, 333-344.
- Friedrichs, J. L. (2013). A practical guide to quantify cell adhesion using single-cell force spectroscopy. *Methods*, 169-178.

Friedrichs, J. L. (2013). A practical guide to quantify cell adhesion using single-cell force spectroscopy. *Methods*, 169-178.

Fu, X. L. (2018). The Rules and Functions of Nucleocytoplasmic Shutting Proteins. *Int. J. Mol. Sci.*

Fusco, S. P. (2015). Crosstalk between focal adhesions and material mechanical properties governs cell mechanics and functions. *Acta Biomaterialia*, 63-71.

Gabrielsen, A. L. (2001). The impact of zona pellucida thickness variation of human embryos on pregnancy outcome in relation to suboptimal embryo development. A prospective randomized controlled study. *Human reproduction*, 2166-2170.

Garcia, R. a. (2012). The emergence of multifrequency force microscopy. *Nature Nanotechnology*.

Gates, R. S. (2007). Precise atomic force microscope cantilever spring constant calibration using a reference cantilever array. *Rev. Sci. Instrum.*

Gaub, B. M. (2017). Mechanical Stimulation of Piezo1 Receptors Depends on Extracellular Matrix Proteins and Directionality of Force. *Nano Letters*, 2064-2072.

Giolo, E. M. (2019). Study of mechanical properties of fresh and cryopreserved individual human oocytes. *European Biophysical Journal*, 585-592.

Goldstein, A. H. (2005). Thymosin beta: Actin-sequestering protein moonlights to repair injured tissues. *Trends Mol. Med.*, 421-429.

Gonzàlez-Bermùdez, B. G. (2019). Advances in Micropipette Aspiration: Applications in Cell Biomechanics, Models, and Extended Studies. *Biophysical Journal*, 587-594.

Guck, J. A. (2000). Optical deformability of soft biological dielectrics. *Physical reviews letters*, 5451-5454.

Guck, J. S. (2005). Optical Deformability as an Inherent Cell Marker for Testing Malignant Transformation and Metastatic Competence. *Biophysical Journal*, 3689-3698.

Guimaraes-Camboa, N. C.-M. (2017). Pericytes of multiple organs do not behave as mesenchymal stem cells in vivo. *Cell Stem Cell*, 345-359.

Gupta, M. K. (2015). Micropillar substrates: a tool for studying cell mechanobiology. *Biophys. Methods Cell Biol.*, 289-308.

Hadjimichael, C. C. (2015). Common stemness regulators of embryonic and cancer stem cells. *World J. Stem. Cells*, 1150-1184.

Han, M. P. (2011). Lower growth factor expression in follicular fluid undergone in-vitro fertilization. *Clinical and experimental reproductive medicine*, 210-215.

Hang, X. H. (2021). Nanosensors for single cell mechanical interrogation. *Biosensors and Bioelectronics*.

Hasegawa, A. M. (2014). Microdroplet In Vitro Fertilization Can Reduce the Number of Spermatozoa Necessary for Fertilizing Oocytes. *J. Reprod. Dev.*, 187-193.

Haugh, M. V. (2015). The role of integrin alpha (V) beta in osteocyte mechanotrasduction. *J. Mech. Behav. Biomed. Mater.*, 67-75.

Ho, H.-C. S. (2001). Hyperactivation of mammalian spermatozoa: function and regulation. *Reproduction*, 519-526.

Hoh, J. H. (1994). *J. Cell Sci.*, 1105-1114.

Holscher, H. (2008). Theory of phase-modulation atomic force microscopy with constant oscillation amplitude. *Journal of applied physics*.

Hotulainen, P. a. (2006). Stress fibers are generated by two distinct actin assembly mechanisms in motile cells. *J. Cell Biol.*, 383-394.

Hsu, C. Y. (2019). Comaprison of human issue microarray to human pericyte Transcriptome tiels novel perivascular cell markers. *Stemm Cell Dev.*, 1214-1223.

Huang, Z. W. (2010). The human oocyte and cumulus cells relationship: new insights from the cumulus cell transcriptome. *Mol. Human Rep.*, 715-725.

Jaafar, M. M.-M.-H. (2012). Drive-amplitude-modulation atomic force microscopy: From vacuum to liquids. *Beilstein Journal of Nanotechnology*, 336-344.

Jansen K. A., D. D. (2015). A guide to mechanobiology: Where biology and physics meet.

*Biochimica and Biophysical Acta.*

Jansen, K. A. (2017). Mechanotransduction at the cell-matrix interface. *Semin. Cell Dev. Biol.*, 75-83.

Jelinkova, L. P. (2003). Improved implantation rate after chemical removal of the zona pellucida.

*Fertility and sterility.*

Ji, Y.-I. L.-Y.-J.-O.-O. (2013). Expression Patterns of Thymosin beta 4 and Cancer Stem Cell Marker CD133 in Ovarian Cancers. *Pathol. Oncol. Res.*, 237-245.

Kálmán, M. S. (2001). Immunohistochemical investigation of actin-anchoring proteins vinculin, talin and paxillin in rat brain following lesion: A moderate reaction, confined to the astroglia of brain tracts. *Exp. Brain. Res.*, 426-434.

Karcher, H. L.-M. (2003). A three dimensional viscoelastic model for cell deformation with experimental verification. *Biophys. J.*

Kasas, S. S. (2018). AFM contribution to unveil pro- and eukaryotic cell mechanical PROPERTIES. *Seminars in Cell and Developmental Biology*, 177-187.

Katira, P. Z. (2012). How changes in cell mechanical properties induce cancerous behavior. *Physical reviews letters.*

Kemper, K. d. (2014). Phenotype switching: Tumor cell plasticity as a resistance mechanism and target for therapy. *Cancer Res.*, 5937-5941.

Khalilian, M. N. (2011). Alterations in the mechanical properties of human ovum zona pellucida following fertilization: experimental and analytical studies. *Experimental mechanics*, 175-182.

Khalilian, M. V.-Y. (2013). Estimating zona pellucida hardness under microinjection to assess oocyte/embryo quality: Analytical and experimental studies. *Advances in Bioscience and Biotechnology*, 679-688.

- Kikuchi, K. N. (2000). Maturation/M-phase promoting factor: a regulator of aging in porcine oocytes. *Biol. Reprod.*, 715-722.
- Kim, D. H. (2012). Actin cap associated focal adhesions and their distinct role in cellular mechanosensing. *Sci. Rep.*
- Kondo, T. (2012). Stem Cells and Cancer Stem Cells: New Insights. *Advances in Cancer Stem Cell Biology*, 17-31.
- Krichavsky, M. Z. (2011). Prevention and recovery of hibernating myocardium by microvascular repair. *Circulation*, 998-1000.
- Krieg, M. F. (2019). Atomic-force microscopy-based mechanobiology. *Nature Reviews Physics*, 41-57.
- Krieg, M. H. (2008). A Bond for a Lifetime: Employing Membrane Nanotubes from Living Cells to Determine Receptor–Ligand Kinetics. *Angewandte Chemie*, 9775-9778.
- Kuczynski, W. D. (2002). Rescue ICSI of unfertilized oocytes after IVF. *Human reproduction*, 2423-2427.
- Lathia, J. L. (2017). Overview of Cancer Stem Cells and Stemness for Community Oncologists. *Target. Oncol.*, 387-399.
- Lekka, M. (2017). *Cellular Analysis by Atomic Force Microscopy*. Jenny Stanford Publishing.
- Li, L. W. (2013). MEK1 promotes YAP and therir interaction is critical for tumorigenesis in liver cancer. *FEBS Lett.*, 3921-3927.
- Lim, C. T. (2006). Mechanical models for living cells—a review. *Journal of Biomechanics*, 195-216.
- Lim, E. A. (2004). A phenotypic study of murine oocyte Death in vivo. *Journal of Reproduction and Development*.
- Lin, H. L.-K.-H.-W.-Y.-T.-K.-R. (2015). Mechanical phenotype of cancer cells: cell softening and loss of stiffness sensing. *Oncotarget*.

Liu, C. P. (2015). Mechanical Relaxation of Metallic Glasses: An Overview of Experimental data and Theoretical Models. *Metals*, 1073-1111.

Liu, Y. C. (2019). Robotic Micropipette Aspiration for Multiple Cells. *Micromachines*.

Lord, T. A. (2013). Oxidative stress and ageing of the post-ovulatory oocyte. *Reproduction*, 217-227.

Luis Alfonso, J. G. (2016). Cellular mechanotransduction. *AIMS Biophys.*, 50-62.

Makowiecka, A. M. (2019). Thymosin beta 4 Regulates Focal Adhesions Formation in Human Melanoma Cells and Affects Their Migration and Invasion. *Front. Cell Dev. Biol.*

Makowiecka, A. M. (2021). Changes in Biomechanical Properties of A375 Cells Due to the Silencing of TMSB4X Expression Are Not Directly Correlated with Alterations in Their Stemness Features. *Cells*.

Malinda, K. G. (1997). Thymosin beta 4 stimulates directional migration of human umbilical vein endothelial cells. *FASEB J.*, 474-481.

Martinac, B. (2014). The ion channels to cytoskeleton connection as a potential mechanism of mechanosensitivity. *Biochim. Biophys. Acta*, 682-691.

Martino, F. P. (2018). Cellular Mechanotransduction: from tension to Function. *Frontiers in Physiology*.

Martino, S. D. (2012). Stem cell-biomaterial interactions for regenerative medicine. *Biotechnol. Adv.*, 338-351.

Meaney, D. S. (2015). Cellular biomechanics of central nervous system injury. *Handb. Clin. Neurol.*, 105-114.

Medalsy, I. D. (2013). Nanomechanical Properties of Proteins and Membranes depend on Loading Rate and Electrostatic Interactions. *ACS Nano*, 2642-2650.

Mehta, B. N. (2013). Follicular fluid insulin like growth factor-1 (FF IGF-1) is a biochemical marker of embryo quality and implantation rates in in vitro fertilization cycles. *Journal of Human reproductive sciences*, 140-146.

Miao, Y. K. (2009). Oocyte aging: cellular and molecular changes, developmental potential and reversal possibility. *Human Reproduction Update*, vol.1, 1-13.

Mitchell, G. H. (2010). Arterial stiffness and cardiovascular events: the framingham heart study. *Circulation*, 505-511.

Mollinari, C. R.-V. (2009). Downregulation of thymosin beta 4 in neural progenitor grafts promotes spinal cord regeneration. *J. Cell Sci.* , 4195-4207.

Monnè, M. J. (2011). A structural view of egg coat architecture and function in fertilization. *Biology of Reproduction*, 661-669.

Moreno-Flores, S. B.-H. (2010). Stress relaxation and creep on living cells with the atomic force microscope: a means to calculate elastic moduli and viscosities pf cell components. *Nanotechnology*.

Moreno-Vincente, R. P.-P.-M.-S.-A.-A. (2019). Caveolin-1 modulates Mechanotransduction responses to substrate stiffness through actin-dependent control of YAP. *Cell Rep.* , 1679-1680.

Nagy, A. G. (2006). Removal of Zona Pellucida. *Cold Spring Harb Protoc.*

Nakagata, N. T. (2013). Applications of cryopreserved unfertilized mouse oocytes for in vitro fertilization. *Cryobiology*, 188-192.

Nakao, K. N. (1997). SImple and efficient vitrification procedure for cryopreservation of mouse embryos. *Experimental animals*.

Närwä, E. S. (2017). A Strong Contractile Actin Fence and Large Adhesions Direct Human Pluripotent Colony Morphology and Adhesion. *Stem. Cell Rep.*, 67-76.

Nees, S. W. (2013). Focus on cardiac pericytes. *Arch. Eur. J. Physiol.*, 779-787.

Nie, H.-Y. T. (2011). Subcellular features revealed on unfixed rat brain sections by phase imaging. *Analyst*.

Nowell, C. O. (2016). Chronic inflammation imposes aberrant cell fate in regenerating epithelia through mechanotransduction. *Nat. Cell. Biology*, 168-180.

- O'Callaghan, R. J. (2011). Stiffness and heterogeneity of the pulmonary endothelial glycocalyx measured by atomic force microscopy. *Am. J. Physiol. Lung Cell Mol. Physiol.*, 353-360.
- O'Farrell, F. A. (2014). A role for pericytes in coronary no-reflow. *Nat. Rev. Cardiol.*, 427-432.
- Papi, M. B. (2010). Mechanical properties of zona pellucida hardening. *European Biophysical Journal*, 987-992.
- Park, D. X.-G.-M.-F.-H.-S. (2010). Nestin is Required for the Proper Self-Renewal of Neural Stem Cells. *Stem Cells*, 2162-2171.
- Paszek, M. J. (2005). Tensional homeostasis and the malignant phenotype. *Cancer Cell*, 241-254.
- Pellegrin, S. M. (2007). Actin stress fibres. *Journal of Cell Science*.
- Pesce, M. M. (2017). Cardiac mechanoperception a life-long story from early beats to aging and failure. *Cell Stem Dev.*, 77-90.
- Piccolo, S. D. (2014). The biology of YAP/TAZ hippo signaling and beyond. *Physiol. Rev.*, 1287-1312.
- Piccolo, S. D. (2014). The biology of YAP/TAZ: Hippo signlning and beyond. *Physiol. Rev.*, 1287-1312.
- Pickup, M. W. (2014). The extracellular matrix modulates the hallmarks of cancer. *EMBO Reports*.
- Polacheck, W. J. (2016). Measuring cell-generated forces: a guide to the available tools. *Nat. Methods*, 415-423.
- Puecha, P.-H. P. (2006). A new technical approach to quantify cell–cell adhesion forces by AFM. *Ultramicroscopy*, 637-644.
- Qin, S. L. (2017). NANOG regulates epithelial–mesenchymal transition and chemoresistance in ovarian cancer. *Biosci. Rep.*
- Que, E. L. (2017). Zinc sparks induce physiochemical changes in the egg zona pellicida that prevent polyspermy. *Interg. Biol. (Camb.)*.
- Quinn, P. K. (1985). Improved pregnancy rate in human in vitro fertilization with the use of a medium based on the composition of human tubal fluid. *Fertil. Steril.*, 493-498.

- Raser, J. O. (2005). Noise in Gene Expression. *Science*, 2010-2014.
- Ricci-Vitiani, L. M. (2010). Thymosin beta4 targeting impairs tumorigenic activity of colon cancer stem cells. *FASEB J.*, 4291-4310.
- Rigato, A. M. (2017). High-frequency microrheology reveals cytoskeleton dynamics in living cells. *Nature Physics*.
- Rigato, A. M. (2017). High-frequency microrheology reveals cytoskeleton dynamics in living cells. *Nature Physics*, 771-775.
- Ryan, M. J. (2018). Identifying and managing hibernating myocardium: What is new and what remains unknown? *Curr Heart Fail Rep.*, 214-223.
- Sanders, M. G. (1992). Thymosin beta 4 (Fx peptide) is a potent regulator of actin polymerization in living cells. *Proc. Natl. Acad. Sci. USA*, 4676-4682.
- Sauerbrun-Cutler, M. T. (2015). Oocyte zona pellucida dysmorphism is associated with diminished in-vitro fertilization success. *J. Ovarian research*.
- Scatena, R. (2012). Cancer Stem Cells: A Revisitation of the “Anaplasia” Concept. *Advances in Cancer Stem Cell Biology*, 1-16.
- Scatena, R. (2012). Cancer Stem Cells: A Revisitation of the “Anaplasia” Concept. *Advances in Cancer Stem Cell Biology*, 1-16.
- Scott, W. W. (2002). Use of phase imaging in atomic force microscopy for measurement of viscoelastic contrast in polymer nanocomposites and molecularly thicklubricant films. *Ultramicroscopy*, 151-169.
- Seetharaman, S. E.-M. (2020). Cytoskeletal Crosstalk in Cell Migration. *Trends Cell Biol.*, 720-735.
- Shen, T. B. (2019). Separating the contributions of zona pellucida and cytoplasm in the viscoelastic response of human oocytes. *Acta Biomaterialia*, 253-262.
- Smart, N. R. (2007). Thymosin induces adult epicardial progenitor mobilization and neovascularization. *Nature*, 177-182.

- Snijder, J. I. (2012). Probing the impact of loading rate on the mechanical properties of viral nanoparticles. *Micron*, 1343-1350.
- Snyder, D. W. (2020). A rare subpopulation of melanoma cells with low expression of metastasis suppressor NME1 is highly methastatic in vivo. *Sci. Rep.*
- Sosne, G. S. (2002). Thymosin beta 4 promotes corneal wound healing and decreases inflammation in vivo following alkali injury. *Exp. Eye Res.*, 293-299.
- Stewart, M. P. (2011). Hydrostatic pressure and the actomyosin cortex drive mitotic cell rounding. *Nature*.
- Strippoli, R. L. (2015). Caveolin-1 deficiency induces a MERK-ERK1/2-Snail-1 dependent epithelial-mesenchymal transition and fibrosis during peritoneal dialysis. *EMBO molecular medicine*.
- Su, H. Z. (2020). Sirtuin 3 is essential for hypertension-induced cardiac fibrosis via mediating pericyte transitio. *J. Cell Mol. Med.*, 8057-8068.
- Sullan, R. M. (2014). Single-cell force spectroscopy of pili-mediated adhesion. *Nanoscale*.
- Sun, Q. W. (2007). Evaluation of oocyte quality: morphological, cellular and molecular predictors. *Reproduction, Fertility and Development*, 1-12.
- Sun, Y. C. (2012). Forcing stem cells to behave: a biophysical perspective of the cellular microenvironment. *Annual reviews of biophysics*, 519-542.
- Suresh, S. (2007). Biomechanics and biophysics of cancer cells. *Acta Biomaterialia*, 413-438.
- Susic, D. (2007). Cross-link breakers as a new therapeutic approach to cardiovascular disease. *Biochem. Soc. Trans.*, 853-856.
- Takeo, T. H. (2008). Methyl-beta-cyclodextrin improves fertilizing ability of C57BL/6 mouse sperm after freezing and thawing by facilitating cholesterol efflux from the cells. *Biol. Reprod.*, 546-551.
- Takeo, T. N. (2011). Reduced glutathione enhances fertility of frozen/thawed C57BL/6 mouse sperm after exposure to methyl-Beta cyclodextrin. *Biol. Reprod.*, 1066-1072.

Taqueti, V. R. (2018). Coronary microvascular disease pathogenic mechanisms and therapeutic options. *JACC State of the art Review, J. A. Coll. Cardiol.*

Tari', J. J.-A.-H. (2002). Postovulatory aging of oocytes decreases reproductive fitness and longevity of offspring. *Biology of reproduction*, 495-499.

Tomari, H. H. (2018). Meiotic spindle size is a strong indicator of human oocyte quality. *Reproductive Medicine and Biology*.

Toyoda, Y. C. (2017). Genome-scale single-cell mechanical phenotyping reveals disease-related genes involved in mitotic rounding. *Nature communications*.

Tripathi, S. C. (2020). A mechanism for epithelial-mesenchymal heterogeneity in a population of cancer cells. *PLoS Comput. Biol.*, 1-27.

Velazquez-Villarreal, E. M. (2020). Single-cell sequencing of genomic DNA resolves sub-clonal heterogeneity in a melanoma cell line. *Commun. Biol.*, 1-8.

Vining, K. M. (2017). Mechanical forces direct stem cell behaviour in development and regeneration. *Nat. Rev. Mol. Cell Biol.*, 728-742.

Wang, H. W. (2021). Influence of Fimbriae on Bacterial Adhesion and Viscoelasticity and Correlations of the Two Properties with Biofilm Formation. *Langmuir*.

Watson, C. J. (2006). Post-lactational mammary gland regression: molecular basis and implications for breast cancer. *Exp. Reviews*.

Webster, K. B. (2014). Tensional homeostasis in single fibroblast. *Biophysical Journal*, 146-155.

Wu, P. A. (2018). A comparison of methods to assess cell mechanical properties. *Nature methods*, 491-498.

Xie, K. Y. (2018). Controlling Cellular Volume via Mechanical and Physical Properties of Substrate. *Biophysical J.*, 675-687.

Xu, W. M. (2012). Cell Stiffness Is a Biomarker of the Metastatic Potential of Ovarian Cancer Cells. *PLoS ONE*.

Yamagishi, A. S. (2019). The Structural Function of Nestin in Cell Body Softening is Correlated with Cancer Cell Metastasis. *Int. J. Biol. Sci.*

Yang, M. T.-K. (2011). Assaying stem cell mechanobiology on microfabricated elastomeric substrates with geometries modulated rigidity. *Nat. Protoc.*, 187-213.

Yun, X. T. (2017). Interrogation of drug effects on HeLa cells by exploiting new AFM mechanical biomarkers. *RSC Advances*, 43764-43771.